# High Spin Structure in Nuclei Near $^{208}$Pb Studied by $\gamma$-Spectroscopy

Maurycy Rejmund

Institute of Experimental Physics
Warsaw University
June 1, 1998

Ph.D. Thesis supervised by
dr hab. Teresa Rząca-Urban
Institute of Experimental Physics
Warsaw University

# Contents

# Chapter 1

# Introduction

The basic assumption of the nuclear shell model is that to a first approximation each nucleon moves independently in a potential that represents the average interaction with the other nucleons in the nucleus. This independent motion of the nucleons follows from the combination of the weakness of the nuclear long-range attraction and the Pauli exclusion principle. In analogy to the atomic shell model there are nucleonic orbits in the nucleus that are characterized by various quantum numbers. The nucleonic states of given radial quantum number $n$, orbital angular momentum $l$ and total spin $j$ ($j$ is from coupling $\mathbf{j} = \mathbf{l} + \mathbf{s}$, with $s$ denoting intrinsic spin) still differ in projection $m$ of the total spin $\mathbf{j}$ onto the quantization axis ($m = -j, -j+1, \ldots, j-1, j$), but the $m$-states are degenerate for the spherically symmetric potential. These states form a sub-shell that can be occupied by $2j+1$ protons and $2j+1$ neutrons. The group of orbits (sub-shells) lying close in energy is referred to as a major shell. The nuclei with closed major shells play a particular role. The energy gap between major shells is large compared to the energy spacing between the sub-shells within the major shell, thus the doubly closed-shell nuclei exhibit an extra stability. The way to excite them is by promoting at least one nucleon to the next major shell. This agrees with the observation of relatively high excitation energies of the first excited state in such nuclei as compared to nuclei with partly filled shells. From the systematics of the excitation energy of the first excited state in even-N and even-Z nuclei (N and Z are numbers of neutrons and protons, respectively) one finds it anomalously high when Z or N equals 2, 8, 20, 28, 50, 82 or 126. These are called "magic" nucleon numbers and occur at the shell closure. The magic numbers, as they are observed in nature, could be only reproduced after introduction of a strong spin-orbit coupling term into the independent-particle Hamiltonian.

The nucleus is a many nucleon system and in fact there is no heavy centre of

the force similar to that of the atom. The actual Hamiltonian of the many nucleon system consists of the kinetic-energy term $T(k)$ and the two-particle interaction $W(k,l)$ and after introduction of some average single-particle potential $U(r)$ it is written as

$$H = \sum_{k=1}^{A} [T(k) + U(k)] + \left[ \sum_{1=k<l}^{A} W(k,l) - \sum_{k=1}^{A} U(k) \right] = H^{(0)} + H^{(1)}. \qquad (1.1)$$

Here $H^{(0)}$ defines the independent-particle motion and $H^{(1)}$ represents a residual interaction reflecting the fact that the particles do not move completely independently. With the proper choice of the single-particle potential $U(r)$, the residual interaction $H^{(1)}$ is small and can be treated as a perturbation. Thus, the smaller $H^{(1)}$, the better the true multi-nucleon wave function is represented by the independent-particle wave function $\Phi_l^{(0)}$. For the energy of the state, in first-order perturbation theory, we write

$$E_l = e_l^{(0)} + e_l^{(1)} = \left\langle \Phi_l^{(0)} \left| H^{(0)} + H^{(1)} \right| \Phi_l^{(0)} \right\rangle = \sum_{k=1}^{n} \epsilon_k + \left\langle \Phi_l^{(0)} \left| H^{(1)} \right| \Phi_l^{(0)} \right\rangle \qquad (1.2)$$

where the first term gives the contribution from the single-particle energies and the second term that from the residual interaction. Equation 1.2 shows that for the calculations of the first-order energy shift $E^{(1)}$ one needs only the zeroth-order wave function obtained from the unperturbed Hamiltonian $H^{(0)}$ and the energy shift due to the residual interaction $H^{(1)}$ is then the expectation value of the residual interaction in the unperturbed state.

Generally the particles can scatter between various states $\Phi_i^{(0)}$ and the wave function of the $m$-th state can be written as

$$\Psi_m = \sum_{l=1}^{p} a_{lm} \Phi_l^{(0)} \qquad (1.3)$$

and the corresponding Hamilton operator as

$$H_{kl} = \left\langle \Phi_k^{(0)} | H^{(0)} | \Phi_l^{(0)} \right\rangle + \left\langle \Phi_k^{(0)} | H^{(1)} | \Phi_l^{(0)} \right\rangle = e_l^{(0)} \delta_{kl} + H_{kl}^{(1)} \qquad (1.4)$$

The eigenvalues and the eigenvectors of the above operator represent excitation energies $E_m$ and amplitudes of wave functions $\vec{a}_m$ of the $m$-th state, respectively.

The shell-model theory has been very successful in describing the properties of nuclei that are located in the vicinity of the double (proton and neutron) shell closures. The doubly magic nucleus plays the role of the spherical, inert, hard core of total spin $I = 0$ and produces the average nuclear potential. The valence particles

or holes, that are added to a magic core, are assumed to move independently on the corresponding single-particle orbits. The energies and the wave functions, describing the discrete states of the nucleus, can then be calculated (Equation 1.4), once the single-particle energies $\epsilon_k$ and the matrix elements of the residual interaction $H^{(1)}_{kl}$ are known. For practical shell-model calculations one often takes the empirical single-particle energies which can be extracted from the energy spectrum of the one particle and one hole neighbours of the core nucleus (Figure 1.2). In this way the involved calculation of the independent-motion Hamiltonian and the solution of the corresponding Schrödinger equation can be avoided. The residual interaction for many particle states can be calculated from the two body interaction between the participating nucleons. This is the main task of the shell model theory and computer programs and is treated in various text books [Bru77, Law80, Hey90]. A much simplified example of such calculations is presented in Section 3.2.

The knowledge of the two body residual interaction is therefore central to the understanding of nuclear structure. Some of the matrix elements can be measured directly in nuclei with two or slightly more particles outside of the closed core. This is one of the goals of the presented experiments. Ideally theory should be able to predict this two body shell-model interaction inside the nucleus from the known interaction between free nucleons. Kuo and Brown have worked out a method to accomplish this [Kuo66]. Properties of nuclei close to $^{208}$Pb are calculated with an interaction derived in this way and compared with experimental findings in Chapter 4.

Spectroscopic studies in the mass regions of doubly magic nuclei like $^{16}$O, $^{40}$Ca, $^{56}$Ni or $^{208}$Pb have been usually the main interest of shell-model research. It became apparent that the study of the effective interaction is most advantageous in the neighbourhood of doubly magic $^{208}$Pb. It is now commonly accepted that the $^{16}$O, $^{40}$Ca and $^{56}$Ni systems form doubly closed cores only in a limited sense. There are low lying deformed states in these nuclei that complicate the picture. Thus, the spherical shell-model has only limited applicability. The variety of stripping and pick-up experiments, performed on the $^{208}$Pb core, suggest that it is a good closed shell nucleus and thus one expects the shell model to be especially successful in the Pb region. It has been also verified that the $^{208}$Pb core is highly stable against deformations and the spherical shape remains even if up to ten nucleons are removed or added to the core. The shell model description of the $^{208}$Pb region encounters however also one problem. The first excited state of $^{208}$Pb is an octupole vibration that poses some difficulties for the shell model. But the main features of this level can be reproduced by a shell model wave function with many components as shown

in Chapter 4.

The interaction between the octupole vibration and the single particle motion is a separate subject of general interest since a long time [Ham74, Bohr75]. New data on this subject are presented in Section 3.5 and are used to check the theory of particle octupole-vibration coupling.

$^{208}$Pb and some of its neighbours are stable and allow therefore a variety of experimental studies. The part of the chart of nuclides around the doubly magic $^{208}$Pb is shown in Figure 1.1. The nuclei with one and two valence particles or holes outside of $^{208}$Pb core are presented. They are particularly important to study the basic parameters of the nuclear shell model in this mass region. The stable nuclei, i.e. $^{206,207,208}$Pb and $^{209}$Bi, are indicated by the black squares. The masses of $^{208}$Pb and its one- and two-particle neighbours have been established with high accuracy. Also the single particle states (proton in $^{209}$Bi and neutron in $^{209}$Pb) and single hole states (proton-hole in $^{207}$Tl and neutron-hole in $^{207}$Pb) outside the doubly magic core, are very well studied and the corresponding single particle(hole) energies are now all known from experiment. They are schematically shown in Figure 1.2, where the binding energies are given in keV relative to $^{208}$Pb. The energy of the shell gap, above the shell closure, is not up to scale in the figure and its actual energy is large, about 3.4 MeV for neutrons and 4.2 MeV for protons, and comparable to the energy width of a single major shell. It is apparent, that due to the large energy needed to excite the magic core, the properties of nuclear states at moderate excitation energy in nuclei in this mass region, are to be derived from only a very few valence nucleon configurations and hence not very difficult to be interpreted in the frame of shell-model theory.

Many important properties of the nuclei around $^{208}$Pb have been measured by charged particle spectroscopy. For instance studies of $^{207}$Pb$(d,p)^{208}$Pb and $^{209}$Bi$(t,\alpha)^{208}$Pb have determined the strengths of neutron and proton particle-hole configurations in many excited states of $^{208}$Pb [Sch97, Val97]. Also the $\gamma$-decay of nearly all states below 5 MeV in $^{208}$Pb has been measured [Sch97, Yeh97]. The single particle M1 and E2 matrix elements are also known [Sch93] and therefore quantitative information on the wave functions could be extracted from the $\gamma$ transitions [Sch93, Sch95]. Very careful and high resolution measurements of inelastic electron and proton scattering have also been performed. Essentially all possible charged particle spectroscopy experiments have been performed, even $^{210m}$Bi$(t,\alpha)^{209}$Pb with a radioactive beam and radioactive target [Han77].

There is on the other hand a lack of evidence for high spin states in these nuclei. The high spin states lying close to the yrast line are often of high configurational

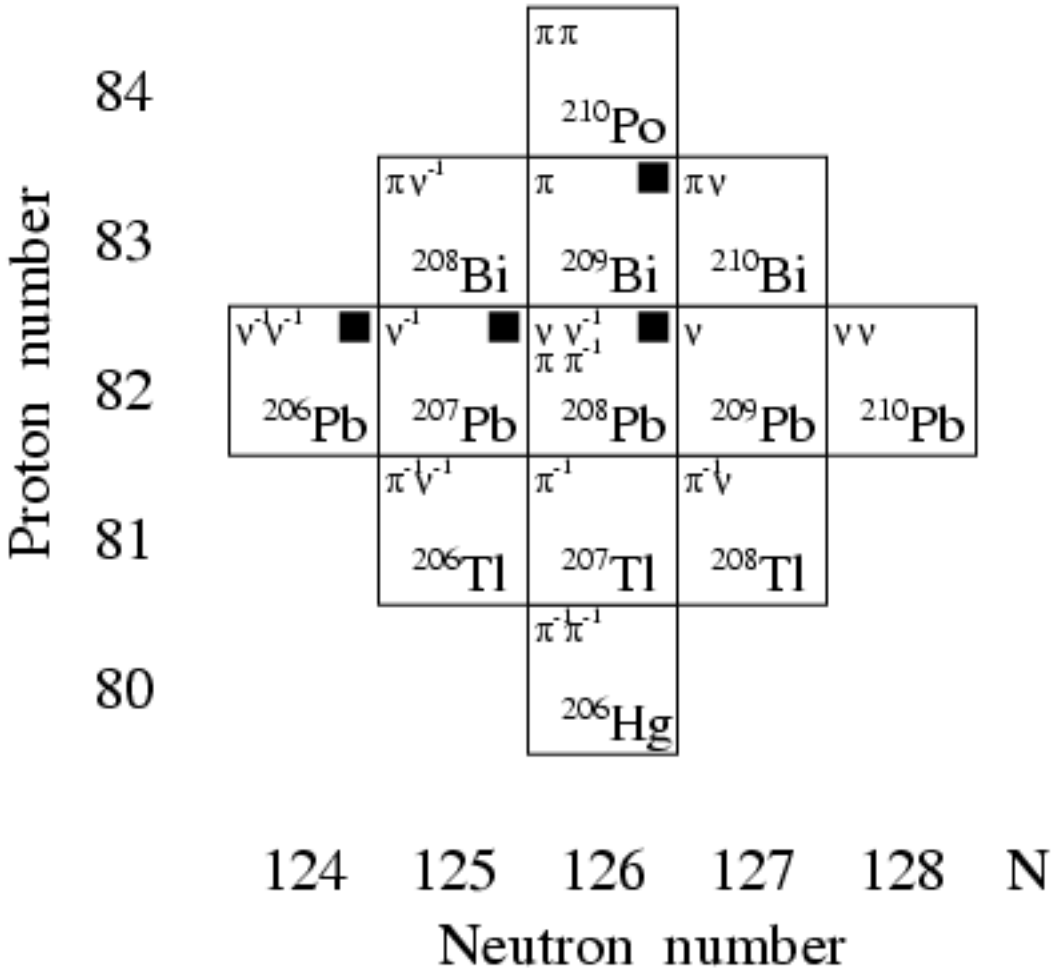


Figure 1.1 The part of the chart of nuclides around $^{208}$Pb. Only the neighbours with one and two particles or holes outside of the doubly magic $^{208}$Pb core are shown. Those are nuclei of major importance for determination and verification of the parameters of the nuclear shell model in this mass region. The symbols $\pi$ and $\nu$ indicate a valence proton and neutron, respectively in the particle or the hole state. The black squares stand for stable nuclei.

purity and therefore of great importance for the study of the residual interaction. But the nuclei near $^{208}$Pb are too neutron rich to be populated in fusion evaporation reactions, which are commonly used for the study of nuclear states at high angular momentum. This disadvantage has been overcome at present. Recent technical developments of large multi-detector $\gamma$-ray arrays opened new possibilities to exploit more complex nuclear processes which populate the nuclei of interest with suitable yields for $\gamma$ spectroscopy. Of these the deep inelastic collisions became relevant.

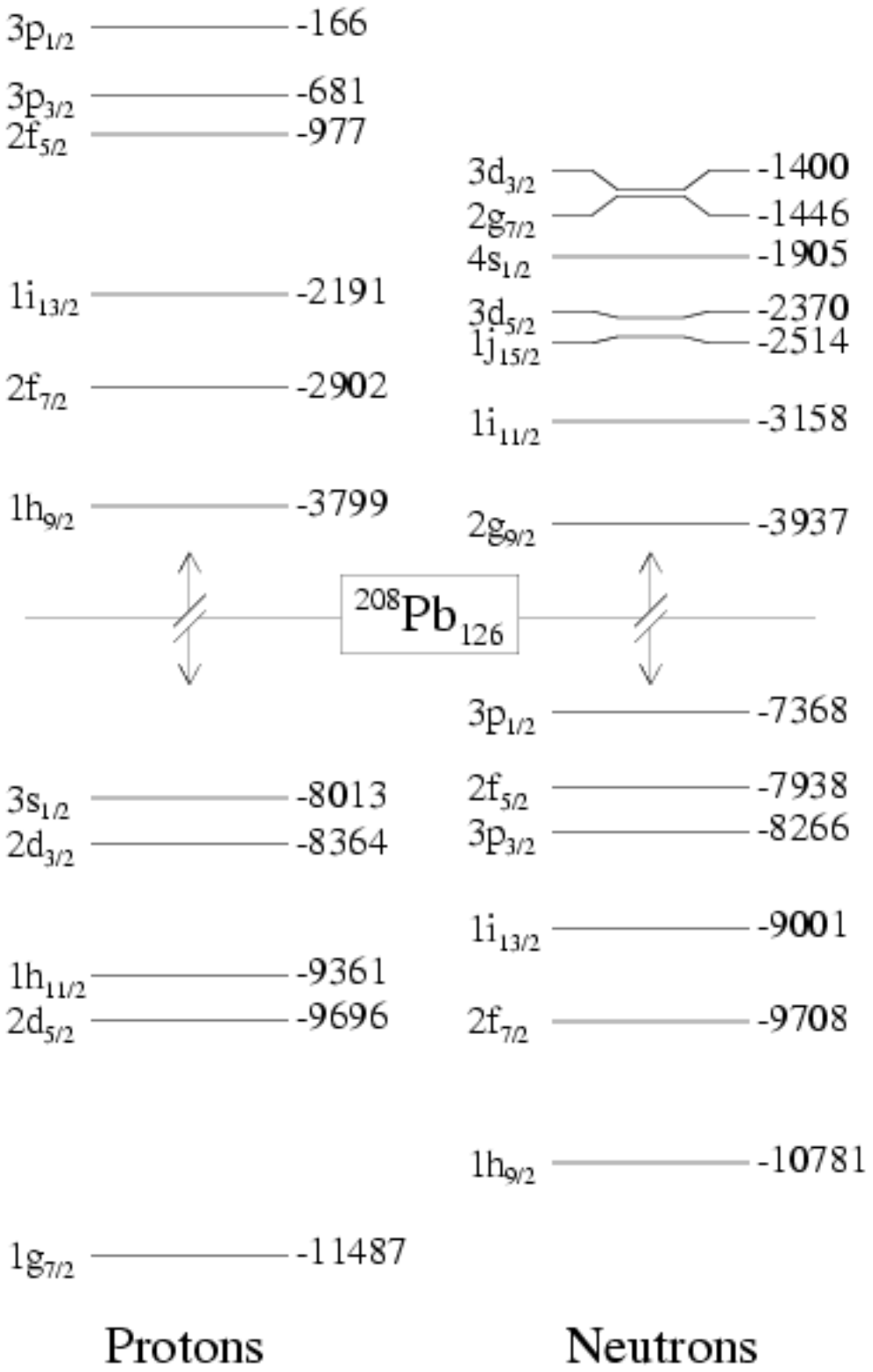


Figure 1.2 The single-particle energies for proton and neutron states in $^{208}$Pb region. They are taken from experimental spectra of $^{207}$Tl, $^{207}$Pb, $^{209}$Bi and $^{209}$Pb. The energies are given in keV relative to $^{208}$Pb.

They indeed populate more neutron rich nuclei, that cannot be reached with fusion evaporation reactions, and this reaction mechanism now can be used as a new tool for high spin $\gamma$-ray spectroscopy.

Deep inelastic collisions of $^{64}$Ni, $^{82}$Se [Sch92, Sch93(a)] and $^{76}$Ge [Bro96] heavy ion beams with thick $^{208}$Pb targets have recently been successfully used to study the $\gamma$-decay of high spin states in nuclei around $^{208}$Pb. They revealed many new states in several nuclei, in particular in $^{207}$Pb and in $^{208}$Pb. The experiments presented here aimed at a further extension of the present knowledge towards higher spins and more neutron rich nuclei. Therefore, we used still heavier and more neutron rich ion beams, i.e. $^{136}$Xe and $^{208}$Pb ions, to bombard thick $^{208}$Pb targets. The $\gamma$-rays deexciting the high spin states in nuclei populated in deep inelastic reactions were measured using an efficient multi-detector $\gamma$-array.

In the following section of this work the details of our experimental setup and that of data taking and analysis are described. The third section presents our experimental findings and their interpretation and discussion. Shell model calculations with a new realistic interaction and for a larger model space than used so far are described in Chapter 4.

# Chapter 2

# Experiments

A number of processes can be distinguished in heavy ion collisions when the projectile energy exceeds the Coulomb barrier by a few percent. In a classical picture they can be classified with respect to the impact parameter $b$ of the colliding ions.

If the impact parameter is significantly greater than the sum of the radii of the colliding nuclei distant collisions occur. They lead mainly to elastic scattering and Coulomb excitation processes. The nuclear interaction between the projectile and target nucleus is negligible compared to the electromagnetic interaction. The trajectories of the colliding ions are fully determined by the Coulomb potential.

With the decrease of the impact parameter towards the grazing impact parameter grazing collisions become more and more probable. They lead generally to inelastic scattering reactions with the transfer of a few nucleons due to a considerable amount of nuclear interaction. The time of the interaction corresponds to the time-of-flight of the projectile trough the interaction region.

For impact parameters smaller than the grazing impact parameter generally two types of collisions can be distinguished. The first class, close collisions, leads to deep inelastic reactions. They are characterized by an intense flow of mass and charge between the interacting ions. The interaction takes a significantly longer time than the time-of-flight trough the interaction region. Much relative kinetic energy is converted into excitation of the nuclei. It is however still possible to distinguish the projectile-like and the target-like nucleus among the reaction products. The second class of collisions, for a still smaller impact parameter $b$, are deeply penetrating collisions. They lead to the formation of a compound system. The interaction time is a few orders of magnitude longer than the penetration time of the target nucleus by the projectile. The compound nucleus, resulting in the collision, can decay by fission or deexcite by evaporating light particles, depending on its mass, charge,

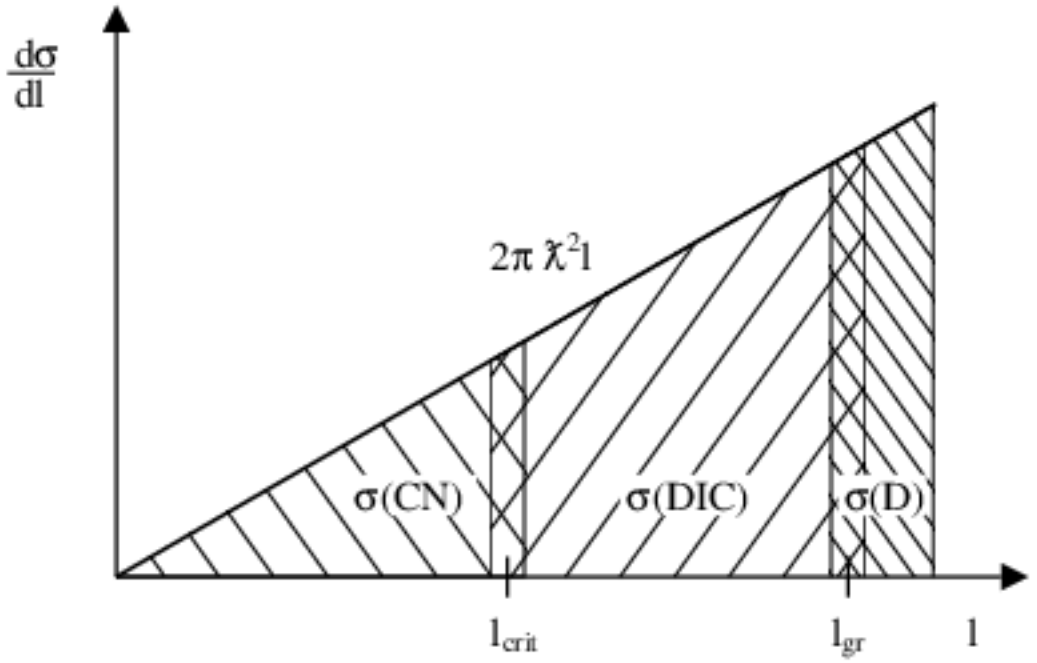


Figure 2.1 Schematic representation of the differential reaction cross section $d\sigma/dl$ in the classical frame. The area below the line corresponds to the cross section for $\sigma$(CN) - compound nucleus formation reactions, $\sigma$(DIC) - deep inelastic reactions, $\sigma$(D) - direct reactions.

angular momentum and energy.

Instead of the classical impact parameter the angular momentum might be used to classify the various processes. A schematic representation of the cross section as function of the angular momentum $l$ is shown in Figure 2.1. Two characteristic values of the angular momentum $l$ are to be considered namely $l_{crit}$ and $l_{gr}$ [Wil80]. The collisions characterized by $l_{crit} \leq l \leq l_{gr}$ are dominantly deep inelastic. In the vicinity of $l_{crit}$ deep inelastic and fusion processes compete. Below $l_{crit}$ fusion dominates. If the angular momentum of the projectile is close to $l_{gr}$ deep inelastic reactions compete with direct reactions. The latter dominate the reaction cross section at $l > l_{gr}$.

At beam energies of a few percent above the Coulomb barrier the deep inelastic reactions prevail and contribute significantly to the total reaction cross section. They result in the transfer of many particles, high angular momentum and large excitation energy of the reaction products. It has been shown that deep inelastic reactions preferentially populate high spin yrast states [Sch93, Sch93(a), Bro94, Bro96]

and can be used to study excitations in stable and moderately neutron rich nuclei that cannot be reached with fusion-evaporation reactions [Paw94, Sch93, Sch93(a)]. Various $\gamma$ spectroscopy investigations of the nuclei produced in deep inelastic reactions have been very fruitful recently [Sch93, Sch93(a), Paw94, Bro96, Rej97, Rej98]. About 200 different nuclei have been produced and identified in one reaction of this type [Kró96]. An important feature of deep inelastic reactions is a strong trend to equilibrate the $N/Z$ ratio of the colliding nuclei. Therefore in order to enhance the production of the neutron rich nuclei of interest, one favoures projectile and target ions, that are as neutron rich as possible. The excited reaction products evaporate however neutrons; this limits the access to the very neutron rich region.

The mentioned $\gamma$-spectroscopy experiments with deep inelastic reactions utilized the thick target technique. This implies very important consequences for the performed measurements. First, the projectiles penetrating the target slow down until they are stopped or undergo a nuclear reaction. Therefore the observed population is only in part due to deep inelastic reactions that dominate at the full beam energy. When the energy of the particles is gradually lowered towards the Coulomb barrier the reaction mechanism changes from mainly deep inelastic to predominantly quasi elastic processes. At energies close and below the Coulomb barrier Coulomb excitation of projectile and target nuclei dominates.

The second effect, when a thick target is used, results from the fact that the recoiling reaction products are stopped in the target. The stopping time is about 3 ps. Most of the $\gamma$-rays are emitted after this time and therefore no Doppler correction is required and a high energy resolution achieved. The $\gamma$-rays emitted before the nuclei are at rest are however highly Doppler broadened and contribute to the unresolved background.

## 2.1 Experimental techniques

Two experiments have been performed to study high spin states of nuclei in the vicinity of $^{208}$Pb. A 30 mg/cm$^2$ thick $^{208}$Pb target, isotopically enriched to 98%, was used in these experiments. It was hit by heavy ion beams of $^{136}$Xe and $^{208}$Pb, provided by the UNILAC accelerator of GSI-Darmstadt. The beam energies in the laboratory system $E_{LAB}$ of 779 MeV for $^{136}$Xe and 1356 MeV for $^{208}$Pb were chosen to give about $(E_{CM} - V_C)/V_C = 0.12$[1] energy excess over the Coulomb barrier, because these experimental conditions were used successfully in similar reactions

[1] $E_{CM}$ and $V_C$ stand for the beam energy and the Coulomb barrier in the Center of Mass system

involving lighter ion beams [Kró96]. The parameters of the reactions used in the present work are given in Table 2.1 as calculated in ref. [Wil80]. The systems are so heavy, that fusion does not occur ($l_{crit} = 0$).

Table 2.1 Parameters of the reactions used in the present study: $E_{LAB}$ - beam energy in the laboratory system, $E_{CM}$ and $V_C$ beam energy and Coulomb barrier in the center of mass system, $l_{crit}$ and $l_{gr}$ - the critical and grazing angular momenta, $\sigma_{react}$ - the total reaction cross section.

| projectile | target | $E_{LAB}$ [MeV] | $V_C$ [MeV] | $(E_{CM} - V_C)/V_C$ | $l_{crit}$ [$\hbar$] | $l_{gr}$ [$\hbar$] | $\sigma_{react}$ [mb] |
|---|---|---|---|---|---|---|---|
| $^{136}$Xe | $^{208}$Pb | 779 | 421 | 0.12 | 0 | 211 | 764 |
| $^{208}$Pb | $^{208}$Pb | 1356 | 605 | 0.12 | 0 | 302 | 853 |

The setup used in these experiments [Schl] consisted of five Compton suppressed EUROBALL HPGe-Cluster detectors [Ebe94] and 132 NaI detectors of the CRYSTAL BALL array [Met83]. The HPGe-Cluster detector consists of seven large hexagonal tapered encapsulated Ge detectors closely packed in a common cryostat. The single HPGe-crystal has a length of 78 mm and diameter of 70 mm at the cylindrical rear end. The HPGe-Cluster detectors were surrounded by a common BGO escape-suppression shield. A schematic picture of the HPGe-Cluster detector is shown in Figure 2.2 on page 12. The cross section of the detector is presented on the left side; the dashed area indicates the BGO escape-suppression shield. The front view of the detector, only the Ge-detectors, is shown on the right. The five HPGe-Cluster detectors were placed in a ring around the beam axis. The distance from the front of the Ge-crystals to the target was 36 cm and the center of the HPGe-Cluster detectors was at 154° relative to the beam axis. The Ge detectors covered about 7% of the full solid angle. A total photo-peak efficiency of 2.2% and energy resolution of 2.6 keV FWHM were achieved at a $\gamma$-ray energy of 1.33 MeV. The CRYSTAL BALL array covered about 83% of the solid angle and had a photo-peak efficiency of about 53% at 1.33 MeV.

A very high yield of Pb X-rays in the experiment with the $^{208}$Pb beam was observed. This made it necessary to use absorbers consisting of 0.5 mm Ta and 0.5 mm Cu in front of the Ge detectors. Consequently the efficiency at $\gamma$-ray energies below 200 keV was significantly reduced in this experiment.

The beam was pulsed with two independent frequencies. The width of the macro pulse was about 5 ms with a repetition time of 20 ms. The intensity distribution

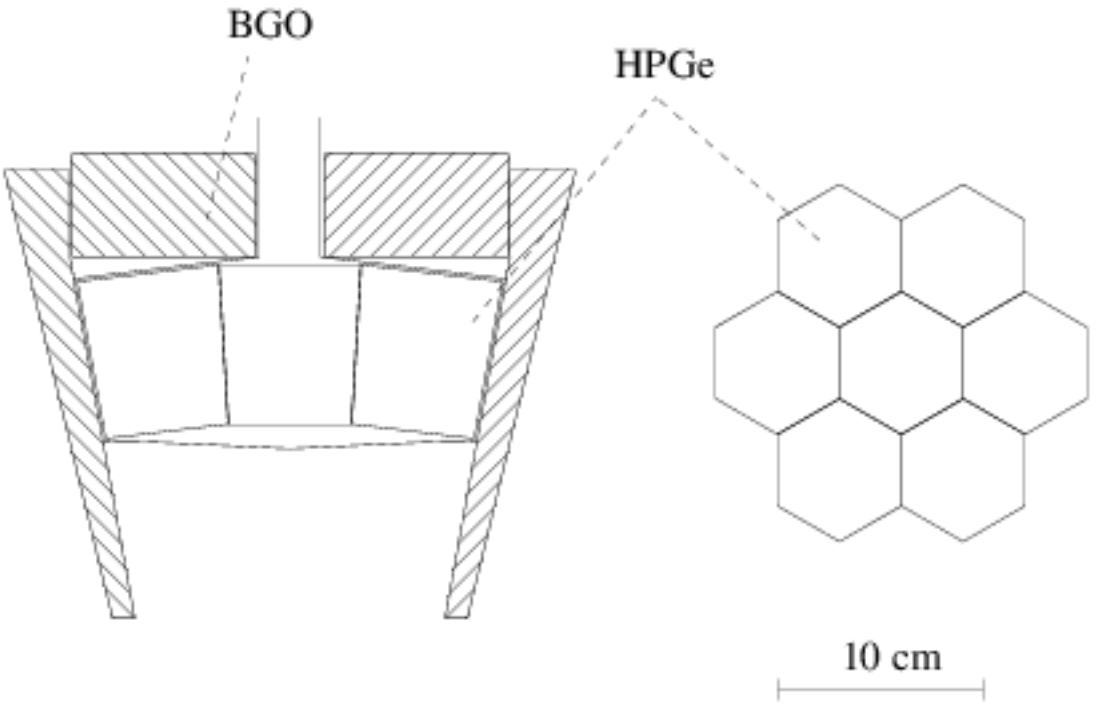


Figure 2.2 Schematic view of the EUROBALL HPGe-Cluster detector.

during the macro pulse varied, an example is shown in Figure 2.5. The micro pulse of the beam was about 1 ns wide and had a repetition time of 111 ns. The charge state of $^{136}$Xe ions was $18^+$ and the average beam current 20 nA. This gives an intensity of about 4.5 pnA in the macro pulse of the beam. The charge state of the $^{208}$Pb ions was $27^+$ and the average beam current 10 nA, or about 1.5 pnA in the macro pulse of the beam.

The electronic logic defined a valid event as a coincidence of at least two Compton-suppressed $\gamma$-signals from the Ge-detectors. An electronic circuit has been used to distinguish the $\gamma$-$\gamma$ coincidences that occurred in adjacent Ge-crystals; these were assumed as resulting from a Compton scattering of a single $\gamma$ ray. Therefore, if two $\gamma$ rays were detected in adjacent Ge-crystals, one more $\gamma$ ray was required to constitute a valid event. The maximum time separation between coincident $\gamma$-rays was set by a hardware condition of a time overlap equal to 130 ns. The schematic diagram of the timing logic as used in the experiments is presented in Figure 2.3 on page 13. Because electronic delays used in the experiments are omitted in the Figure, logic decisions can seemingly go backward in time. For each valid event the preceding beam micro pulse was selected as the $T_0$ time reference for this event, this is indicated by the backward going arrow in Figure 2.3. This $T_0$ pulse opened a 1 $\mu$s

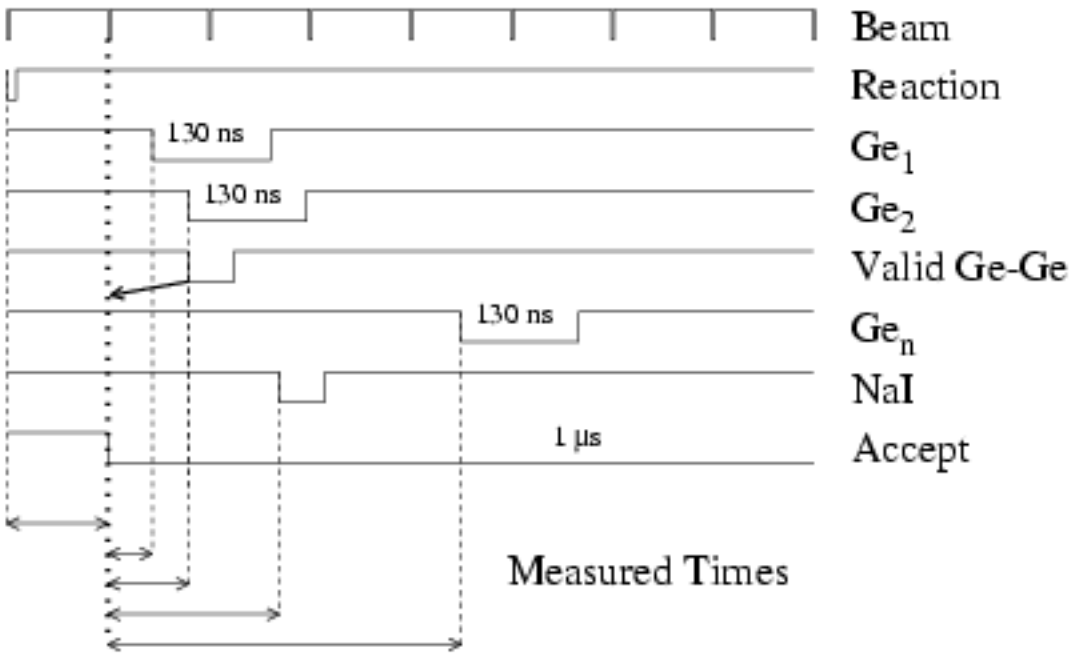


Figure 2.3 Schematic diagram of the timing logic as used in the experiments. The electronic delays used in the experiment are omitted in the picture. See also text for further description.

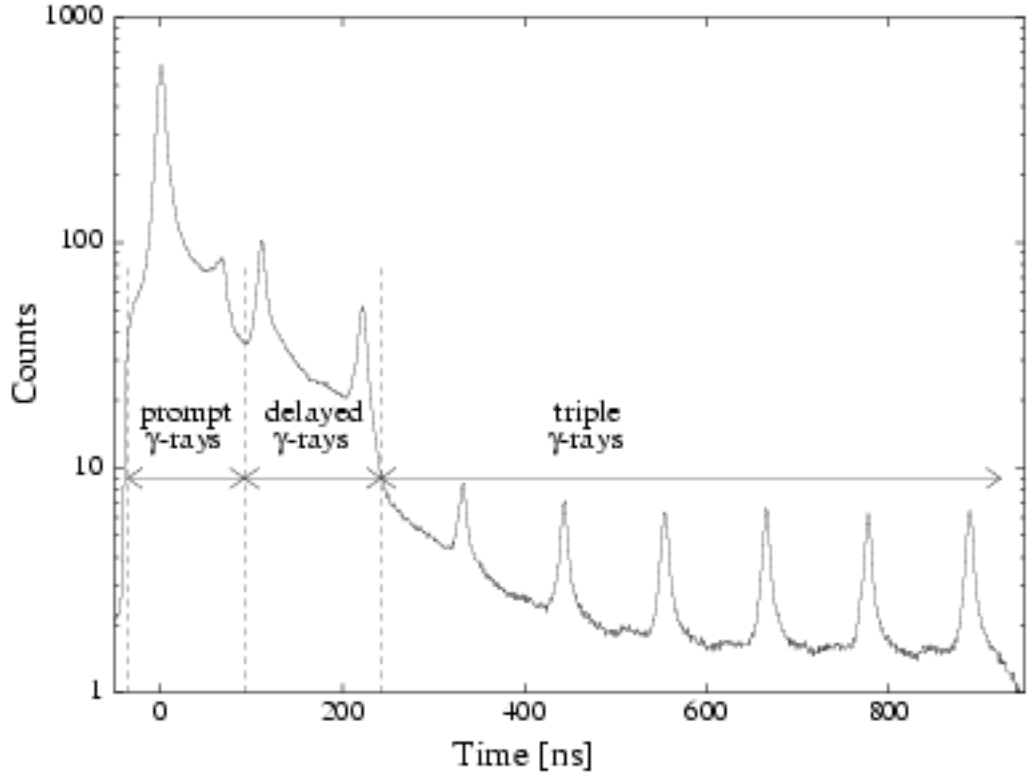


Figure 2.4 The time spectrum of the Ge-detectors from the experiment with the $^{136}$Xe beam. The Y scale is chosen arbitrarily.

wide time gate for the data acquisition system. The energies and times of all Ge- and NaI-detectors that fired within this time window were measured and stored. All times were measured relative to the $T_0$ pulse, as shown in Figure 2.3.

A prompt $\gamma$-multiplicity of ($M_{\gamma\text{ball}} \geq 3$) in the CRYSTAL BALL array was chosen to signal at which micro beam pulse a reaction occurred. The time between this signal (the occurrence of a reaction), labeled Reaction in Figure 2.3 and the $T_0$ signal was also measured, as indicated in the Figure. The time of the reaction could be recorded when the reaction preceded the valid event by $T_R \leq 1$ $\mu$s. This enables to measure $\gamma$-$\gamma$-coincidences in the decay of an isomer at longer times than the 111 ns spacing of the beam pulses. The major part of the events however occured prompt in the vicinity of a given micro pulse of the beam.

The time spectrum of the Ge detectors from the experiment with the $^{136}$Xe beam is presented in Figure 2.4 (page 13); it shows the sum of all Ge-detectors. The first part, marked "prompt $\gamma$-rays", shows the beam interval around the reference peak, that is selected by the first Ge-signal. Therefore at least one of the time signals of the coincidence event, namely that coming first has to be here. In the second region, marked "delayed $\gamma$-rays", the time signals of the second Ge-detector occur that can be delayed by the coincidence time of about 130 ns relative to the first Ge-signal. Finally in the third region, marked "triple $\gamma$-rays", only the third signal from events with a $\gamma$-multiplicity of at least 3 can appear; after a coincidence of two Ge-detectors has established a valid event, a third signal is registered in the acceptance interval. The first big peak in this spectrum shows prompt $\gamma$-rays, all others are due to random coincidences with signals belonging to later beam pulses. The decay of the intensity between the prompt peaks, that is clearly visible between 100 and 400 ns, is due to isomers. The drop of the intensity at the two borders between these 3 intervals is due to this fact, that the times of all detectors can lie in the first interval, then in the second interval only the second time signal can appear, and in the third only that of the third (and still later) detectors.

$\gamma$-$\gamma$ coincidences were measured during the macro pulse (beam on) and out of the macro pulse (beam off). Therefore, an additional parameter was introduced. It measured the time position of the event with respect to the macro pulse, as shown in Figure 2.5. The part up to 5 ms corresponds to the beam pulse where dominantly prompt and short lived radiation was measured. The beam intensity increased within the first millisecond to about 80% of the maximum intensity. During the next two milliseconds the intensity increase was significantly slower, and after 3 ms the plateau of maximum intensity was reached. The spectrum beyond 5 ms corresponds to the off-beam time when only transitions from long lived states, either isomers or

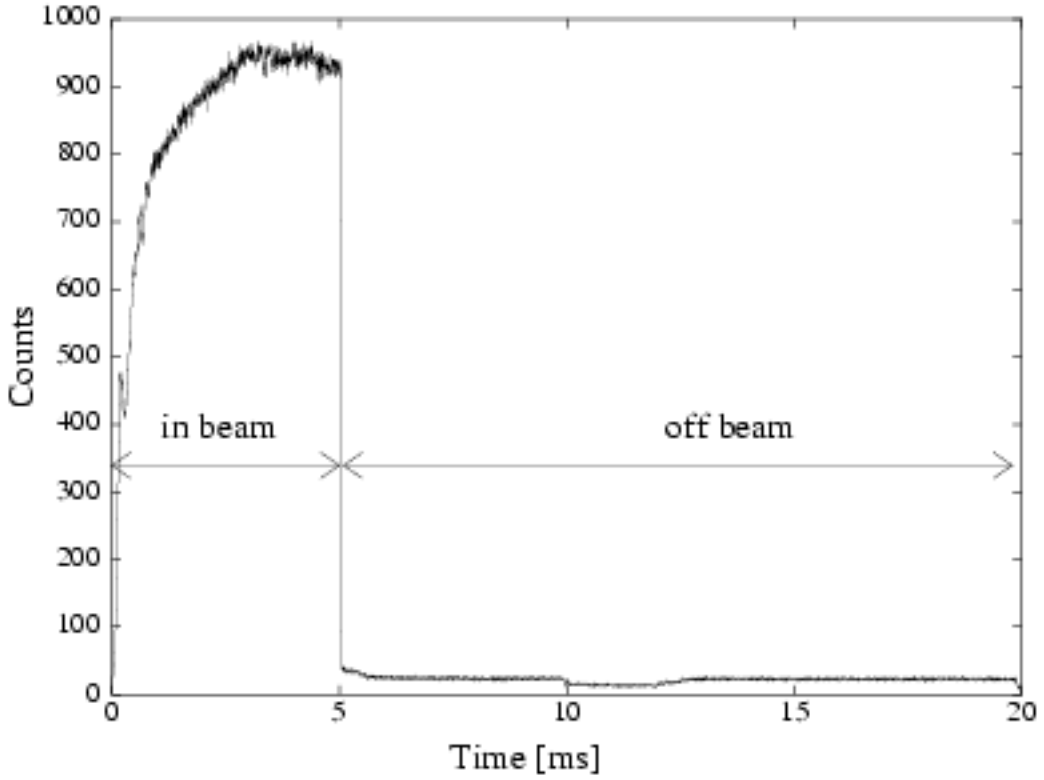


Figure 2.5 Time distribution of the events with respect to the macro pulse of the beam from the experiment with the $^{208}$Pb beam. The Y scale is chosen arbitrarily.

$\beta$-decay, were measured.

The total number of valid events recorded in the experiment using the $^{136}$Xe beam was $112.1 \times 10^6$. The number of events recorded in the macro pulse of the beam was $108.0 \times 10^6$ and outside $4.1 \times 10^6$. In the experiment using the $^{208}$Pb beam the total number of events was $69.6 \times 10^6$ where $68.1 \times 10^6$ were in the macro pulse of the beam and $1.5 \times 10^6$ outside.

The energy and efficiency calibrations were performed using standard radioactive sources of $^{60}$Co, $^{133}$Ba, $^{152}$Eu and $^{226}$Ra. The data obtained from the Ge-cluster detectors were treated in "add-back" mode; the energy signals of two $\gamma$-rays in neighbouring Ge-crystals detected within a 50 ns wide time window were summed up into one energy. The assumption was made, that the two signals resulted from the Compton scattering of a single $\gamma$-ray. The time calibration used the precisely known micro pulse structure of the beam (see Figure 2.4 on page 13). The slow time scale relative to the macro pulse was measured with an absolutely calibrated time digitizer.

## 2.2 Data analysis

The experimental data were analysed event by event off-line and sorted into $E_\gamma$-$E_\gamma$ (energy versus energy of coincident $\gamma$ rays) and $E_\gamma$-$T_\gamma$ (energy versus time of $\gamma$-rays) matrices. Prompt-prompt, prompt-delayed and off-beam $E_\gamma$-$E_\gamma$ coincidence matrices (two dimensional intensity distributions) were constructed. Then one dimensional $\gamma$-$\gamma$ coincidence spectra, both as function of time and of energy, were generated by projecting from the relevant $E_\gamma$-$E_\gamma$ or $E_\gamma$-$T_\gamma$ matrix onto one axis with the gate on the photo-peak of an individual $\gamma$ ray on the other axis. The background in these spectra was determined from projections with additional gates in the vicinity of this given photo-peak and then after proper normalization subtracted. This procedure is based on the assumption that the background has only a weak energy dependence and can be interpolated under the photopeak from points in its vicinity.

The aim of the analysis was to identify new $\gamma$-ray transitions that depopulate high spin states in nuclei in the $^{208}$Pb region. The identification was based on coincidences with already known transitions in the given nucleus. In special cases, when no $\gamma$-rays were known or long lived isomers prevented $\gamma$-ray coincidence measurements, the cross coincidence technique was used [Paw94, Kró96]. It is based on the analysis of coincidences with known $\gamma$ transitions in the partner nucleus of the binary reaction. This often allows to assign new $\gamma$-transitions to a nucleus. But transitions in the partner nucleus may also be misassigned to the studied nucleus itself. This can be excluded if one analyses the coincidence spectra from different measurements using various projectile-target combinations (see Figure 3.4 on page 31). For identified $\gamma$ transitions the relevant time distribution was analysed to check for possible isomerism of the depopulated state.

The prompt-prompt $E_\gamma$-$E_\gamma$ coincidence matrix was sorted event by event using the software condition that the multiplicity of the detected $\gamma$-rays in the Ge detectors $M_{\gamma\mathrm{Ge}} \geq 2$. Events with a $\gamma$-ray multiplicity of 3 or more, $M_{\gamma\mathrm{Ge}} \geq 3$, were unfolded into the corresponding series of $\gamma$-$\gamma$ coincidences. Only events that occured within the macro pulse of the beam, 0 ms $\leq T \leq$ 5 ms, were considered in this matrix (see Figure 2.5 on page 15). Although the width of the beam micro pulse was about 1 ns and the time resolution of the Ge detectors about 10 ns, we required that both coincident $\gamma$-rays occured between 30 ns before and 90 ns after the same beam pulse. Low energy $\gamma$-rays $E_\gamma < 200$ keV often exhibit a long electronic time delay, that could reach about 100 ns. For $\gamma$-ray energies greater than 200 keV this effect was negligible. To avoid an additional decrease of efficiency for the low energy $\gamma$-rays

the software time window was set 120 ns wide. The last condition requested for the prompt-prompt matrix was that a nuclear reaction ($M_{\gamma\text{ball}} \geq 3$) occurred at the same micro pulse of the beam. No further distinctions between $\gamma$-rays were made in this case. The resulting prompt-prompt matrix was symmetrized.

The prompt-prompt $E_\gamma$-$E_\gamma$ coincidence matrix allowed to investigate excited states in nuclei that decayed by emission of $\gamma$-rays shortly after they were created in the nuclear reaction. Due to the relatively wide time coincidence window used also the deexcitation of short lived isomers could be studied including $\gamma$-$\gamma$ coincidences across the isomer. However, the coincidence intensities of delayed $\gamma$-rays with respect to the prompt ones, that precede the isomer, were reduced in accordance with the timing conditions.

An example for a spectrum from the prompt-prompt matrix is presented in Figure 3.4 on page 31. The spectrum shows prompt $\gamma$ rays coincident to the 1422.7 keV transition in $^{209}$Pb (see also Figure 3.5 on page 32) derived from the experiments using $^{208}$Pb beam (upper panel) and $^{136}$Xe (lower panel). $\gamma$ transitions from the partner nuclei of the binary reaction are evident in the spectra besides those assigned to $^{209}$Pb.

The prompt-delayed $E_\gamma$-$E_\gamma$ coincidence matrix was created using the software condition on the multiplicity of the detected $\gamma$-rays in the Ge detectors $M_{\gamma\text{Ge}} \geq 3$. It was required that at least two prompt-coincident transitions occured within the time window $-30$ ns $\leq T_{\text{prompt}} \leq 90$ ns and at least one delayed $\gamma$ ray after $T_{\text{delayed}} \geq 130$ ns with respect to the same micro pulse of the beam (see Figure 2.4 on page 13). Because the hardware trigger during the measurement required already a $\gamma$-$\gamma$ coincidence within 130 ns, only triple coincidences can include one detector that fires later. The minimal delay of 130 ns was also chosen to exclude random coincidences with prompt radiation from the next beam pulse and electronically delayed low energy $\gamma$ rays. All events were unfolded into simple prompt-delayed coincidences. The resulting matrix was asymmetric with prompt and delayed $\gamma$ rays on the two axes. The additional requirements, specifying the time relation of the event relative to the reaction and the macro pulse of the beam, were taken as for the prompt-prompt matrix. The prompt-delayed $E_\gamma$-$E_\gamma$ matrix provided a very efficient mean to study and identify the prompt radiation preceding an isomer in coincidence with the delayed $\gamma$-rays that depopulate the isomeric state.

A typical projection of the prompt delayed matrix is presented in Figure 3.1 on page 23. This spectrum shows the prompt $\gamma$-rays coincident with the delayed 799.7 keV transition in $^{210}$Pb (see also Figure 3.2 on page 25) from the experiment with the $^{208}$Pb beam. The prompt $\gamma$ transitions identified with $^{210}$Pb are evident.

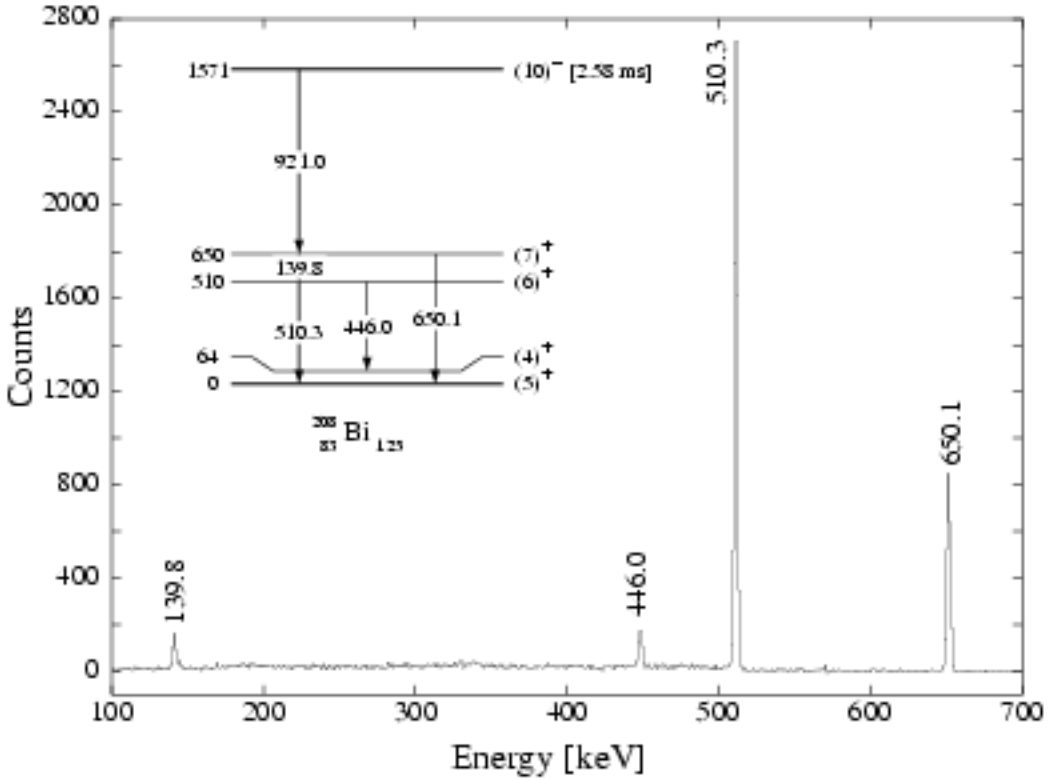


Figure 2.6 The off-beam spectrum of $\gamma$-rays coincident with the 921.0 keV transition. The relevant level scheme of $^{208}$Bi is shown in the inset. The spectrum is from the experiment with the $^{208}$Pb beam.

The 803 keV transition belongs to $^{206}$Pb, the binary reaction partner to $^{210}$Pb.

The off-beam $E_\gamma$-$E_\gamma$ coincidence matrix was sorted using the software condition on the multiplicity of $\gamma$-rays $M_{\gamma\mathrm{Ge}} \geq 2$. Only events that occured outside of the macro pulse of the beam, 5 ms $\leq T \leq$ 20 ms, were considered in this matrix (see Figure 2.5 on page 15). No further conditions were required and the matrix was symmetrized.

The analysis of this matrix allowed to study $\gamma$ transitions depopulating long lived isomeric states populated in the nuclear reaction. Also $\gamma$ spectra from $\beta$- or $\alpha$-decay of unstable nuclei populated in the nuclear reaction could be investigated. States characterized by a half life between $T_{1/2} \sim 50$ $\mu$s and a few days could be identified using this matrix.

An example for a spectrum obtained from the off-beam matrix is shown in Figure 2.6 on page 18. The spectrum shows $\gamma$-rays coincident to the 921.0 keV transition that depopulates a long lived isomeric state in $^{208}$Bi [Mar86]. The relevant level

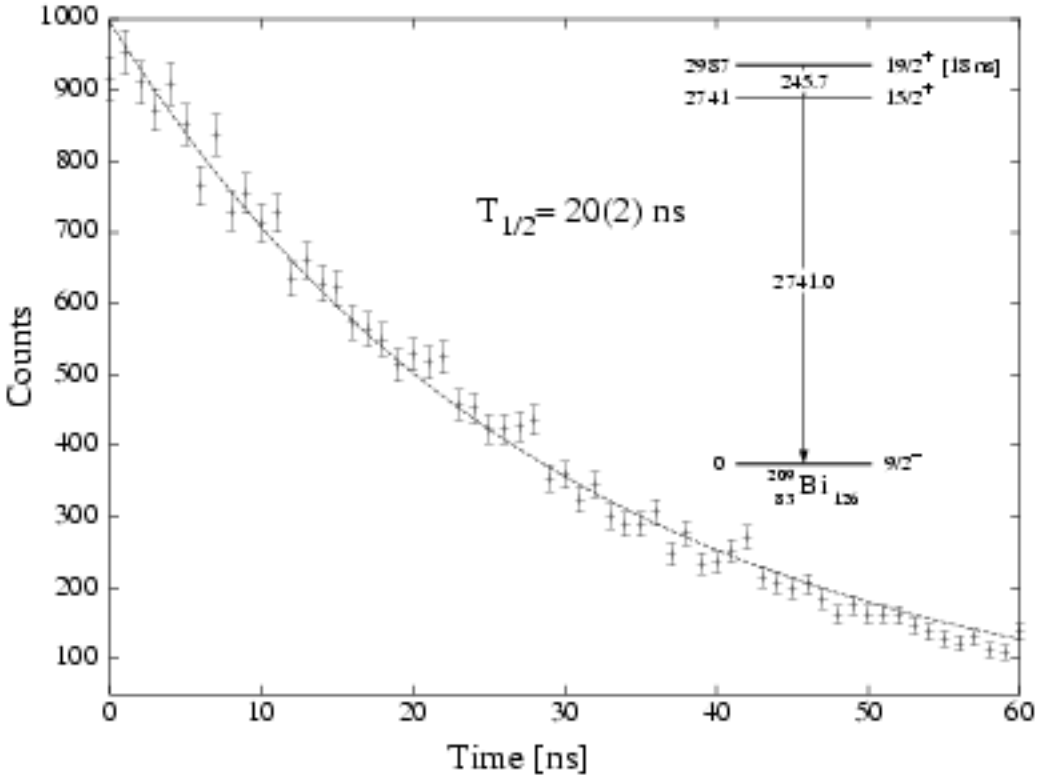


Figure 2.7 The time distribution of the 2741.0 keV $\gamma$-ray from the experiment with the $^{208}$Pb beam. The relevant partial level scheme of $^{209}$Bi is shown in the inset.

scheme of $^{208}$Bi nucleus is shown in the inset. The isomeric half life of the $10^-$ state is $T_{1/2} = 2.58(4)$ ms [Mar86]. The coincident $\gamma$-rays are evident in the spectrum.

Two $\underline{E_\gamma\text{-}T_\gamma}$ matrices were sorted for the two different measured times. The first included only events with $M_{\gamma\mathrm{Ge}} \geq 2$, that occured during the macro pulse of the beam 0 ms $\leq T \leq$ 5 ms. The additional requirement, specifying the time relation of the event relative to the reaction, was taken as for the prompt-prompt matrix. Energy and time, relative to the micro pulse that caused the reaction, of the same $\gamma$-ray (signals from the same detector) were put into this matrix. The analysis of this matrix allowed to check for isomers and measure their half life by the time distribution of the $\gamma$-rays that depopulate the isomer. The sensitivity of this measurement ranged from a few nanoseconds up to about 1 microsecond.

A representative time distribution derived in this way is shown in Figure 2.7 on page 19. It gives the time distribution of the 2741.0 keV transition in $^{209}$Bi. The corresponding partial level scheme of $^{209}$Bi [Mai83] can be found in the inset of the figure. The isomeric half life of the $19/2^+$ state could be determined as

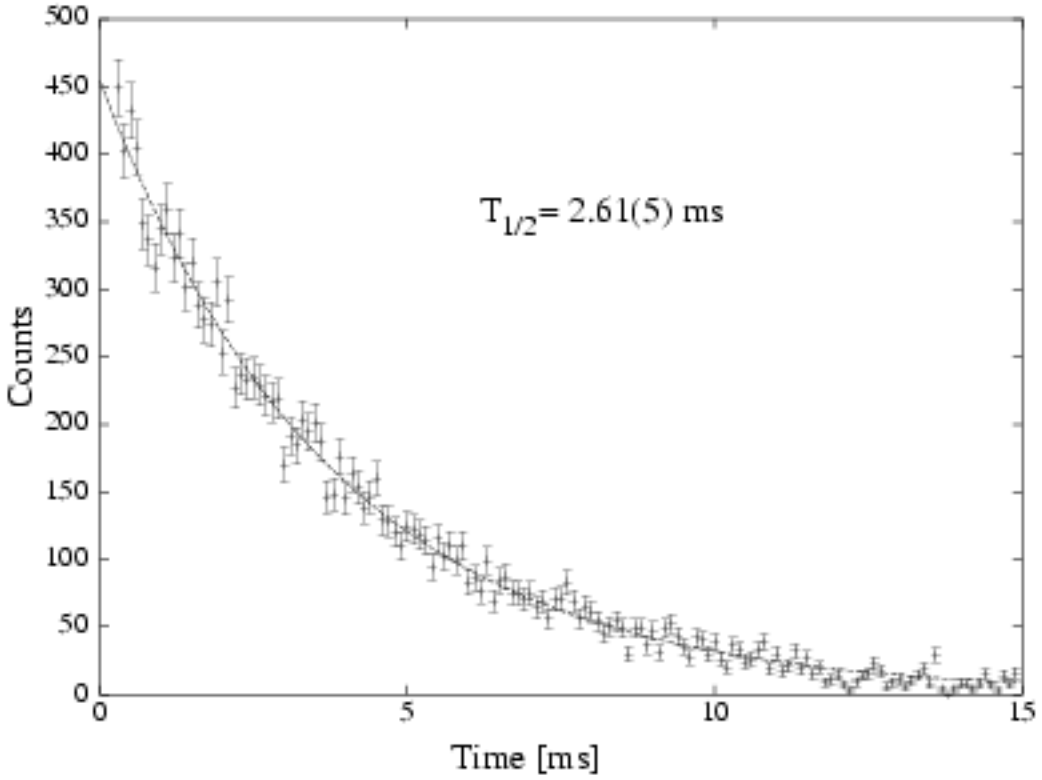


Figure 2.8 The time distribution of the 921.0 keV $\gamma$-ray in $^{208}$Bi. The spectrum is derived from the experiment with the $^{208}$Pb beam.

$T_{1/2} = 20(2)$ ns in agreement with the previous value of $T_{1/2} = 18(1)$ ns [Bee78].

The second $\gamma$-time matrix included only events, with $M_{\gamma\mathrm{Ge}} \geq 2$, that occured outside of the macro pulse of the beam 5 ms $\leq T \leq$ 20 ms. The $\gamma$-ray energy versus the time of event measured respectively to the end of the macro pulse of the beam were put into this matrix.

The analysis of this matrix allowed to determine isomeric half lives ranging from about 100 $\mu$s to about 20 ms.

As an example the time distribution of the 921.0 keV transition in $^{208}$Bi derived from this matrix is presented in Figure 2.8 on page 20. The relevant partial level scheme [Mar86] can be found in the inset of Figure 2.6 on page 18. The 921.0 keV transition depopulates the long lived $T_{1/2} = 2.58(4)$ ms isomeric state in $^{208}$Bi [Mar86]. The isomeric half life determined in the present measurement is $T_{1/2} = 2.61(5)$ ms.

# Chapter 3

# Results and Discussion

The experiments performed in this work revealed new experimental information on high spin states in several nuclei lying close to $^{208}$Pb. New excited states have been found in $^{210}$Pb. They result from the excitation of two valence neutrons outside of the doubly magic $^{208}$Pb core. The experimental results and a detailed discussion of $^{210}$Pb are presented in the first section. New high spin states in $^{209}$Pb and $^{207}$Tl, the nuclei with one valence neutron and one valence proton-hole outside of the $^{208}$Pb core have also been found. These levels result from the yrast states of the $^{208}$Pb core coupled to the valence neutron in $^{209}$Pb and the valence proton-hole in $^{207}$Tl. The second and third section consist of a review on these nuclei. New excited states could also be assigned to $^{205}$Tl. They are presented in the fourth section. In the last, fifth section the particle-octupole vibration coupling phenomenon is treated in detail. New interesting results on this subject are presented and discussed in the frame of a simple theoretical model.

In our experimental set up all Ge-detectors were positioned at 154° relative to the beam axis and therefore no angular distributions of $\gamma$-rays could be measured. In general, angular distributions of $\gamma$-rays were not yet evaluated with deep inelastic reactions. Therefore no spins and multipolarities could be determined from our experimental data.

A part of the results on $^{210}$Pb and $^{209}$Pb, presented in this chapter, have been published already [Rej97, Rej98]. The other results like the particle-octupole vibration coupling are the subject of further publication [Rej(a)]. New data of these experiments on $^{208}$Pb and Bi and Po isotopes are treated by the cooperating group at the Henryk Niedwodniczański Institute, Kraków [Wrz].

## 3.1 The nucleus $^{210}$Pb

The nucleus $^{210}$Pb has two neutrons outside the doubly magic $^{208}$Pb core. The low lying excited states of this nucleus are therefore expected to exhibit the simple structure of two particle excitations with the neutrons in the lowest shell-model orbitals $2g_{9/2}$, $1i_{11/2}$, $1j_{15/2}$, $3d_{5/2}$, $4s_{1/2}$, $2g_{7/2}$ and $3d_{3/2}$ (see Figure 1.2 on page 6). For excitations lying close to the yrast line only the high spin orbitals $2g_{9/2}$, $1i_{11/2}$, $1j_{15/2}$ have to be considered. The high energy, low spin orbitals are not likely to contribute to the high spin yrast states.

A set of yrast states has been identified above the $0^+$ ground state in $^{210}$Pb. These are $8^+$, $6^+$, $4^+$ and $2^+$ [Sjo80, Bohn81, Dec83]. They are depopulated by $\gamma$ rays of energy (80), 98, 298, 799.7 keV respectively [Sjo80, Bohn81, Dec83]. These states were identified to be members of the $\nu 2g_{9/2}^2$ multiplet. The $8^+$ and $6^+$ states are isomeric with half lives of 201 ns and 49 ns respectively [Dec83]. The energy of the $8^+ \rightarrow 6^+$ transition has not been measured. The adopted [Har81] energy of the $8^+$ state is 1278(5) keV and this uncertainty is transferred to the higher states.

In the present experiment we observed the previously known $\gamma$ rays of energy 298 keV and 799.7 keV in mutual coincidence. The two low energy E2 transitions, depopulating the $6^+$ and $8^+$ states, could not be observed. This was due to the high electron conversion probability for these transitions. The total conversion coefficient for the 98 keV $\gamma$ ray is 6.71 and for 80 keV 17.9.

The spectrum of prompt $\gamma$ rays coincident with the delayed 799.7 keV transition from $^{208}$Pb+$^{208}$Pb collisions is shown in Figure 3.1 on page 23. Five new transitions of energy 528.0, 1233.7, 640.4, 1346.0 and 981.0 keV were identified and assigned to $^{210}$Pb. The relative intensities measured in coincidence with the 799.7 keV line are given in Table 3.1 on page 24. The 803 keV transition, evident in this spectrum, belongs to the $^{206}$Pb nucleus which is the partner of $^{210}$Pb in the binary reaction. The individual coincidence relations between the five new $\gamma$ rays and their relative intensities establish four new high spin states in $^{210}$Pb above the $8^+$ isomer. The level scheme of $^{210}$Pb as observed in the present study is shown in Figure 3.2a on page 25.

The experiment does neither determine the multipolarity of the $\gamma$ transitions nor spins and parities of states. There is however clear and ample evidence, that deep inelastic reactions populate almost exclusively yrast states [Sch93, Sch93(a), Bro94, Bro96]. The yrast states, in nuclei in the $^{208}$Pb region, can be firmly predicted from the shell model. The following discussion of the excited states in $^{210}$Pb is based on the general knowledge and understanding of the simple shell-model states.

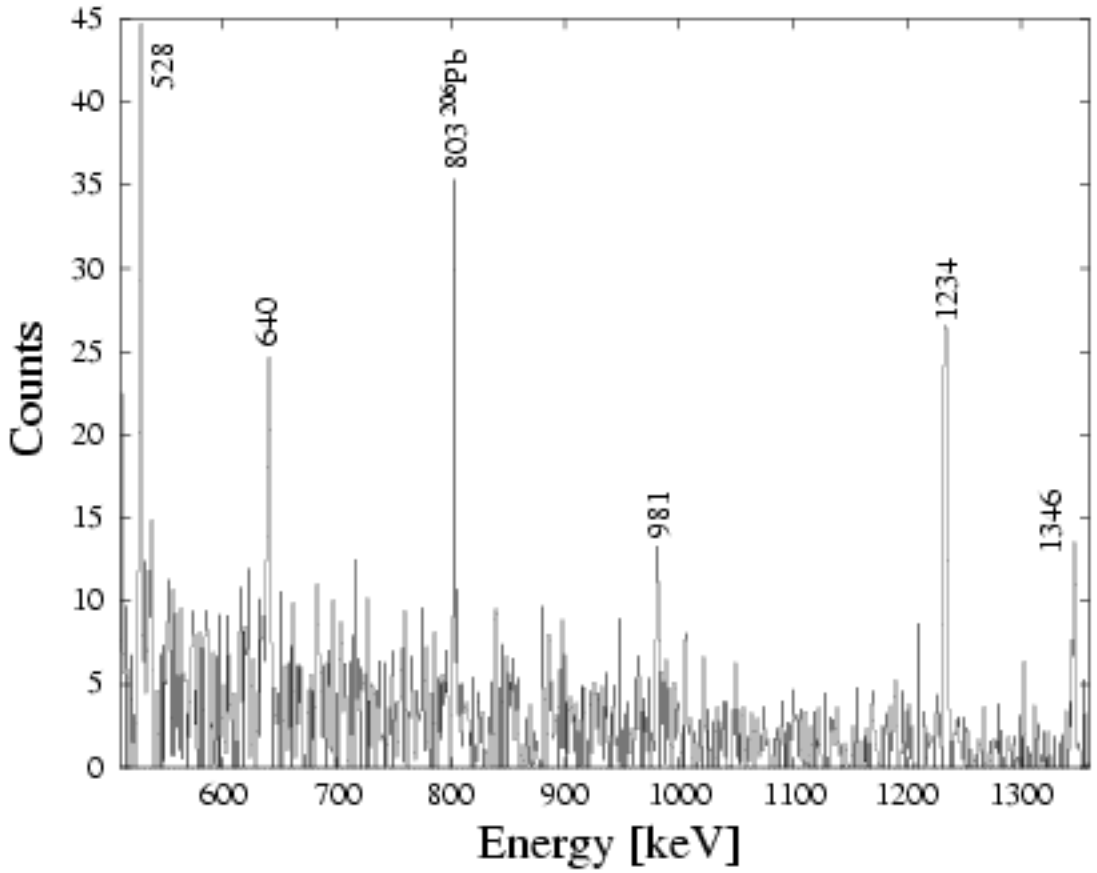


Figure 3.1 The spectrum of prompt $\gamma$ rays coincident with the delayed 799.7 keV transition in $^{210}$Pb.

In Figure 3.2b the unperturbed excitation energies of the configurations with two neutrons in the $2g_{9/2}$, $1i_{11/2}$ and $1j_{15/2}$ shell-model orbitals are shown. The single neutron energies were taken from experiment (see Figure 1.2 on page 6).

*Level at 1806 keV, $(10^+)$*

An extension to higher spin of the typical scheme $0^+, 2^+, 4^+, 6^+, 8^+$ for the $\nu 2g_{9/2}^2$ multiplet is not possible. Due to the Pauli principle, two like nucleons in the same shell-model orbital can couple only to states of even spin, and $8^+$ is the maximum in this case. The next configuration above $\nu 2g_{9/2}^2$ is $\nu 1i_{11/2}2g_{9/2}$, (see Figure 3.2b), that can couple to the maximum spin $10^+$. The $10^+$ state is expected to be the lowest level of this configuration. This is also the case for the very similar state of $\pi 2f_{7/2}1h_{9/2}$ in the $^{210}$Po nucleus [Man88, War91]. The $2f_{7/2}$ and $1h_{9/2}$ orbitals in $^{210}$Po are lower in spin by $1\hbar$ than the corresponding $2g_{9/2}$ and $1i_{11/2}$ orbitals in $^{210}$Pb. Also the orbital ($l$) and spin ($s$) angular momentum are parallel in the case of the $2f_{7/2}$ and $2g_{9/2}$ orbitals and antiparallel in for the $1h_{9/2}$ and $1i_{11/2}$ orbitals. The level observed at 1806 keV in the present experiment is also very likely the same as

Table 3.1 Energies and relative intensities of transitions assigned to $^{210}$Pb. The relative intensities have been determined from the spectrum in coincidence with the delayed 799.7 keV transition.

| $E_\gamma$ [keV] | $I_\gamma$ | $E_i$ [keV] | $I_i^\pi$ | $E_f$ [keV] | $I_f^\pi$ |
|---|---|---|---|---|---|
| 528.0(2) | 114 | 1806 | $(10^+)$ | 1278 | $8^+$ |
| 640.4(2) | 57 | 3152 | $(13^-)$ | 2512 | $(11^-)$ |
| 981.0(4) | 32 | 4133 | $(14^+)$ | 3152 | $(13^-)$ |
| 1233.7(2) | 122 | 2512 | $(11^-)$ | 1278 | $8^+$ |
| 1346.0(2) | 69 | 3152 | $(13^-)$ | 1806 | $(10^+)$ |

the $(10^+)$ level seen in the $^{208}$Pb(t, p) reaction at 1799(15) keV [Fly72]. Therefore we propose $(10^+)$ assignment for this level. The 528.0 keV $\gamma$ ray is then a stretched E2 transition of one neutron from $1i_{11/2}$ to $2g_{9/2}$ with the second neutron in the $2g_{9/2}$ orbital as a spectator.

*Level at 2512 keV, $(11^-)$*

The next higher lying configurations are $\nu 1i_{11/2}^2$ and $\nu 2g_{9/2}1j_{15/2}$ (see Figure 3.2b). The former one does not extend beyond spin $10^+$. The second $\nu 2g_{9/2}1j_{15/2}$ has $I \leq 12$. For this multiplet the $12^-$ state is expected about 0.5 MeV above the $11^-$ state. A very similar case has been found in the $^{148}$Gd nucleus for the corresponding levels of the $\nu 2f_{7/2}1i_{13/2}$ configuration [Pii90]. The parallel neutron spins give rise to a repulsive interaction in the unnatural parity $12^-$ state. There is, however, a still more important fact. The $12^-$ state has to be pure $\nu 2g_{9/2}1j_{15/2}$. The large admixture of $\nu 2g_{9/2}^2 \times 3^-(^{208}\mathrm{Pb})$ to the $\nu 2g_{9/2}1j_{15/2}$ configuration [Ham69] (see also section 3.5) can only contribute to the states of $I \leq 11$, due to the Pauli principle. The pure $\nu 1j_{15/2}$ orbital lies much higher than the effective, mixed one. We propose the assignment $(11^-)$ for the state at 2512 keV excitation energy. $^{148}$Gd with two neutrons outside of the doubly magic $^{146}$Gd core shows in general similar features as $^{210}$Pb, in particular as the high spin neutron orbitals there differ only by a one unit lower orbital angular momentum.

The observed 1233.7 keV $\gamma$ ray is interpreted as a stretched E3 transition. The decay constant $\lambda(E3, 11^- \rightarrow 8^+) = 2.7 \times 10^8$ s$^{-1}$ was calculated from the measured $B(E3, 15/2^- \rightarrow 9/2^+) = 26$ W.u. [Ell67] in $^{209}$Pb. This gives a very low upper limit for the unobserved E1 transition to the $10^+$ state, $\lambda(E1) \leq 5 \times 10^{-8}$ W.u.. For the

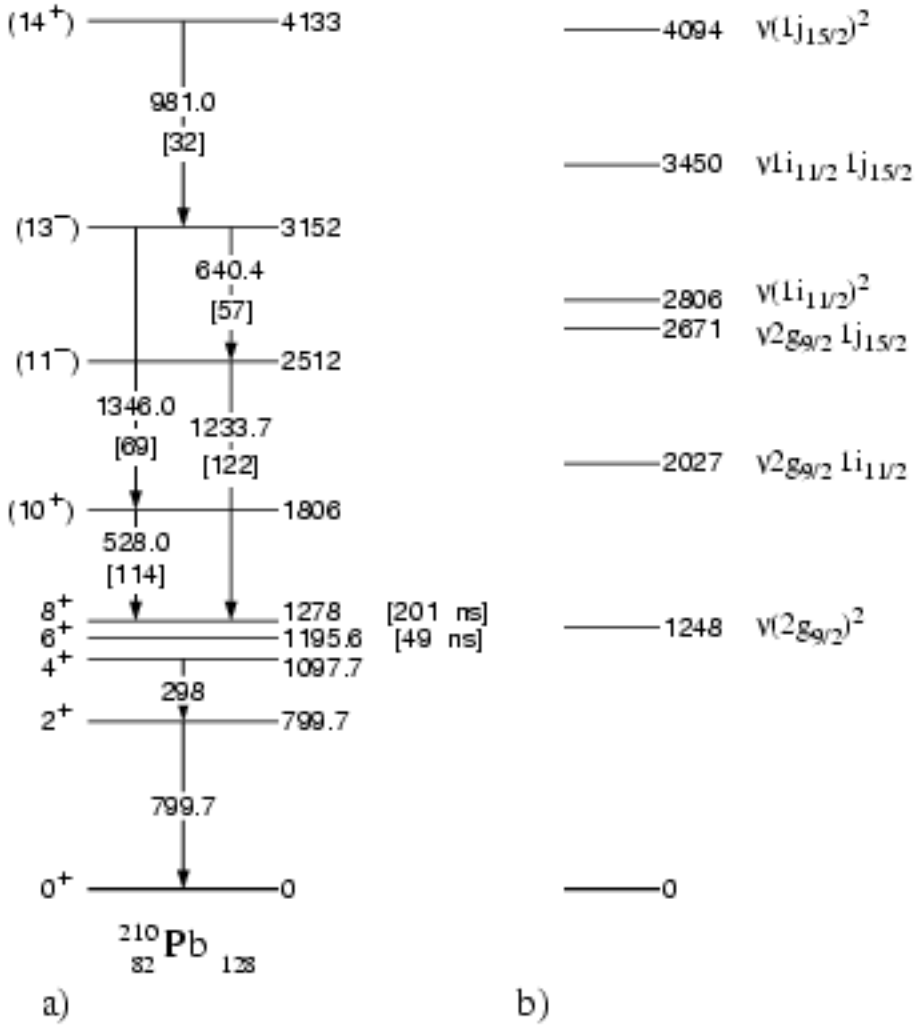


Figure 3.2 The level scheme of $^{210}$Pb a) experiment, in square brackets [ ] $\gamma$-intensities in coincidence with 799.7 keV line, b) energies of unperturbed two neutron states. All energies are given in keV. The proposed spin-parity assignments, given in brackets, follow from systematics and model assumptions (see also text).

similar E1 decay of the lowest $8^+$ state in $^{208}$Pb to the $7^-$ state a hindrance factor of $1 \times 10^{-8}$ has been measured [Sch97]. The retardation of the E1 transition from the $11^-$ to the $10^+$ state can be viewed as a manifestation of the purity of the wave functions.

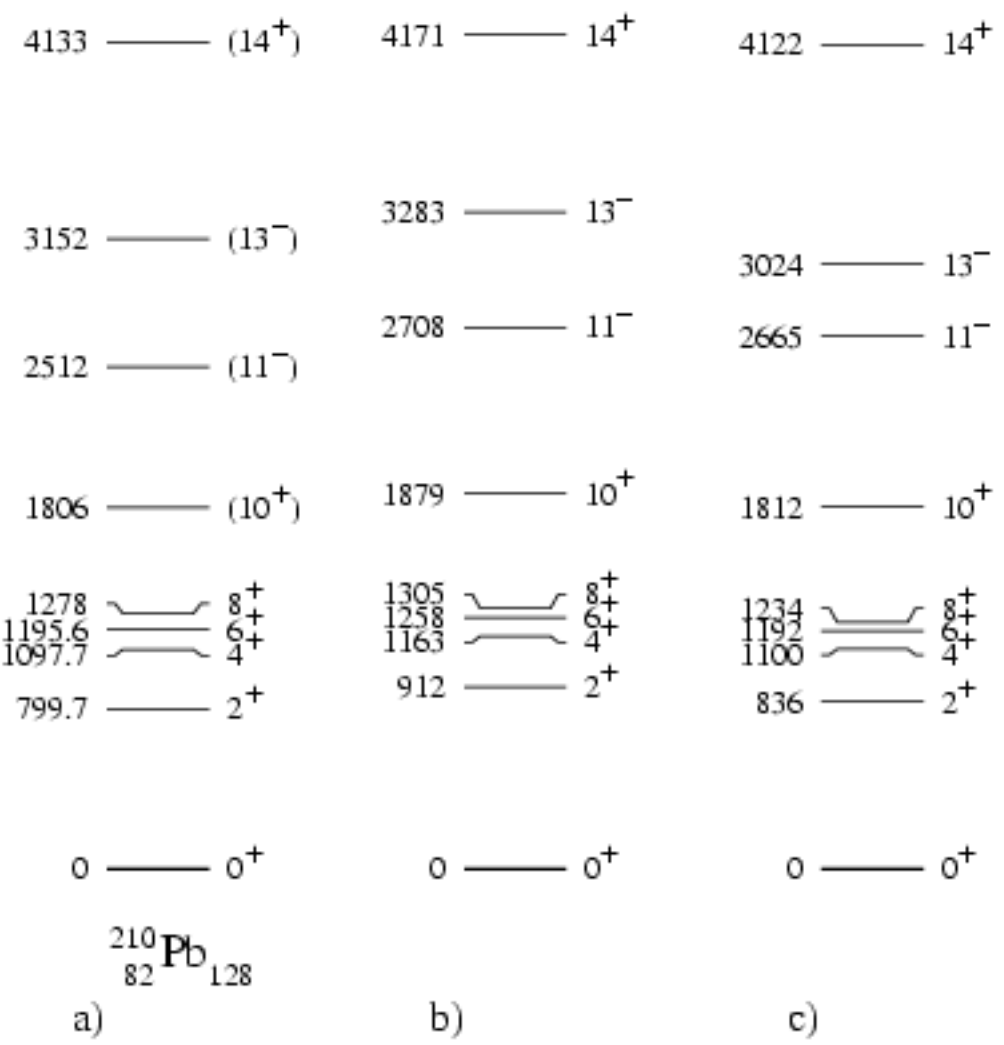


Figure 3.3 The experimental level scheme of $^{210}$Pb (a) compared to the shell model calculations (b) using SDI matrix elements of residual interaction and (c) using realistic matrix elements of residual interaction (see also text). All energies are given in keV.

*Level at 3152 keV, $(13^-)$*

The next configuration is $\nu 1i_{11/2}1j_{15/2}$. It is very similar to the known $\pi 1h_{9/2}1i_{13/2}$ multiplet in $^{210}$Po [Man88, War91]. Here the corresponding orbitals differ again only by one unit in orbital angular momentum. From this similarity the state of the highest spin, $13^-$, and natural parity comes lowest in energy. We propose the assignment $(13^-)$ for the state at 3152 keV excitation energy. The E3 transition, that depopulates this state feeding the $10^+$ state, was calculated to proceed with

the decay constant $\lambda(E3, 13^- \rightarrow 10^+) = 3.1 \times 10^8$ s$^{-1}$ from the measured [Ell67] $B(E3, 15/2^- \rightarrow 9/2^+) = 26$ W.u. in $^{209}$Pb. The E2 transition to the $11^-$ state was calculated, assuming a pure $\nu 2g_{9/2}1j_{15/2}$ configuration of the $11^-$ state, to proceed with $\lambda(E2, 13^- \rightarrow 11^-) = 1.0 \times 10^8$ s$^{-1}$. This leads to a branching ratio of 75% E3 and 25% E2. However, a little admixture of the $\nu 1i_{11/2}1j_{15/2}$ configuration in the $11^-$ state is expected. With the assumption that this admixture is 1%, the E2 decay constant increases to $\lambda(E2, 13^- \rightarrow 11^-) = 1.8 \times 10^8$ s$^{-1}$. This gives a branching ratio of 63% E3 and 37% E2. Therefore a comparable strength of the transitions as observed experimentally is acceptable. The intensity of the 640 keV E2 transition is uncertain, because it is a doublet.

*Level at 4133 keV, $(14^+)$*

The highest observed level is proposed to be the $(14^+)$ state of the $\nu 1j_{15/2}^2$ multiplet. It is the maximum possible spin to be reached without exciting the $^{208}$Pb core. Its E3 decay to $11^-$ is calculated to proceed with $\lambda(E3, 14^+ \rightarrow 11^-) = 1.5 \times 10^9$ s$^{-1}$. Only the E1 decay to $13^-$ has been observed. This gives the rather common value of $\lambda(E1, 14^+ \rightarrow 13^-) \geq 5 \times 10^{-7}$ W.u.. The $12^+$ level in $^{148}$Gd of analogous structure shows also 97% E1 and only 3% E3 decay [Pii90]. However, the $\gamma$-ray energies favour the E3 decay much more there.

The $^{208}$Pb$(\alpha, ^2$He) reaction has been studied [Neu93] and 9 states in $^{210}$Pb identified with a resolution of 200 keV. This reaction populates preferentially states with a stretched configuration of the two neutrons. Therefore the authors assigned the levels that they found to the nearest calculated shell model states with a stretched configuration. Assignments of $10^+$ and $13^-$ to states at 1.80 and 3.13 MeV agree well with the present results. Doublets of states have been found at 2.52 and 3.99 MeV and identified in part with the $11^-$ and $14^+$ states. The energy fits well for the $11^-$ level but less well for our $(14^+)$ 4.133 MeV state.

In analogy to $^{148}$Gd [Pii90] the $11^-$ and $14^+$ states can be interpreted in an alternative way, namely as an octupole and double octupole excitation on top of the $(\nu 2g_{9/2}^2,\ 8^+)$ state. The $1j_{15/2}$ orbital has a large admixture of $2g_{9/2} \times 3^-$. Therefore the $1j_{15/2}2g_{9/2}$ and $1j_{15/2}^2$ configurations contain $2g_{9/2}^2 \times 3^-$ and $2g_{9/2}^2 \times (3^-)^2$ components of about the same size. The difference between $^{148}$Gd and $^{210}$Pb is only quantitative. In $^{148}$Gd the octupole is stronger and in $^{210}$Pb the single-particle structure dominates.

In order to check our interpretation of the newly identified high spin states in $^{210}$Pb we performed a mathematically strict calculation using the schematic Surface Delta Interaction (SDI) [Pop88]. The calculations have been made using the

Table 3.2 States in $^{210}$Pb calculated with the Surface Delta Interaction. The energies, spins and configurations are given. The SDI strength parameter $A_1 = 0.13$ MeV was used (see text).

| $E_x$ | $I^\pi$ | Configuration(%) | | | | | |
|---|---|---|---|---|---|---|---|
| [keV] | | $2g_{9/2}^2$ | $2g_{9/2}1i_{11/2}$ | $2g_{9/2}1j_{15/2}$ | $1i_{11/2}^2$ | $1i_{11/2}1j_{15/2}$ | $1j_{15/2}^2$ |
| 0 | $0^+$ | 70.3 | – | – | 18.1 | – | 11.6 |
| 912 | $2^+$ | 77.7 | 1.1 | – | 4.5 | – | 2.2 |
| 1163 | $4^+$ | 91.3 | 1.5 | – | 1.2 | – | 0.6 |
| 1258 | $6^+$ | 96.5 | 1.2 | – | 0.4 | – | 0.2 |
| 1305 | $8^+$ | 98.5 | 0.9 | – | 0.1 | – | 0.05 |
| 1879 | $10^+$ | – | 99.2 | – | 0.6 | – | 0.2 |
| 2708 | $11^-$ | – | – | 98.5 | – | 1.2 | – |
| 3283 | $13^-$ | – | – | – | – | 100. | – |
| 4094 | $14^+$ | – | – | – | – | – | 100. |

RITSSCHIL shell-model code [Zwa85]. The theoretical results and experimental data are compared in Figure 3.3 in columns (b) and (a), respectively. The SDI strength parameter $A_1 = 0.13$ MeV has been used. This value is similar to $A_1 = 0.16$ MeV, determined by Poppelier at al. [Pop88] from a fit to many states in nuclei in the $^{208}$Pb region. However, the Coulomb pairing interaction was not considered there. We reduced the $A_1$ value to reproduce the two neutron binding energy and simultaneously have good agreement with the energies of the $2^+$, $4^+$ and $6^+$ excited states. The calculated binding energy of $^{210}$Pb is $-9.219$ MeV and the measured is $-9.122$ MeV relative to $^{208}$Pb. The calculations included the $\nu(2g_{9/2},\ 1i_{11/2},\ 1j_{15/2},\ 3d_{5/2},\ 4s_{1/2},\ 2g_{7/2},\ 3d_{3/2})$ neutron orbitals with the restriction that only one neutron was allowed to occupy the $\nu(3d_{5/2},\ 4s_{1/2},\ 2g_{7/2},\ 3d_{3/2})$ orbitals. The experimental energies (see Figure 1.2 on page 6) were used for the single neutron orbitals.

The calculated energies are in very good agreement with the experimental data. The contribution of the high spin neutron multiplets to the wave function of the calculated states can be found in Table 3.2. In general very little mixing is calculated for the yrast states of the $^{210}$Pb nucleus. The ground state has about 70% of the $\nu 2g_{9/2}^2$ configuration with considerable admixtures of 18% $\nu 1i_{11/2}^2$ and 12% $\nu 1j_{15/2}^2$. The first excited $2^+$ state has 78% of the $\nu 2g_{9/2}^2$ configuration. The remaining part

Table 3.3 The effective, diagonal residual interaction matrix elements for two neutron states. The matrix elements were extracted from the measured energy spectrum of $^{210}$Pb assuming pure wave functions.

| $i$ | $j$ | $I^\pi$ | $\langle ij\|V_{eff}\|ij\rangle$ [MeV] |
|---|---|---|---|
| $\nu 2g_{9/2}$ | $\nu 2g_{9/2}$ | $0^+$ | $-1.248$ |
| $\nu 2g_{9/2}$ | $\nu 2g_{9/2}$ | $2^+$ | $-0.448$ |
| $\nu 2g_{9/2}$ | $\nu 2g_{9/2}$ | $4^+$ | $-0.150$ |
| $\nu 2g_{9/2}$ | $\nu 2g_{9/2}$ | $6^+$ | $-0.052$ |
| $\nu 2g_{9/2}$ | $\nu 2g_{9/2}$ | $8^+$ | $+0.031$ |
| $\nu 2g_{9/2}$ | $\nu 1i_{11/2}$ | $10^+$ | $-0.221$ |
| $\nu 2g_{9/2}$ | $\nu 1j_{15/2}$ | $11^-$ | $-0.151$ |
| $\nu 1i_{11/2}$ | $\nu 1j_{15/2}$ | $13^-$ | $-0.298$ |
| $\nu 1j_{15/2}$ | $\nu 1j_{15/2}$ | $14^+$ | $+0.039$ |

of the wave function is however much more fragmented than it is for the $0^+$ state. The wave functions of the states with $I \geq 4$ are rather pure. The main component of the wave function contributes about 91% for the $4^+$ state and more than 97% for the higher spin states. The dominant component corresponds in each case to the two neutron state with the closest lying unperturbed energy, as discussed earlier in this section.

In Figure 3.3c also calculations using realistic matrix elements of the residual interaction are given for comparison. The residual interaction was originally derived by Kuo and Herling [Kuo68, Kuo71] from the measured interaction between free nucleons and later modified by Warburton and Brown [War91] to give a better description of nuclear properties (see also Section 4.1). Very good agreement between experiment (column a) and calculations (column c) is evident in Figure 3.3.

The measurement of the spectrum of a two particle nucleus like $^{210}$Pb allows a direct determination of the effective residual two body interaction. The effective residual interaction matrix elements of the two neutrons have been calculated assuming pure wave functions for the excited states in $^{210}$Pb. The calculated diagonal matrix elements are given in Table 3.3.

## 3.2 The nucleus $^{209}$Pb

The $^{209}$Pb nucleus consists of 82 protons and 127 neutrons and can be described in terms of a particle-core model as one valence neutron outside of doubly magic $^{208}$Pb. $^{209}$Pb has been studied experimentally by the (d, p) reaction (neutron stripping) on the stable $^{208}$Pb nucleus [Mar91], the (p, d) reaction (neutron pick up) on the radioactive $^{210}$Pb target [Igo71], the (t, $\alpha$) reaction (proton pick up) on $^{210m}$Bi with a radioactive beam and target [Han77], and the two neutron stripping reaction $^{207}$Pb(t, p) [Fly71]. $\gamma$ transitions in $^{209}$Pb have only been measured with the $^{208}$Pb(d, p$\gamma$) reaction [Dün75] and following the $\beta$ decay of $^{209}$Tl [Kou89] All the above mentioned reactions populate single particle states (see Figure 1.2) or selected two particle one hole states.

In the present experiment we could identify new $\gamma$ transitions in $^{209}$Pb from the spectra in prompt coincidence with the previously known $\gamma$ rays 1422.7 keV, 779.2 keV and 643.5 keV [Mar91]. The spectra of $\gamma$ rays measured in prompt coincidence with the 1422.7 keV transition in $^{209}$Pb from the experiments with the $^{208}$Pb and $^{136}$Xe beam are shown in Figure 3.4. Coincident transitions from the binary reaction partner $^{207}$Pb or $^{135}$Xe are evident in the spectra. Also transitions in the nuclei $^{205}$Pb and $^{134}$Xe that result from the reaction partner by the evaporation of one neutron are present in the corresponding spectra. The $\gamma$ transitions assigned to $^{209}$Pb are listed in Table 3.4. Relative intensities from the experiment with the $^{208}$Pb beam are given. The mutual coincidence relations between the observed $\gamma$ transitions and their relative intensities establish the high spin states in $^{209}$Pb. The yrast level scheme of excited states in $^{209}$Pb as observed in the present study is presented in Figure 3.5a on page 32.

The deep inelastic reactions are known to populate almost exclusively the yrast states [Sch93, Sch93(a), Bro94, Bro96]. However, in the present study, it was possible to observe a weak population of non yrast states apparently via the quasielastic process. We observed the previously known [Mar91] cascade of $\gamma$ rays of energies 1567 keV, 465 keV and 285 keV feeding the $9/2^+$ ground state of $^{209}$Pb. The corresponding levels at 1567 keV and 2032 keV are known to be the $3d_{5/2}$ and $4s_{1/2}$ single neutron states. These are strongly populated in neutron transfer. The 285 keV transition deexcites a $3/2^-$ level at 2317 keV [Dün75]. This state is described as $\nu 2g_{9/2} \times 3^-(^{208}\mathrm{Pb})$ excitation. These low spin states are not included in Figure 3.5a and Table 3.4.

A number of weak transitions could be assigned to $^{209}$Pb on the basis of prompt $\gamma$-$\gamma$ coincidence data but could not be definitely placed in the level scheme due to

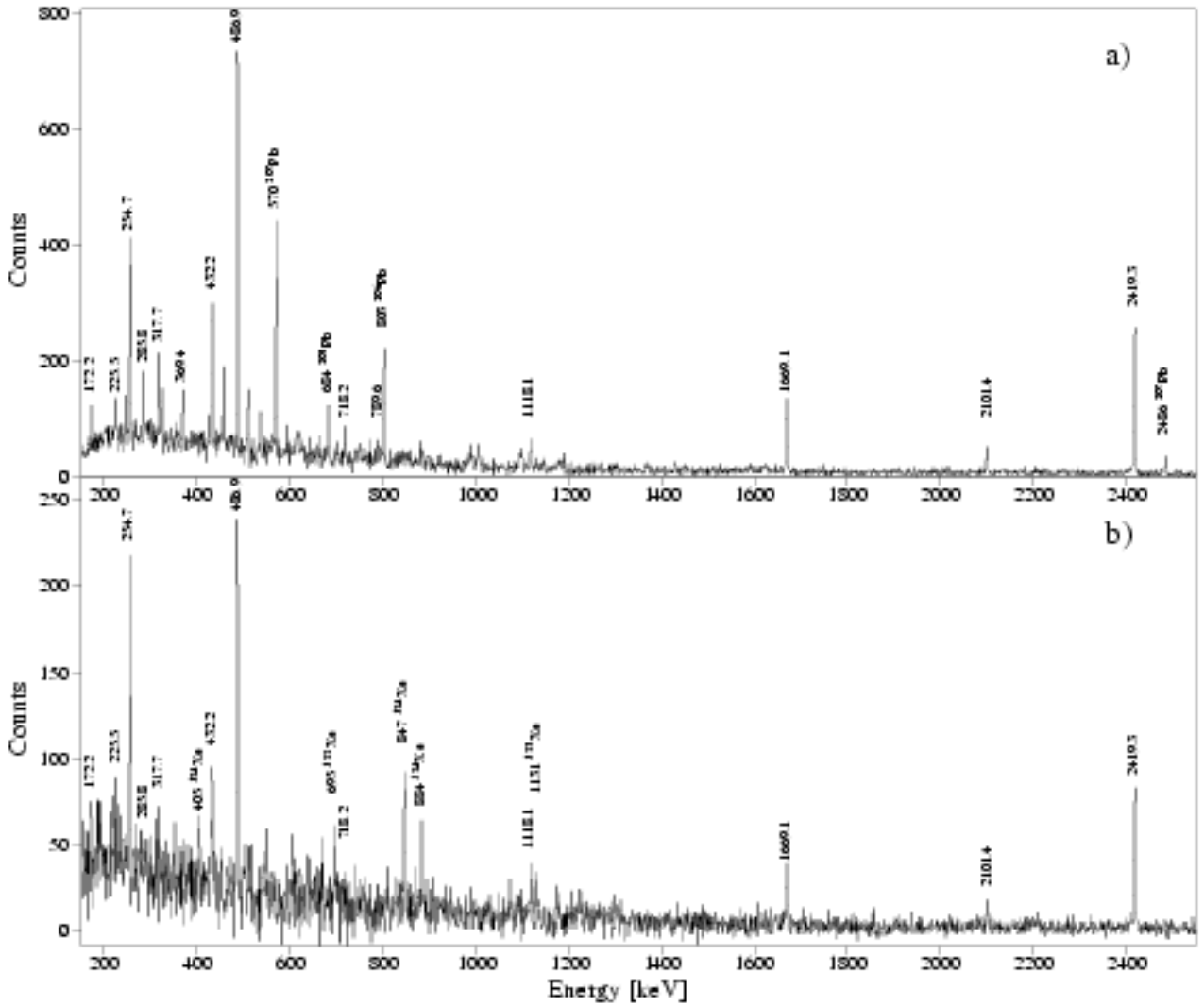


Figure 3.4 Spectrum of prompt $\gamma$-rays in coincidence with the 1422.7 keV line from the experiments with a) $^{208}$Pb beam, b) $^{136}$Xe beam.

a lack of statistics. Of these a 1100 keV transition is certainly located above the 3842 keV level and likely feeds the 4329 keV state. A weak 1178 keV transition and a cascade of 790 keV and 458 keV $\gamma$-rays were observed on top of the 3842 keV excited state.

There were no experimental data on angular distributions of the $\gamma$ transitions or any other direct information on the spins of the observed levels or multipolarities of the transitions. In the following we discuss tentative spin assignments based on the combination of the available experimental information and on theoretical expectations, that are reliable for the lower lying yrast states.

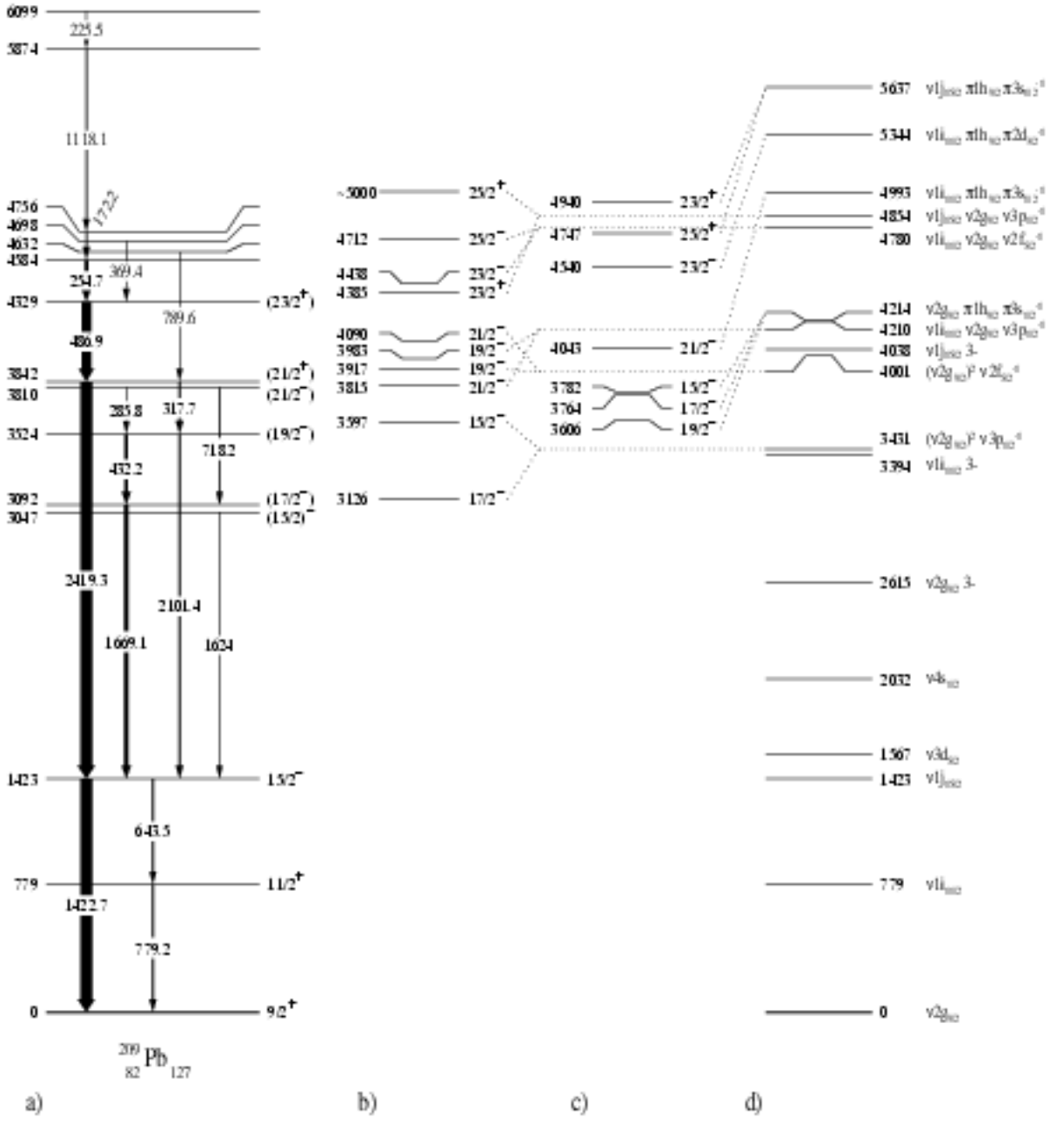


Figure 3.5 Comparison of the experimental a) level scheme of $^{209}$Pb with shell-model expectations. Column d) shows the unperturbed energies of the relevant configurations. Columns b) and c) give the energies calculated for selected high spin states with residual interactions but without configuration mixing; neutron excitations of $^{208}$Pb are shown in b) and proton excitations in c). All energies are given in keV. The proposed spin-parity assignments, given in brackets, follow from systematics and model assumptions (see also text).

Table 3.4 Energies and intensities of $\gamma$-transitions in $^{209}$Pb. Relative intensities in prompt coincidence with the 1422.7 keV transition from the experiment with the $^{208}$Pb beam are presented. The last 3 transitions marked by † are from coincidences with the 2419.3 keV line. Energy and spin of the decaying levels are also given. ‡ - Multiple line, intensity uncertain.

| $E_\gamma$ [keV] | $I_\gamma$ | $E_i$ [keV] | $I_i^\pi$ | $E_f$ [keV] | $I_f^\pi$ |
|---|---|---|---|---|---|
| 172.2(3) | 12(2) | 4756 | | 4584 | |
| 225.5(2) | 10(2) | 6099 | | 5874 | |
| 254.7(1) | 33(3) | 4584 | | 4329 | $(23/2^+)$ |
| 285.8(3) | 9(2) | 3810 | $(21/2^-)$ | 3524 | $(19/2^-)$ |
| 317.7(2) | 18(2) | 3842 | $(21/2^+)$ | 3524 | $(19/2^-)$ |
| 369.4(2) | 9(2) | 4698 | | 4329 | $(23/2^+)$ |
| 432.2(3) | 31(10)‡ | 3524 | $(19/2^-)$ | 3092 | $(17/2^-)$ |
| 486.9(1) | 83(5) | 4329 | $(23/2^+)$ | 3842 | $(21/2^+)$ |
| 718.2(3) | 10(1) | 3810 | $(21/2^-)$ | 3092 | $(17/2^-)$ |
| 789.6(4) | 5(1) | 6432 | | 3842 | $(21/2^+)$ |
| 1118.1(2) | 11(2) | 5874 | | 4756 | |
| 1624(1) | $\leq 5$ | 3047 | $(15/2)^-$ | 1423 | $15/2^-$ |
| 1669.1(2) | 33(3) | 3092 | $(17/2^-)$ | 1423 | $15/2^-$ |
| 2101.4(3) | 17(2) | 3524 | $(19/2^-)$ | 1423 | $15/2^-$ |
| 2419.3(1) | 100(7) | 3842 | $(21/2^+)$ | 1423 | $15/2^-$ |
| | | | | | |
| 643.5(2) | 13(2)† | 1423 | $15/2^-$ | 779 | $11/2^+$ |
| 779.2(2) | 14(2)† | 779 | $11/2^+$ | 0 | $9/2^+$ |
| 1422.7(1) | 100(7)† | 1423 | $15/2^-$ | 0 | $9/2^+$ |

The experimental level scheme of the $^{209}$Pb nucleus, as deduced in the present study, is shown in Figure 3.5a. Column d shows the excitation energies of the unperturbed single-particle and two particle-one hole configurations, that are relevant for the discussion of the yrast states. The single neutron energies were taken from experiment (see Figure 1.2 on page 6).

Empirical shell-model (ESM) calculations have been performed to explore the

structure of the excited states in $^{209}$Pb. The general idea of this approach is to consider only pure configurations. But the residual interaction is taken from experimental energies and therefore includes energy shifts due to configuration mixing. This ESM approach has been applied to the neighbouring nucleus $^{209}$Bi [Cle74, Mai83]. It gave a good description of the states, that in this case result from the coupling of one proton to the one particle-one hole excitations of the $^{208}$Pb core.

The calculations included those two particle-one hole configurations that result from one particle-one hole excitations of the doubly magic $^{208}$Pb core nucleus coupled to the valence neutron in the $\nu(2g_{9/2},\ 1i_{11/2},\ 1j_{15/2})$ shell-model orbitals. Proton and neutron particle-hole excitations of the $^{208}$Pb core were considered. As the low lying yrast states in $^{209}$Pb are expected to be of quite pure structure, the ESM calculations without configuration mixing should be fairly realistic.

The empirical shell-model calculations used the effective diagonal two body matrix elements (TBME) of the residual interaction that could be extracted from experimental data on the neighbouring nuclei. The TBME for the neutron-neutron multiplets were taken from the $^{210}$Pb spectrum [Rej97] (see also section 3.1), for the proton-neutron multiplets from the $^{210}$Bi spectrum [Bro92] and for the one particle-one hole multiplets from $^{208}$Pb [Rej95, Sch95]. The matrix elements for the neutron-proton hole multiplets were extracted from experimental data [Mar86] and if not possible used as calculated by Kim and Rasmussen [Kim64]. The list of two-body matrix elements of residual interaction as used in our present ESM calculations is presented in Tables 6.1 and 6.2.

The three body hamiltonian matrix element of the residual interaction can be expressed in terms of the corresponding two body matrix elements [Bohr69, (p. 73)] and it is given by Equation 3.1.

$$
\begin{aligned}
&\left\langle (j_1 j_2)_{J_c'}, j_3; J | H | (j_1 j_2)_{J_c}, j_3; J \right\rangle = \\
&= (\epsilon_{j_1} + \epsilon_{j_2} + \epsilon_{j_3})\delta_{J_c', J_c} + \langle j_1 j_2; J_c' | V_{12} | j_1 j_2; J_c \rangle\, \delta_{J_c', J_c} \\
&+ \sum_{J_{13}} (-1)^{J_c' + J_c} \sqrt{(2J_c'+1)(2J_c+1)}(2J_{13}+1) \times \\
&\times \left\{ \begin{array}{ccc} j_1 & j_2 & J_c' \\ J & j_3 & J_{13} \end{array} \right\} \left\{ \begin{array}{ccc} j_1 & j_2 & J_c \\ J & j_3 & J_{13} \end{array} \right\} \langle j_1 j_3; J_{13} | V_{13} | j_1 j_3; J_{13} \rangle \qquad (3.1) \\
&+ \sum_{J_{23}} \sqrt{(2J_c'+1)(2J_c+1)}(2J_{23}+1) \times \\
&\times \left\{ \begin{array}{ccc} j_2 & j_1 & J_c' \\ J & j_3 & J_{23} \end{array} \right\} \left\{ \begin{array}{ccc} j_2 & j_1 & J_c \\ J & j_3 & J_{23} \end{array} \right\} \langle j_2 j_3; J_{23} | V_{23} | j_2 j_3; J_{23} \rangle
\end{aligned}
$$

where:
$j_1$, $j_2$ and $j_3$ are the spins of the particles and holes, $J_c$, $J'_c$, $J_{13}$ and $J_{23}$ are possible intermediate spins and $J$ is the spin of the level.

Diagonalization in $J_c$, $J'_c$ gives the wave functions and energies of the excited states. Figure 3.5 shows the results of these calculations for neutron excitations of $^{208}$Pb in column b and for proton core excitations in column c. The highly mixed collective octupole state in $^{208}$Pb cannot be included in these calculations. The associated levels in $^{209}$Pb are better described by the particle–vibration coupling model [Ham69, Ham70, Bohr75, (p. 416)]. They will be treated in detail in section 3.5 together with the other particle-octupole states in neighbouring nuclei found in this experiment.

The following discussion of the excited states observed in the $^{209}$Pb nucleus is made with the help of columns b—d in Figure 3.5. The three lowest levels observed in the experiment are the single neutron $2g_{9/2}$, $1i_{11/2}$ and $1j_{15/2}$ states. These neutron shell-model orbitals coupled to the yrast states of the $^{208}$Pb core nucleus form also the higher yrast states of $^{209}$Pb. The low spin neutron shell-model orbitals $3s_{1/2}$ and $3d_{5/2}$ are not important for the high spin states.

*Level at 3047 keV, $(15/2)^-$*

The lowest $15/2^-$ state at 1423 keV excitation energy contains, besides the single neutron $1j_{15/2}$ configuration, about 30% of the $\nu 2g_{9/2} \times 3^-(^{208}\mathrm{Pb})$ configuration. This is deduced from the missing strength in the $l = 7$ neutron transfer from $^{208}$Pb [Igo69] and the strength of its E3 decay, $B(E3, 15/2^- \rightarrow 9/2^+) = 26$ W.u. [Ell67]. The next level at 3047 keV excitation energy has been assigned to be $(15/2)^-$ [Dün75] too. It contains very likely most of the $\nu 2g_{9/2} \times 3^-(^{208}\mathrm{Pb})$ configuration with $\nu 1j_{15/2}$ as main admixture. An M1 transition to the lower $15/2^-$ state should dominate, as it can proceed with strong diagonal matrix elements. The 1624 keV transition is indeed the only decay observed experimentally.

*Level at 3092 keV, $(17/2^-)$*

We identify the level observed at 3092 keV excitation energy with the 3100(5) keV state excited in $^{207}$Pb(t, p) with $l = 8$ [Fly71]. The calculations firmly predict the $17/2^-$ state with the configuration $\nu 2g^2_{9/2}3p^{-1}_{1/2}$ to become yrast at 3126 keV excitation energy. The $^{207}$Pb(t, p) transfer reaction is the only one that populates this state in agreement with the proposed configuration.

The $l = 8$ transfer in the (t, p) reaction implies the transfer of two neutrons

in the $\nu 2g_{9/2}$ shell-model orbital coupled to $8^+$. As the configuration of the target nucleus $^{207}$Pb is $\nu 3p_{1/2}^{-1}$, a spin of $15/2^-$ or $17/2^-$ can result. The strong population of this level in the deep inelastic reaction and its $\gamma$ decay support firmly that this is an yrast state. Therefore the $17/2^-$ assignment is highly favoured. The energy of this state is lowered relative to the unperturbed energy by about 350 keV due to the attractive interaction of both $2g_{9/2}$ neutrons in the $(\nu 2g_{9/2}3p_{1/2}^{-1},\ 5^-)$ excitation of the $^{208}$Pb core nucleus [Sch93, Rej95]. In fact the $5_1^-$ excited state of $\nu 2g_{9/2}3p_{1/2}^{-1}$ in $^{208}$Pb is yrast and its excitation energy is 3198 keV which compares well to the $17/2^-$ energy of 3092 keV observed in $^{209}$Pb.

*Level at 3524 keV, $(19/2^-)$*

The next state at 3524 keV excitation energy is interpreted as $\nu 2g_{9/2}\pi 1h_{9/2}3s_{1/2}^{-1}$ coupled to the maximum angular momentum $19/2^-$ possible for this configuration. We identify this state with the 3530(5) keV state populated strongly in the $^{210m}$Bi(t, $\alpha$) proton pick up reaction [Han77] from the $(\nu 2g_{9/2}\pi 1h_{9/2},\ 9^-)$ state in $^{210}$Bi. The calculations (Figure 3.5c) predict this state to be yrast at 3606 keV excitation energy, about 80 keV higher than the experimentally observed level. The 80 keV downward energy shift, with respect to the calculated energy, is likely due to the sizeable admixture of the $\nu 2g_{9/2}^2 2f_{5/2}^{-1}$ configuration in the $19/2^-$ state similarly to the $5_2^-$ state in $^{208}$Pb core nucleus, for which in addition to the $\pi 1h_{9/2}3s_{1/2}^{-1}$ main configuration, a large admixture of $\nu 2g_{9/2}2f_{5/2}^{-1}$ was reported [Sch93, Rej95]. The $\gamma$ decay of the $19/2^-$ state has to proceed through small admixtures of the wave functions, as it is forbidden for the main configuration.

The spectrum of the $^{210m}$Bi(t, $\alpha$) reaction shows another strong transition establishing a level at 3657 keV [Han77] and no other lines in this region. Therefore this level is most likely the $17/2^-$ state of the $\nu 2g_{9/2}\pi 1h_{9/2}3s_{1/2}^{-1}$ configuration, which, as a non yrast state, is not observed in our experiment. The calculated $E(17/2^-) - E(19/2^-) = 158$ keV compares well with the measured 127(7) keV. This proves the reliability of the ESM calculations. The energy of the $19/2^-$ state is lowered by about 700 keV relative to the unperturbed energy. This is mainly due to the large attraction of proton and neutron in the $(\nu 2g_{9/2}\pi 1h_{9/2},\ 9^-)$ state as known in $^{210}$Bi. The $19/2^-$ state of the $\nu 2g_{9/2}\pi 1h_{9/2}3s_{1/2}^{-1}$ configuration in $^{209}$Pb has a very close analogon in the $19/2^+$ yrast state at 2987 keV in $^{209}$Bi [Mai83] with the configuration $\pi 1h_{9/2}\nu 2g_{9/2}3p_{1/2}^{-1}$. The difference between excitation energies $E(19/2^-(^{209}\mathrm{Pb})) - E(19/2^+(^{209}\mathrm{Bi})) = 537$ keV compares well to the difference between proton and neutron shell-gap energy (see Figure 1.2) $E_g(\pi) - E_g(\nu) + V_{\mathrm{Coul}} = 483$ keV; where $V_{\mathrm{Coul}} \simeq -300$ keV is the Coulomb pairing interaction.

*Level at 3810 keV,* $(21/2^-)$

We identify the exited state at 3810 keV with the $\nu 1i_{11/2}2g_{9/2}3p^{-1}_{1/2}$ configuration and its maximum angular momentum of $21/2^-$. The calculations firmly predict this state to be yrast at 3815 keV excitation energy. The downward energy shift, relative to the unperturbed state, is due to the attractive interaction of the $(\nu 2g_{9/2}3p^{-1}_{1/2},\ 5^-)$ excitation of the $^{208}$Pb core nucleus [Sch93, Rej95] and the $(\nu 2g_{9/2}1i_{11/2},\ 10^+)$ interaction as known from $^{210}$Pb [Rej97] (see also Figure 3.2 and Table 3.3). The $\nu 1i_{11/2}3p^{-1}_{1/2}$ interaction is assumed to not contribute significantly to the binding energy of this state; the second $6^-$ state of $\nu 1i_{11/2}3p^{-1}_{1/2}$ configuration in $^{208}$Pb nucleus is lowered only by 4 keV respectively to its unperturbed energy [Sch93, Rej95]. The M1 decay of the $21/2^-$ state to the $19/2^-$ state can proceed only via likely small admixtures of other configurations. The allowed E2 decay to the $17/2^-$ for the main configuration is slow[1] with the partial half life of $\sim 1$ ns. The E2 decay might also be enhanced by admixtures; particularly the probable admixture of $\nu 2g^2_{9/2}2f^{-1}_{5/2}$ to the $21/2^-$ would enlarge the probability of the transition to the $17/2^-$ state[2]. Therefore the comparable strength of the M1 and E2 transition as found in the experiment is acceptable.

*Level at 3842 keV,* $(21/2^+)$

The very strong 2419 keV transition depopulates a level at 3842 keV excitation energy. From the intensity we conclude that this is an yrast state. An Yrast state at this energy can only have the spin and parity $21/2^+$ and decay by an E3–transition. We interpret this state as $\nu 1j_{15/2} \times 3^-(^{208}\mathrm{Pb})$ with the stretched angular momentum coupling to $21/2^+$. The weak 318 keV $\gamma$–transition to the $(19/2^-)$ level fits into this picture. In $^{147}$Gd [Kle79] the state of analogous structure to the $21/2^+$ is depopulated by a strong E3 $\gamma$ ray (58%) competing with the corresponding E1 transition (42%). This level is further discussed in connection with particle–octupole vibration coupling in section 3.5.

*Level at 4329 keV,* $(23/2^+)$

The level at 4329 keV excitation energy can be confidently assigned to the $23/2^+$

[1] The E2 transition $(\nu 1i_{11/2}2g_{9/2}3p^{-1}_{1/2},\ 21/2^-) \rightarrow (\nu 2g^2_{9/2}3p^{-1}_{1/2},\ 17/2^-)$ is determined by the small reduced matrix element $\langle \nu 2g_{9/2}||E2||\nu 1i_{11/2}\rangle = -6.9$ e fm$^2$ [Don75].

[2] The electromagnetic E2 transition $(\nu 2g^2_{9/2}2f^{-1}_{5/2},\ 21/2^-) \rightarrow (\nu 2g^2_{9/2}3p^{-1}_{1/2},\ 17/2^-)$ is determined by a large $\left\langle \nu 3p^{-1}_{1/2}||E2||\nu 2f^{-1}_{5/2}\right\rangle = 20.6$ e fm$^2$ reduced matrix element [Don75].

state of the $\nu 1j_{15/2}2g_{9/2}3p^{-1}_{1/2}$ configuration. The $25/2^+$ spin assignment can be excluded as the $\nu 2g_{9/2} \times 3^-$ admixture of the $\nu 1j_{15/2}$ shell-model orbital is blocked by the Pauli principle and the $25/2^+$ state therefore shifted upwards considerably, similarly as the $12^-$ state of the $\nu 2g_{9/2}1j_{15/2}$ configuration in $^{210}$Pb [Rej97] (see also section 3.1). The calculations predict the $23/2^+$ state to be yrast at 4385 keV which is higher than the measured energy only by about 60 keV. The missing energy is very likely due to small admixtures of other configurations to this state; one possible admixture is $\nu 1j_{15/2}\pi 1h_{9/2}3s^{-1}_{1/2}$. The measured energy of the state is lowered by about 530 keV relative to its unperturbed energy. This results from the attraction in the $(\nu 2g_{9/2}3p^{-1}_{1/2},\ 5^-)$ and the $(\nu 1j_{15/2}3p^{-1}_{1/2},\ 8^+)$ yrast states in the $^{208}$Pb core nucleus [Sch93, Rej95] and the $(\nu 2g_{9/2}1j_{15/2},\ 11^-)$ yrast state in $^{210}$Pb [Rej97] (see also section 3.1). One may also compare directly the experimental spacings $E(23/2^+) - E(17/2^-) = 1237$ keV in $^{209}$Pb and $E(11^-) - E(8^+) = 1234$ keV in $^{210}$Pb. In both cases one neutron changes from $\nu 2g_{9/2}$ to $\nu 1j_{15/2}$. The very close agreement of these numbers may be understood as a consequence of the almost identical interaction of $\nu 3p^{-1}_{1/2}$ with $\nu 2g_{9/2}$ and $\nu 1j_{15/2}$. In fact the experimental spacings $E(8^+) - E(5^-) = 1413$ keV in $^{208}$Pb [Sch93] and $E(15/2^-) - E(9/2^+) = 1423$ keV in $^{209}$Pb are also almost the same. Nevertheless a $23/2^-$ assignment of the $\nu 1i_{11/2}2g_{9/2}2f^{-1}_{5/2}$ configuration to the 4329 keV level cannot be definitively ruled out, although in this case an M1–transition to the $(21/2^-)$ state should prevail.

Assignments to the states of higher excitation energy are ambiguous. Too many configurations are possible and configuration mixing, as observed in the $8^+$ and $10^+$ states in $^{208}$Pb [Sch93, Rej95], is expected to increase. Also reliable ESM calculations can no longer be performed as some important matrix elements like $\nu 2g_{9/2}\pi 1h^{-1}_{11/2}$ have not yet been measured.

## 3.3 The nucleus $^{207}$Tl

The nucleus $^{207}$Tl has 81 protons and 126 neutrons. In terms of the particle-core model it has one valence proton hole outside of the doubly magic $^{208}$Pb. It has been studied already by charged particle spectroscopy using the proton pick-up reactions $^{208}$Pb(d,$^3$He) [Gra92], $^{208}$Pb(t,$\alpha$) [Ecc65, Fly77] and the two neutron stripping reaction $^{205}$Tl(t, p) [Han69]. $\gamma$ transitions in $^{207}$Tl could be measured following the $\beta^-$ decay of $^{207}$Hg [Jon81] and from the decay of the $11/2^-$ isomer following the $^{208}$Pb(t,$\alpha$) reaction [Ecc65]. The above mentioned reactions populate predominantly the single hole states or selected one particle two hole states. The $1/2^+$

ground state and the yrast states $3/2^+$ and $11/2^-$ at energies 351 keV and 1348 keV could be established in earlier studies [Ecc65, Han69, Fly77, Gra92] and assigned as predominantly the proton hole occupying the $\pi 3s_{1/2}$, $\pi 2d_{3/2}$ and $\pi 1h_{11/2}$ shell-model orbitals respectively. The transition of energy 1348.1 keV depopulating the $11/2^-$ isomer directly to the ground state and the main decay cascade of 997.1 keV and 351.1 keV through the $3/2^+$ state have been found earlier [Ecc65, Jon81]. The isomeric half life of the $11/2^-$ state has been measured as $T_{1/2} = 1.3(1)$s [Ecc65]; it is mainly due to the M4 transition to the $3/2^+$ state.

In the present experiment we could observe the cascade of $\gamma$ rays of energies 351.1 keV and 997.1 keV in the off-beam $E_\gamma$-$E_\gamma$ coincidence spectra. The isomeric half life could not be measured as it exceeds the range of our sensitivity. We could identify in the in-beam prompt $E_\gamma$-$E_\gamma$ coincidence spectra from the experiment with the $^{208}$Pb beam a 2464.9 keV line in mutual coincidence with the 1609 keV transition from $^{209}$Bi [Mai83]. This coincidence relation could not be observed in the corresponding coincidence spectra of the experiment with the $^{136}$Xe beam, although the 2464.9 keV transition was very prominent in both experiments (see Figure 3.10 on page 50). Therefore, we assigned the 2464.9 keV transition to $^{207}$Tl which is the partner of $^{209}$Bi in the binary reaction of a $^{208}$Pb beam with a $^{208}$Pb target. No experimental evidence is available on $\gamma$-rays depopulating the yrast states in $^{137}$Cs, the partner of $^{207}$Tl in the binary reaction of the $^{136}$Xe beam with the $^{208}$Pb target. In the present experiment we did not observe any transitions which could be identified with this nucleus.

Several transitions could be observed in mutual prompt coincidence with the 2464.9 keV line in the experiments with both beams and based on this relation we assigned them also to $^{207}$Tl. In Figure 3.6 the spectra of prompt $\gamma$-rays coincident with the 2464.9 keV transition, assigned to $^{207}$Tl, from experiments using the $^{208}$Pb beam (a) and the $^{136}$Xe beam (b) are shown. In panel (a) the 1609 keV transition from $^{209}$Bi is evident. The energies and relative intensities, as observed in coincidence with the 2464.9 keV line, of $\gamma$ rays identified with $^{207}$Tl are given in Table 3.5. Based on the relative intensities and mutual coincidences we established the level scheme of $^{207}$Tl which is shown in Figure 3.7 (left column). The 2464.9 keV transition is the strongest of all observed and is proposed to feed the $11/2^-$ isomer in $^{207}$Tl. Only two additional $\gamma$ rays of energies 479.9 keV and 604.9 keV were placed in the level scheme as feeding the 3813 keV level. Nonobservation of the mutual coincidence relation between these transitions indicates their parallel placement in the level scheme. A $\gamma$ ray of energy 264.9 keV, which is about as intense as the 604.9 keV line is certainly located above the 4293 keV level. There is however also a weak coincidence with

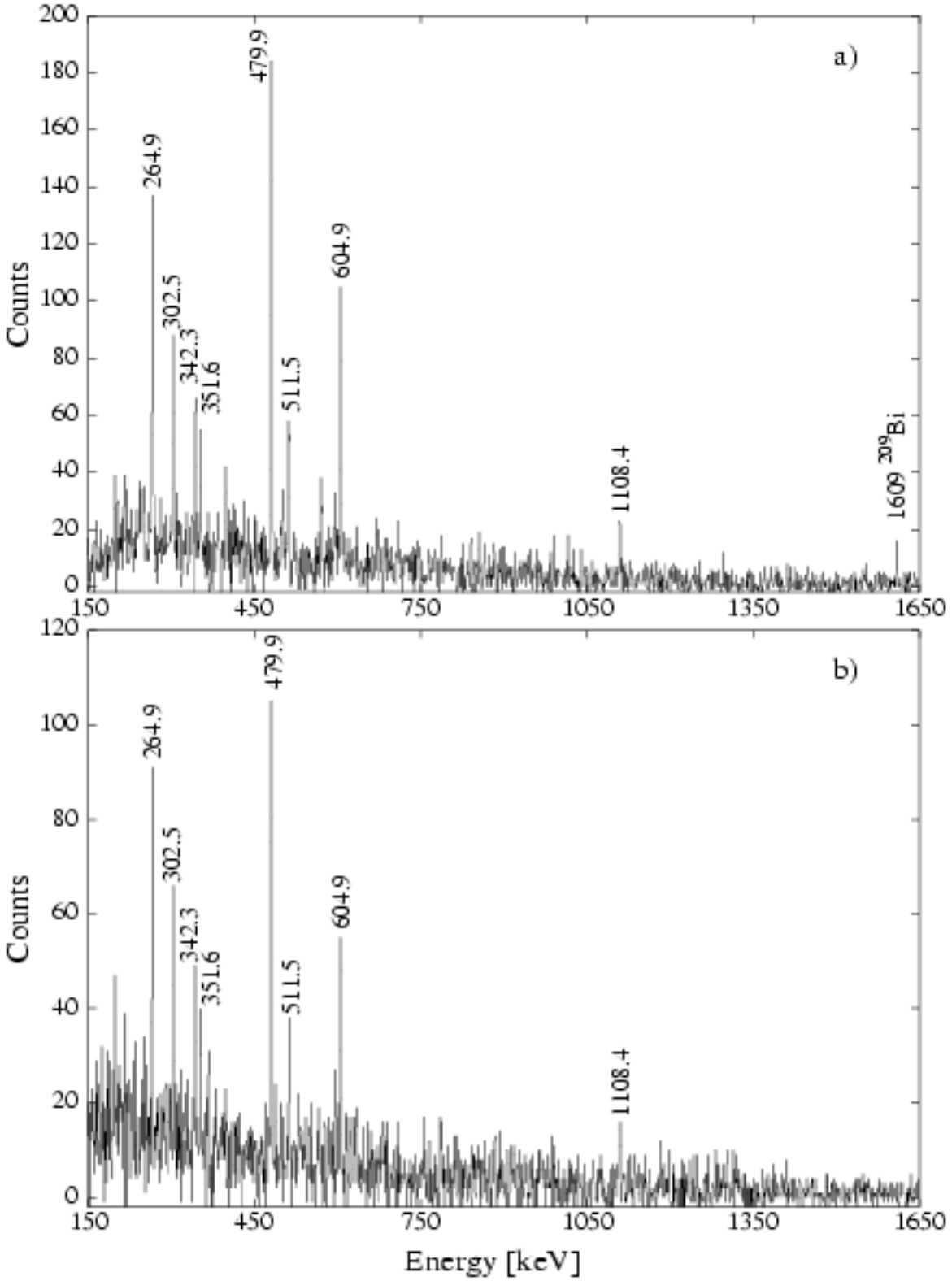


Figure 3.6 The spectrum of prompt $\gamma$-rays coincident to 2465 keV transition in $^{207}$Tl from the experiments with a) $^{208}$Pb beam, b) $^{136}$Xe beam.

Table 3.5 Energies and relative intensities of transitions assigned to $^{207}$Tl. Relative intensities as determined in coincidence with the 2464.9 keV transition from the experiment with the $^{208}$Pb beam are given. † - Doublet of lines.

| $E_\gamma$ [keV] | $I_\gamma$ | $E_i$ [keV] | $I_i^\pi$ |
|---|---|---|---|
| 264.9(1) | 58(7) | | |
| 302.5(5)† | 40(6) | | |
| 342.3(3) | 26(5) | | |
| 351.6(3) | 19(4) | | |
| 479.9(2) | 100(10) | 4293 | |
| 511.5(3) | 30(5) | | |
| 604.9(2) | 53(7) | 4418 | |
| 1108.4(3) | 19(5) | | |
| 2464.9(1) | – | 3813 | $(17/2^+)$ |

the 604.9 keV transition observed in the experiment. The other weak transitions, present in Table 3.5, could not be firmly placed due to the lack of intensity in the coincidence spectra.

The yrast states above $11/2^-$ involve excitations of the $^{208}$Pb core coupled to the single proton hole states in the $\pi 3s_{1/2}^{-1}$, $\pi 2d_{3/2}^{-1}$ and $\pi 1h_{11/2}^{-1}$ shell-model orbitals. The lowest excitation of $^{208}$Pb at 2615 keV is the collective $3^-$ state and this coupled to the $\pi 1h_{11/2}^{-1}$ proton hole is most likely to create an yrast state. The level observed at 3813 keV excitation energy is deexcited by the 2464.9 keV transition. From the intensity of this $\gamma$ line it follows that the level at 3813 keV is yrast. We interpret it as the $\pi 1h_{11/2}^{-1} \times 3^-(^{208}\mathrm{Pb})$ with stretched coupling to the maximum possible angular momentum of $17/2^+$. The state in $^{207}$Pb of corresponding structure to the $17/2^+$ level in $^{207}$Tl was reported earlier [Sch92]. The valence neutron hole in the $\nu 1i_{13/2}^{-1}$ shell-model orbital and the $3^-$ excitation of the $^{208}$Pb core create the excited state of spin-parity $19/2^-$, which is deexcited by the stretched E3 transition of energy 2485 keV to the $\nu 1i_{13/2}^{-1}$ level. A further discussion of particle octupole-vibration coupling can be found in Section 3.5.

Assignments of spin, parity and main configuration to the two new states at higher excitation energy are ambiguous. Their spin should however be at least 17/2. Many states are possible and reliable empirical shell-model calculations can not be

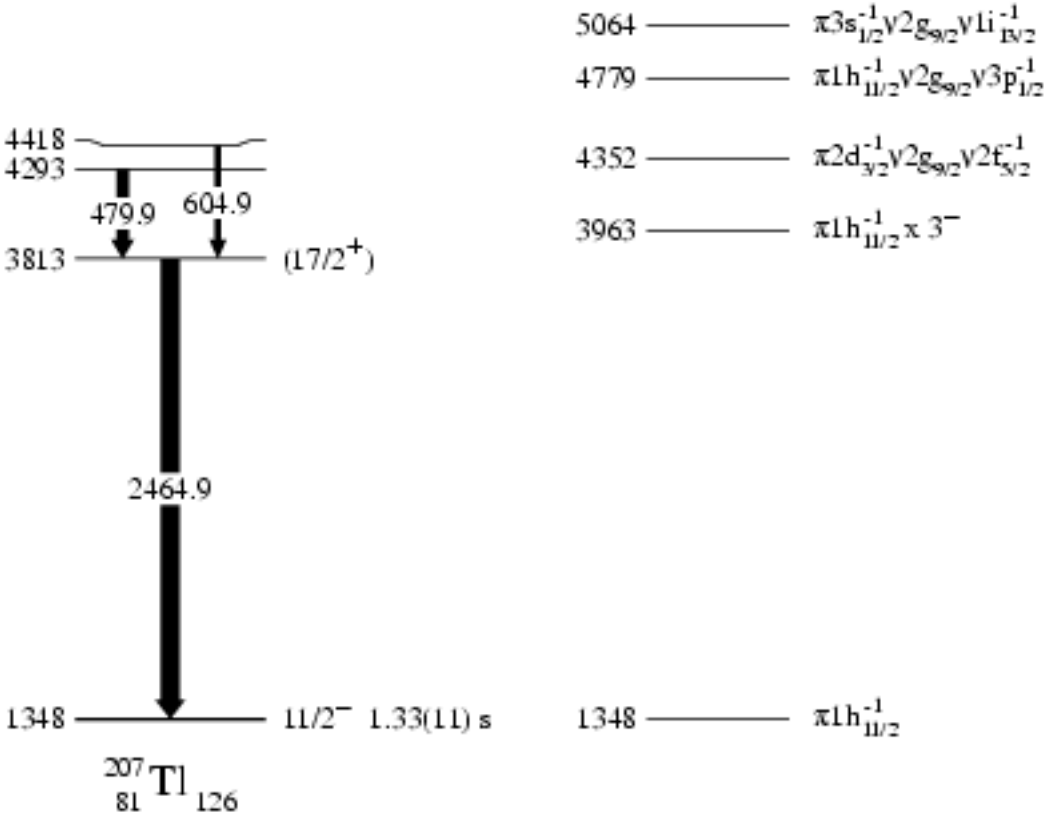


Figure 3.7 The partial level scheme of $^{207}$Tl, as observed in the experiment (left column). Only states above the $11/2^-$ isomer are presented. All energies are given in keV. The proposed spin-parity assignments, given in brackets, follow from systematics and model assumptions (see also text). Right column shows the unperturbed energies of the relevant configurations.

performed because matrix elements of the residual interaction are often missing. Of the one particle two hole configurations that can produce a spin of at least 17/2 the $\pi 2d^{-1}_{3/2}\nu 2g_{9/2}2f^{-1}_{5/2}$ (see Figure 3.7) has the lowest unperturbed energy. Its maximum spin is however only $17/2^-$. The next configuration $\pi 1h^{-1}_{11/2}\nu 2g_{9/2}3p^{-1}_{1/2}$ can create the yrast states of spin-parity $17/2^+$—$21/2^+$. The states observed at energies of 4293 keV and 4418 keV are possible candidates for $19/2^+$ and $21/2^+$ members of this multiplet. Other assignments cannot be excluded at present however.

## 3.4 The nucleus $^{206}$Tl

The nucleus $^{206}$Tl has one valence proton hole and one valence neutron hole outside the doubly magic $^{208}$Pb. It provides the unique possibility to study the strong proton-neutron hole two body residual interaction in the states with spin $I \leq 12$ where the two hole multiplets dominate the structure. The yrast states of higher spin have to involve particle hole excitations of the $^{208}$Pb core. This allows to study the particle-hole residual interaction for like and unlike particles additionally. The experimental information on these is very scarce at present.

Excitations in $^{206}$Tl have been studied already by a number of experiments. Proton-neutron hole multiplets at low spin could be investigated by charged particle spectroscopy with the one neutron stripping reaction $^{205}$Tl(d, p) [Ers65], one proton pick-up reaction $^{207}$Pb(t, $\alpha$) [Bar70] and the neutron-proton pick-up reaction $^{208}$Pb(d, $\alpha$) [Lew70]. The high spin yrast states were studied by $\gamma$ spectroscopy with the reactions $^{204}$Hg($\alpha$, pn$\gamma$) [Ber76], $^{204}$Hg($^{7}$Li, $\alpha$n$\gamma$) [Häu76] and by the neutron induced reaction $^{209}$Bi(n, $\alpha\gamma$) [Ura78]. A number of yrast states of spin $I \leq 12$ has been identified in previous studies [Ber76, Häu76, Ura78]. The excited state of spin-parity $12^-$ at 2463 keV is a spin-gap isomer of half life $T_{1/2} = 3.74(3)$ min. The $12^-$ state was found to be a member of the $\pi 1h^{-1}_{11/2}\nu 1i^{-1}_{13/2}$ multiplet; $12^-$ is the highest angular momentum to be reached without exciting the $^{208}$Pb core.

In the present experiment we could observe the population of the $12^-$ isomeric state, in the off-beam $E_\gamma$-$E_\gamma$ coincidence spectra, identifiable by the known $\gamma$ transitions from the previous studies [Ber76, Häu76, Ura78]. We could also identify the $\gamma$-rays depopulating the yrast states of the spin-parity $I \leq 8^+$, below the long lived isomer, in the analysis of the prompt-prompt $E_\gamma$-$E_\gamma$ coincidences. Apparently they are also populated bypassing the isomer or directly in quasielastic processes. We aimed to find new $\gamma$ transitions and the unknown high spin yrast states above the $12^-$ isomer in $^{206}$Tl. But an assignment by coincidences with known lines is in this case impossible. The half life of the $12^-$ isomer prohibits coincidences with transitions in $^{206}$Tl below it. The partner of $^{206}$Tl in the binary reaction of the $^{208}$Pb projectile with the $^{208}$Pb target is $^{210}$Bi. It has a very low lying yrast state of spin-parity $9^-$ which is the spin-gap isomer of half life $T_{1/2} = 3.06(6) \times 10^6$ y [Bro92] and no further yrast states above are known so far. In the experiment using the $^{136}$Xe projectiles the partner of $^{206}$Tl in the binary reaction is $^{138}$Cs. Also in this case the yrast states are known only up to a low lying long lived isomer of spin-parity $6^-$ with a half life $T_{1/2} = 2.91(8)$ m [Tul95]. Cross coincidences with $\gamma$ rays from the lighter partner nuclei ($^{209}$Bi, $^{137}$Cs) after evaporation of one or more neutrons are

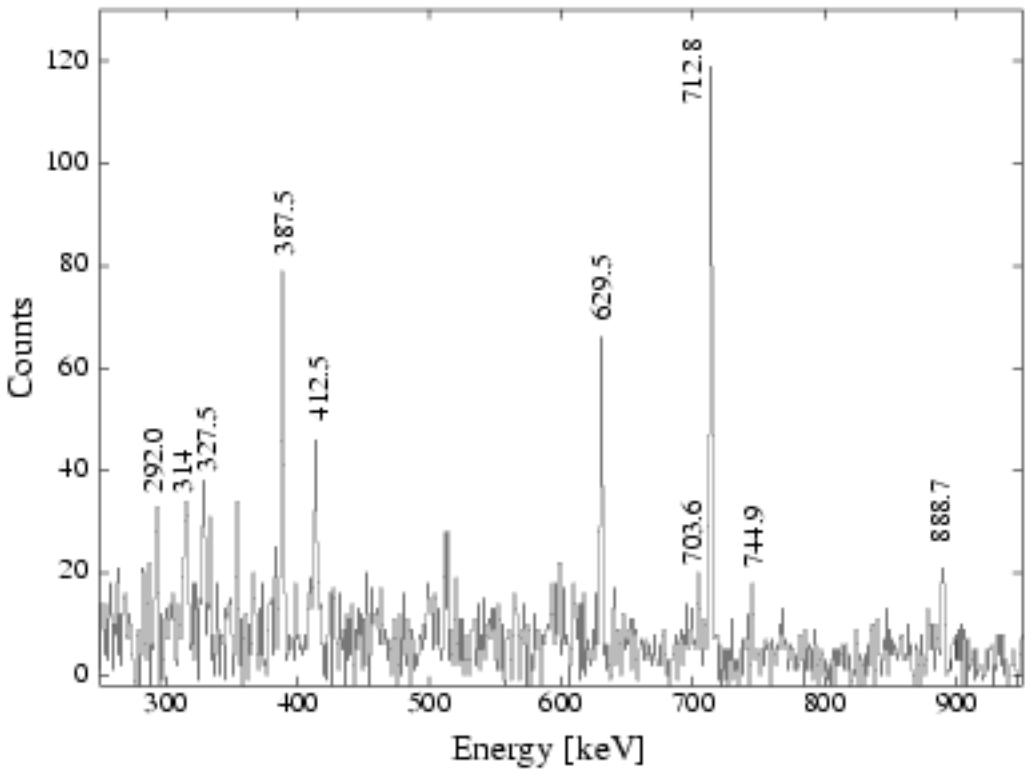


Figure 3.8 The spectrum of prompt $\gamma$-rays coincident with the 2333.2 keV transition in $^{206}$Tl from the experiment with the $^{208}$Pb beam.

likely too weak to be detected.

In the prompt-prompt $E_\gamma$-$E_\gamma$ coincidence spectra measured with both beams, a family of transitions in mutual coincidence with the strong 2333.2 keV $\gamma$ ray was found. The spectrum of $\gamma$ rays coincident with the 2333.2 keV transition from the experiment with the $^{208}$Pb beam is shown in Figure 3.8. We were not able to assign these lines to any nucleus from the prompt-prompt coincidences, because no known line is in coincidence. The high yield of the 2333.2 keV transition is comparable to that of the 2318 keV transition, (see Figure 3.10 on page 50) assigned previously [Bro96] as depopulating the high spin $17^+$ yrast state in $^{208}$Pb. From this we conclude that the 2333.2 keV $\gamma$ ray most probably depopulates an yrast state in a nucleus adjacent to $^{208}$Pb as high spin states in nuclei close to $^{208}$Pb are most strongly populated. An assignment to $^{210}$Bi could be excluded as in the experiment with the $^{208}$Pb beam the 2333.2 keV transition is not observed in cross coincidence with $\gamma$ rays depopulating the low spin yrast states in $^{206}$Tl.

The nucleus $^{206}$Tl, due to the model expectations, is the preferred choice of the

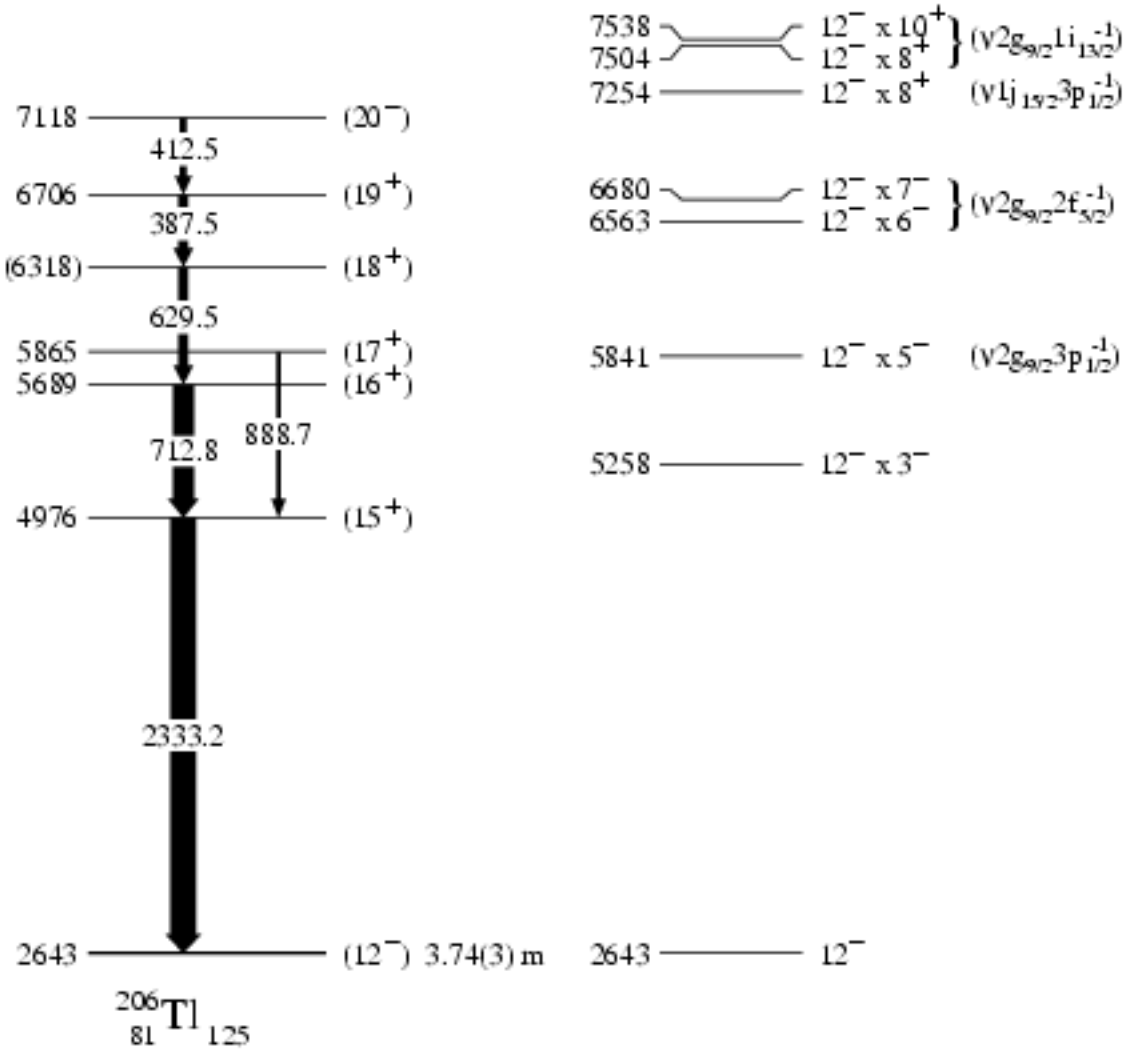


Figure 3.9 The partial level scheme of $^{206}$Tl as seen in the present experiment (left column). Only states above the $12^-$ isomer are presented. All energies are given in keV. The proposed spin-parity assignments, given in brackets, follow from systematics and model assumptions (see also text). The right column shows the energies of the relevant unperturbed states resulting from coupling of the $12^-$ state in $^{206}$Tl to the yrast excitations of the $^{208}$Pb core. The leading particle-hole configurations of the $^{208}$Pb core excitations are also presented.

nuclei to which the 2333.2 keV transition could be possibly assigned. However, the assignment to $^{208}$Tl and particularly to $^{208}$Bi can not be excluded based on the experimental data. Therefore, the following discussion, in particular the $\gamma$ transitions, is rather speculative.

Table 3.6 Energies and relative intensities in coincidence with the 2333.2 keV line from the experiment with the $^{208}$Pb beam of transitions identified with $^{206}$Tl. † - Doublet of lines.

| $E_\gamma$ [keV] | $I_\gamma$ | $E_i$ [keV] | $I_i^\pi$ |
|---|---|---|---|
| 292.0(2) | 15(4) | | |
| 314† | – | | |
| 327.5(2) | 17(4) | | |
| 387.5(2) | 45(7) | 6706 | $(19^+)$ |
| 412.5(1) | 34(6) | 7118 | $(20^-)$ |
| 629.5(2) | 45(8) | 6318 | $(18^+)$ |
| 703.6(2) | 13(4) | | |
| 712.8(1) | 100(13) | 5689 | $(16^+)$ |
| 744.9(2) | 8(3) | | |
| 888.7(2) | 21(5) | 5865 | $(17^+)$ |
| 2333.2(1) | – | 4976 | $(15^+)$ |

The next yrast state in $^{206}$Tl above the $(\pi 1h^{-1}_{11/2}\nu 1i^{-1}_{13/2},\ 12^-)$ level is most likely the $3^-$ vibration of the $^{208}$Pb core on top of this $12^-$ state, namely $((\pi 1h^{-1}_{11/2}\nu 1i^{-1}_{13/2},\ 12^-)\times 3^-;15+)$. The additivity relation of the particle octupole-vibration coupling model (see Section 3.5 for further details) predicts an energy difference very close to 2333 keV. Therefore we tentatively assign the 2333.2 keV transition and the $\gamma$ rays found to be in mutual coincidence with it, to the nucleus $^{206}$Tl; the 2333.2 keV transition as the strongest of all observed is proposed to feed the $12^-$ isomeric state at 2643 keV excitation energy.

The coincidence relations and the relative intensities of the $\gamma$ rays establish the level scheme of the yrast states of $^{206}$Tl as presented in the left column of Figure 3.9. The 629.5 keV and 387.5 keV transitions were found to be of equal intensity, within the experimental accuracy, and therefore their order in the level scheme is uncertain. Several other weak transitions could be assigned to $^{206}$Tl , due to the lack of coincidences however, they could not be firmly placed in the level scheme. The energies and relative intensities of $\gamma$ rays assigned to $^{206}$Tl, as measured in coincidence with the 2333.2 keV transition, are presented in Table 3.6.

The $12^-$ isomer has the highest spin, that is possible with one neutron hole and one proton hole. Levels of higher spin in $^{206}$Tl have to involve excitations of the

$^{208}$Pb core. One expects these to be the yrast states of $^{208}$Pb for the yrast states of $^{206}$Tl. The $(\pi 1h_{11/2}^{-1}\nu 1i_{13/2}^{-1},\ 12^-)$ level is the one neutron hole one proton hole state, that needs by far the least energy to generate angular momentum, because of the large attraction between the proton hole in the $1h_{11/2}$ orbital and the neutron hole in the $1i_{13/2}$ orbital coupled to maximum angular momentum of $12^-$. Therefore the states resulting from the coupling of the $12^-$ state with the yrast states of $^{208}$Pb form likely th yrast states in $^{206}$Tl. Their unperturbed energies are presented in the right column of Figure 3.9, and the further discussion will be performed with the help of this figure.

The excited state at 4976 keV is interpreted as the $(\pi 1h_{11/2}^{-1}\nu 1i_{13/2}^{-1} \times 3^-,\ 15^+)$ excitation. The 2333.2 keV transition is very likely an enhanced, stretched E3 related to $B(E3, 3^- \rightarrow 0^+) = 34.0(5)$W.u. [Spe89] in $^{208}$Pb.

The next excitation of $^{208}$Pb, above the collective $3^-$ state is $5^-$. It is predominantly of $\nu 2g_{9/2}3p_{1/2}^{-1}$ configuration [Sch93, Rej95], the particle-hole excitation with the lowest energy (see Figure 1.2 on page 6). The neutron in $2g_{9/2}$ orbital and the proton hole in the $1h_{11/2}$ orbital are expected to undergo a strong repulsive interaction if coupled to maximum angular momentum of $10^-$. This is not measured in this case, but a known common feature of all particle hole configurations, if hole and particle are different nucleons. The repulsion is significantly smaller if the spin is decreased by one unit. Therefore we propose the excited state at 5689 keV to be $(12^- \times (\nu 2g_{9/2}3p_{1/2},\ 5^-),\ 16^+)$. The $17^+$ state of the same configuration is, as discussed, expected at a slightly higher energy and it is likely the state at 5865 keV. Provided that these two levels have I $\geq 16$ no other configuration has an unperturbed energy close enough to be shifted by the residual interaction to the measured energy.

The next higher yrast states in $^{208}$Pb are $6^-$ and $7^-$ both predominantly of $\nu 2g_{9/2}2f_{5/2}^{-1}$ configuration; the neutron hole is moved from the $3p_{1/2}$ shell to the $2f_{5/2}$ shell of higher spin and higher excitation energy. Based on similar arguments as above one expects two states of spin-parity $18^+$ and $19^+$, both of $12^- \times \nu 2g_{9/2}2f_{5/2}^{-1}$ configuration, to become yrast at about 6.5 MeV in $^{206}$Tl. The energy spacing between these states is likely to be larger than in the case of $16^+$ and $17^+$ discussed earlier. The $6^-$ state is lower in excitation energy than the $7^-$ in $^{208}$Pb and the $18^+$ excitation of mixed parentage should be better bound than the $19^+$ of only $7^-$ parentage; on the other hand, the state of $(\nu 2g_{9/2}3p_{1/2},\ 4^-)$ configuration in $^{208}$Pb is higher by about 280 keV in excitation energy than the corresponding $5^-$ state. We propose the $18^+$ and $19^+$ assignment to the states at 6318 and 6706 keV. The $\gamma$ ray of energy 629.5 keV deexciting the $18^+$ state and feeding the $16^+$ state is in our interpretation a stretched E2 transition of one neutron hole from the $2f_{5/2}$ to

the $3p_{1/2}$ shell-model orbital. No transition has been observed connecting the $18^+$ and $17^+$ states. According to the main components of $18^+$ and $17^+$ states, an M1 transition is configuration forbidden and the allowed E2 transition cannot compete as it would be five times slower than the 629.5 keV line from the energy factor. The $19^+$ state is deexcited by the 387.5 keV $\gamma$ ray. It is likely an M1 transition that proceeds by the diagonal transition matrix element between the states of the same one particle-three hole multiplet.

The next possible excitations of the $^{208}$Pb core are $\nu 1j_{15/2}3p^{-1}_{1/2}$ and $\nu 2g_{9/2}1i^{-1}_{13/2}$ (see the right column of Figure 3.9). The former one is not likely to contribute to the yrast state in $^{205}$Tl as the large repulsion of the proton hole in the $1h_{11/2}$ orbital and the neutron in the $1j_{15/2}$ orbital at high angular momentum would push the state of this configuration upwards significantly. The $\pi 1h^{-1}_{11/2}\nu 1i^{-2}_{13/2}2g_{9/2}$ configuration is favoured due to the attraction of both $1i_{13/2}$ neutron holes with the $1h_{11/2}$ proton hole that can be gained. Therefore the highest state observed in the experiment we interpret as the $20^-$ of mainly this configuration. The $\gamma$ ray of energy 412.5 keV is then of E1 character. The E1 transition between the main components of $20^-$ and $19^+$ states is forbidden and therefore it proceeds by small admixture of other configurations. The corresponding E1 transition has been observed in $^{208}$Pb [Sch97] that proceeds from the second $8^+$ state to the $7^-$ state.

## 3.5 Particle Octupole-Vibration Coupling

The low lying states of the nuclei in the vicinity of $^{208}$Pb result from the excitation of very few particles or holes due to the double shell closure of the $^{208}$Pb core. The presence of the low lying collective octupole vibration of the core nucleus is also very important for the structure of the lowest excited states. The excitation energy of the first $3^-$ state in $^{208}$Pb is 2615 keV; this is about 800 keV lower than the neutron shell gap energy (see Figure 1.2 on page 6). It is interpreted to be a surface vibration of octupole character. The high collectivity of this one-phonon excitation was confirmed by the observation of the strongly enhanced E3 transition to the $0^+$ ground state in $^{208}$Pb. Its reduced transition probability was measured, $B(E3, 3^- \rightarrow 0^+) = 34.0(5)$W.u. [Spe89], 34 times the single particle estimate. Many levels in the nuclei close to $^{208}$Pb combine this collective octupole excitation with the excitation of single particles. There is a coupling between the single particle structure and the octupole vibration, that is essential for the properties of these states. This has been theoretically treated in detail [Ham69, Ham70]. In the following we present first the new experimental findings on this subject, that are particularly well suited to

study the particle octupole-vibration coupling. Then the theory is presented and compared with experiment.

The part of the measured $E_\gamma$-$E_\gamma$ projection around 2615 keV, the energy of the $3^-$ octupole vibrational state in $^{208}$Pb, is shown in Figure 3.10 on page 50. Many strong $\gamma$ transitions are evident in both spectra from the experiments with the $^{208}$Pb and $^{136}$Xe beams. Most of these $\gamma$ lines could be identified as it is indicated in Figure 3.10; the information on these transitions is summarized in Table 3.7 on page 51. All these transitions are interpreted as deexciting an octupole vibration built on the states of highest spin formed by one or two particles (holes). The new states are assumed to result from stretched angular momentum coupling, i. e. their spin is that of the single particle state + $3\hbar$. While again the experiment does not determine spins, these outstanding lines are almost certainly yrast transitions. Also the states of lower spin of the octupole multiplets could decay by faster transitions of lower multipolarity.

It has been found earlier that the 2741 keV transition in $^{209}$Bi depopulates the $3^-$ excitation on top of the $\pi 1h_{9/2}$ proton state [Mai83]. The proton spin and the octupole vibration are coupled to the maximum possible angular momentum of $15/2^+$ and the stretched 2741 keV E3 transition that depopulates this state feeds the $\pi 1h_{9/2}$ ground state of $^{209}$Bi. It has been proposed before [Sch92], that the 2485 keV line depopulates a state at 4119 keV of the $(\nu 1i^{-1}_{13/2} \times 3^-,\ 19/2^-)$ configuration in $^{207}$Pb. Later experiments assigned this line definitely to $^{207}$Pb and on top of the $13/2^+$ isomer [Bro96]. In the present experiment the 2419 keV line could be placed in $^{209}$Pb [Rej98] (see also Section 3.2). It deexcites the $21/2^+$ state; the octupole vibration built on the $\nu 1j_{15/2}$ neutron state. The state of corresponding structure could now be also established in $^{207}$Tl (see Section 3.3). The state of the $(\pi 1h^{-1}_{11/2} \times 3^-,\ 17/2^+)$ configuration is deexcited by a $\gamma$ ray of energy 2465 keV. These transitions are now known in all four one particle or one hole nuclei.

In $^{208}$Pb, a similar experiment [Bro96] revealed a 2318 keV line that depopulates the state of the structure $(\nu 1j_{15/2}1i^{-1}_{13/2}\times 3^-,\ 17^+)$; the parent state $(\nu 1j_{15/2}1i^{-1}_{13/2},\ 14^-)$ has the maximum spin that can be gained by a one particle one hole excitation in $^{208}$Pb. The 2403 keV E3 transition has been reported earlier [Blo93] to depopulate the $(\nu 1i^{-2}_{13/2} \times 3^-,\ 15^-)$ state in $^{206}$Pb. Also here the $(\nu 1i^{-2}_{13/2},\ 12^+)$ level has the highest possible spin for two neutron-holes. In the present experiment we could observe in addition the 2559 keV transition that deexcites the octupole vibration on the $(\nu 1i^{-1}_{13/2}2f^{-1}_{5/2},\ 9^-)$ state in $^{206}$Pb [Blo93]. The 2333 keV line has been assigned to the nucleus $^{206}$Tl (see Section3.4). It deexcites the $15^+$ state of $\pi 1h^{-1}_{11/2}\nu 1i^{-1}_{13/2} \times 3^-$ configuration.

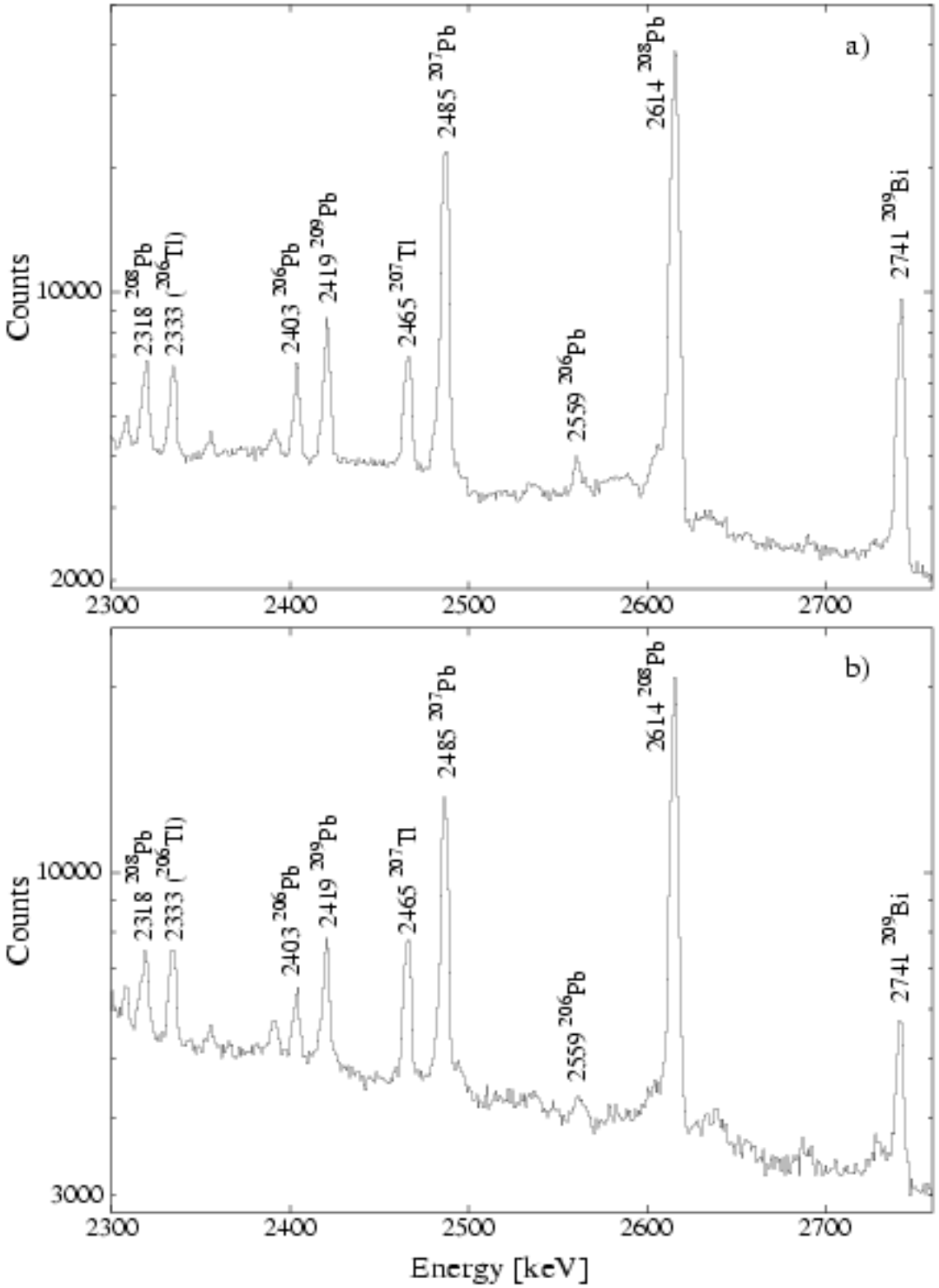


Figure 3.10 The high energy part of the total projection of the prompt-prompt $E_\gamma$-$E_\gamma$ coincidence matrix from the experiment with a) $^{208}$Pb beam, b) $^{136}$Xe beam.

Table 3.7 High energy transitions observed in nuclei around $^{208}$Pb. These transitions are interpreted as E3–transitions depopulating octupole excitations on top of high spin few particle states as presented.

| Nucleus | $E_\gamma$ [keV] | $E_i$ [keV] | $I_i^\pi$ [$\hbar$] | configuration | $E_f$ [keV] | $I_f^\pi$ [$\hbar$] | configuration |
|---|---|---|---|---|---|---|---|
| $^{206}$Tl | 2333 | 4976 | $(15^+)$ | $\pi 1h_{11/2}^{-1}\nu 1i_{13/2}^{-1}\times 3^-$ | 2643 | $(12^-)$ | $\pi 1h_{11/2}^{-1}\nu 1i_{13/2}^{-1}$ |
| $^{207}$Tl | 2465 | 3813 | $(17/2^+)$ | $\pi 1h_{11/2}^{-1}\times 3^-$ | 1348 | $11/2^-$ | $\nu 1h_{11/2}^{-1}$ |
| $^{206}$Pb | 2559 | 5218 | $12^+$ | $\nu 1i_{13/2}^{-1}2f_{5/2}^{-1}\times 3^-$ | 2658 | $9^-$ | $\nu 1i_{13/2}^{-1}2f_{5/2}^{-1}$ |
| $^{206}$Pb | 2403 | 6430 | $15^-$ | $\nu 1i_{13/2}^{-2}\times 3^-$ | 4027 | $12^+$ | $\nu 1i_{13/2}^{-2}$ |
| $^{207}$Pb | 2485 | 4118 | $(19/2^-)$ | $\nu 1i_{13/2}^{-1}\times 3^-$ | 1633 | $13/2^+$ | $\nu 1i_{13/2}^{-1}$ |
| $^{208}$Pb | 2318 | 9062 | $(17^+)$ | $\nu 1j_{15/2}1i_{13/2}^{-1}\times 3^-$ | 6744 | $14^-$ | $\nu 1j_{15/2}1i_{13/2}^{-1}$ |
| $^{209}$Pb | 2419 | 3842 | $(21/2^+)$ | $\nu 1j_{15/2}\times 3^-$ | 1423 | $15/2^-$ | $\nu 1j_{15/2}$ |
| $^{209}$Bi | 2741 | 2741 | $15/2^+$ | $\pi 1h_{9/2}^{-1}\times 3^-$ | 0 | $9/2^-$ | $\pi 1h_{9/2}$ |

Table 3.7 shows that the energy of the octupole vibration on top of the few particle states differs from its unperturbed energy in $^{208}$Pb. This is due to the variation of the nuclear density and thus of the average nuclear potential associated with the collective vibration. This vibrating potential influences the motion of the particles. It provides a coupling between the vibrational degrees of freedom and those of the individual particles, and produces a scattering of the particles between states with emission and absorption of a quantum. In the following the theory for the coupling between the single particle motion and the octupole vibration is presented and then compared with the experimental data.

The matrix element of the coupling, for the scattering of the particle between states $j_1$ and $j_2$, as depicted in Figure 3.11, with the excitation of a phonon of angular momentum $\lambda$ can be written as [Bohr75, (p. 418)]

$$h(j_1,j_2\lambda) = -i^{l_1+\lambda-l_2}\cdot\sqrt{\frac{2\lambda+1}{4\pi}}\cdot\left\langle j_1\frac{1}{2}\lambda 0\left|j_2\frac{1}{2}\right.\right\rangle\cdot\sqrt{\frac{\hbar\omega_\lambda}{2C_\lambda}}\cdot\left\langle j_2\left|R_0\cdot\frac{\partial V(r)}{\partial r}\right|j_1\right\rangle \quad (3.2)$$

The labels $j_1$ and $j_2$ refer to the $n$, $l$ and $j$ quantum numbers describing the state of a given particle. The energy of the vibrational phonon of angular momentum $\lambda$ is $\hbar\omega_\lambda$ and $C_\lambda$ is referred to as the restoring force parameter. It is assumed that

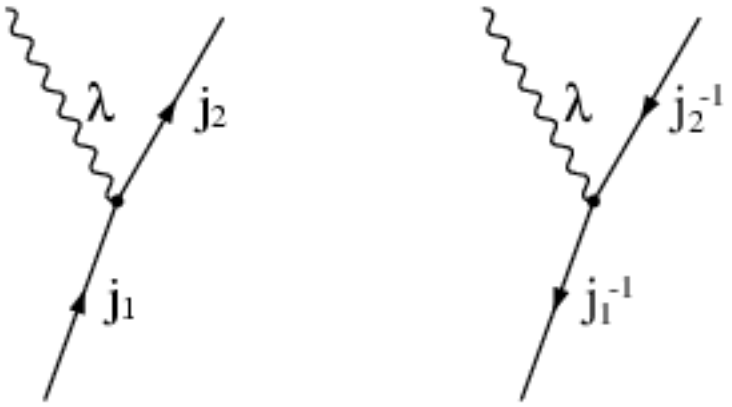


Figure 3.11 Diagrams illustrating the first-order coupling matrix elements between the single a) particle, b) hole states and the vibrational phonon.

the density variation due to the shape oscillation can be approximately obtained by a deformation of the average static central potential $V(r)$. The last term of Equation 3.2, the radial coupling matrix element[1], is the radial overlap of the particles and the oscillating potential at the surface of the nucleus. The $\alpha_{0\lambda} = \sqrt{\hbar\omega_\lambda / 2C_\lambda}$ is the zero point amplitude of the vibration.

The coupling matrix element given in Equation 3.2 requires the parity selection rule of $l_1 + \lambda - l_2 =$ even and the spin selection rule of $|j_2 - \lambda| \leq j_1 \leq j_2 + \lambda$. It obeys the symmetry relation

$$h(j_1, j_2\lambda) = (-1)^{j_1+\lambda-j_2} \cdot \sqrt{\frac{2j_2+1}{2j_1+1}} \cdot h(j_2, j_1\lambda) \tag{3.3}$$

We performed a numerical calculation of the coupling matrix elements between the octupole vibration $\lambda = 3$ of the $^{208}$Pb core and the single particle states in the one particle(hole) nuclei around $^{208}$Pb. In the calculations we used the central potential $V(r)$ as

$$V(r) = V_{\text{Coulomb}} + V_0 \cdot \frac{1}{1 + \exp\left(\frac{r-R_0}{a}\right)} \tag{3.4}$$

[1] The radial matrix element is defined as

$$\langle n_2 l_2 j_2 | f(r) | n_1 l_1 j_1 \rangle = \int_0^\infty \mathcal{R}_{n_2 l_2 j_2} f(r) \mathcal{R}_{n_1 l_1 j_1} r^2 dr$$

Table 3.8 Coupling matrix elements between the indicated single particle (hole) states and the octupole vibration. The calculated radial and total matrix elements according to Equation 3.2 are compared to those deduced from experiment as explained in the text.

| $j_1$ | $j_2$ | $\left\langle j_2 \left\vert R_0 \cdot \frac{\partial V(r)}{\partial r} \right\vert j_1 \right\rangle$ [MeV] | $h(j_1, j_2 \times 3^-)$ [MeV] | $h_{\exp}(j_1, j_2 \times 3^-)$ [MeV] |
|---|---|---|---|---|
| $\nu 1j_{15/2}$ | $\nu 2g_{9/2}$ | 51.045 | −0.848 | −0.591 |
| $\nu 1j_{15/2}$ | $\nu 1i_{11/2}$ | 68.159 | −0.213 | |
| $\nu 1i^{-1}_{13/2}$ | $\nu 2f^{-1}_{7/2}$ | 51.184 | +0.830 | +0.725 |
| $\nu 1i^{-1}_{13/2}$ | $\nu 1h^{-1}_{9/2}$ | 59.251 | +0.214 | |
| $\pi 1h^{-1}_{11/2}$ | $\pi 2d^{-1}_{5/2}$ | 48.006 | +0.750 | +0.747 |
| $\pi 1h^{-1}_{11/2}$ | $\pi 2g^{-1}_{7/2}$ | 47.782 | +0.207 | |

with the potential depth $V_0 = -60.7$ MeV, diffuseness $a = 0.81$ fm, mean radius of the nucleus $R_0 = 1.27 \cdot A^{1/3}$ fm for protons and $V_0 = -45.8$ MeV, $a = 0.72$ fm and $R_0 = 1.24 \cdot A^{1/3}$ fm for neutrons [Str82]. The unperturbed energy of the vibrational phonon $\hbar\omega_3 = 2615$ keV, as observed in $^{208}$Pb, and the zero point amplitude $\alpha_{03} = 0.045$, as determined from the reduced E3 transition probability [Ham69], have been used in the numerical calculations. The radial wave functions of the particles were chosen to be positive at the surface of the nucleus. The calculated matrix elements are presented in Table 3.8. The corresponding radial coupling matrix elements are also shown. An approximate selection rule can be given for the coupling matrix element (Equation 3.2) if $j_1$ and $j_2$ are larger, or comparable with $\lambda$. The vector addition coefficient $\left\langle j_1 \frac{1}{2} \lambda 0 \middle| j_2 \frac{1}{2} \right\rangle$ strongly inhibits the transitions involving a spin flip ($j_1 = l_1 \pm 1/2 \rightarrow j_2 = l_2 \mp 1/2$), as compared with transitions ($j_1 = l_1 \pm 1/2 \rightarrow j_2 = l_2 \pm 1/2$), that preserve the relative orientation of spin and orbit. This is evident in Table 3.8. On the other hand the radial matrix elements do not change much.

The present experiment found some of the states in $^{207}$Tl, $^{207}$Pb and $^{209}$Pb that can be described by particles (holes) in the orbitals $j_1$ and $j_2$ with admixtures of $(j_2 \times 3^-)$ and $(j_1 \times 3^-)$ respectively. For both spins $j_1$ and $j_2$ we have a two level system and the Hamiltonian for these systems can be written down right away. This is done below for $^{209}$Pb. The unperturbed single particle energies are $\epsilon_1$ and $\epsilon_2$, the particles are $\nu 2g_{9/2}$ and $\nu 1j_{15/2}$ for $^{209}$Pb, the energy of the octupole phonon is $\hbar\omega_3$ = 2615 keV and $h \equiv h(\nu 1j_{15/2}, \nu 2g_{9/2} \times 3^-)$ is the coupling matrix element.

The Hamiltonian matrices describing the $9/2^+$, $15/2^-$ and $21/2^+$ states respectively are:

$$\begin{cases} H(9/2^+) &= \begin{bmatrix} \epsilon_1 & \sqrt{\frac{16}{10}}h \\ \sqrt{\frac{16}{10}}h & \epsilon_2 + \hbar\omega_3 \end{bmatrix} \\ H(15/2^-) &= \begin{bmatrix} \epsilon_2 & h \\ h & \epsilon_1 + \hbar\omega_3 \end{bmatrix} \\ H(21/2^+) &= \begin{bmatrix} \epsilon_2 + \hbar\omega_3 & \sqrt{2}h \\ \sqrt{2}h & \epsilon_1 + 2\hbar\omega_3 \end{bmatrix} \end{cases}$$

where we used the symmetry relation (Equation 3.3), and the "boson factor" of $\sqrt{2}$ in the last Hamiltonian comes from the symmetrized intermediate state with two identical phonons.

The diagonalization leads to the set of equations describing the energy of the lower state of each doublet (for the higher state the sign of the square root is +).

$$\begin{cases} \frac{1}{2}\left\{\epsilon_1 + \epsilon_2 + \hbar\omega_3 - \sqrt{(\epsilon_1 - \epsilon_2 - \hbar\omega_3)^2 + 4\frac{16}{10}h^2}\right\} &= E(9/2^+) &= 0.000 \text{ MeV} \\ \frac{1}{2}\left\{\epsilon_1 + \epsilon_2 + \hbar\omega_3 - \sqrt{(\epsilon_2 - \epsilon_1 - \hbar\omega_3)^2 + 4h^2}\right\} &= E(15/2^-) &= 1.423 \text{ MeV} \\ \frac{1}{2}\left\{\epsilon_1 + \epsilon_2 + 3\hbar\omega_3 - \sqrt{(\epsilon_2 - \epsilon_1 - \hbar\omega_3)^2 + 8h^2}\right\} &= E(21/2^+) &= 3.842 \text{ MeV} \end{cases}$$

where the right-hand side of each equation is the experimental excitation energy. The theory contains only two parameters, the difference of the single particle energies $\epsilon_1 - \epsilon_2$ and the coupling element $h$. We determine these parameters from these measured level energies as:

$$\epsilon_1 = 0.130 \text{ MeV}, \ \epsilon_2 = 1.687 \text{ MeV}$$
$$h(\nu 1j_{15/2}, \nu 2g_{9/2} \times 3^-) = -0.591 \text{ MeV}$$

In the following we explore how well the model with these parameters fits also other experimental data. Figure 3.12 on page 55 shows the partial level scheme of $^{209}$Pb resulting from the particle octupole-vibration calculations as described above. The model energy of the second excited $15/2^-$ state, 3009 keV, is in very good agreement with the experimental energy, 3047 keV (see Table 3.4), although it has not been used in determining the parameters. The energies of the relevant unperturbed states, as calculated here, are presented on the right hand side of Figure 3.12.

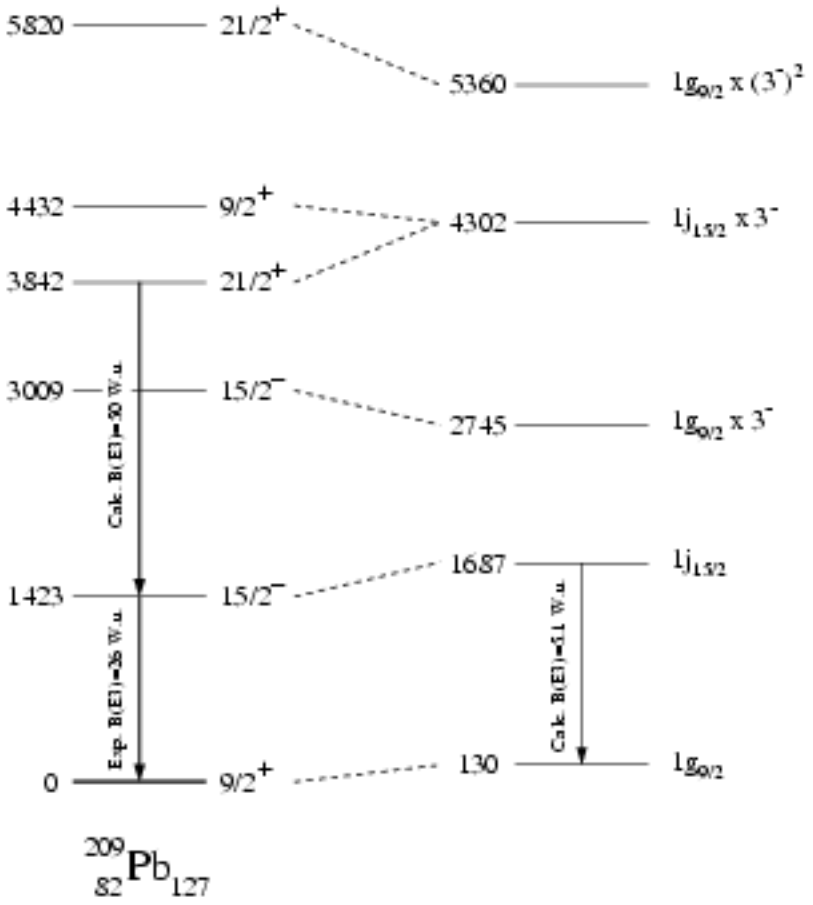


Figure 3.12 The partial level scheme of $^{209}$Pb nucleus resulting from the particle octupole-vibration coupling calculation (left). The energies of the uncoupled states are presented for comparison on the right. All energies are given in keV relative to the ground state of $^{209}$Pb. See text for further information.

$$
\begin{array}{ccccccc}
|21/2^+\rangle & = & 0.876 \cdot \left|\nu 1j_{15/2} \times 3^-\right\rangle & + & 0.482 \cdot \left|\nu 2g_{9/2} \times (3^-)^2\right\rangle & & \\
\downarrow 50\ \text{W.u.} & & \downarrow 34\ \text{W.u.} & \searrow 5.1\ \text{W.u.} & & & \downarrow 2 \times 34\ \text{W.u.} \\
|15/2^-\rangle & = & 0.913 \cdot \left|\nu 1j_{15/2} \times 0^+\right\rangle & + & 0.408 \cdot \left|\nu 2g_{9/2} \times 3^-\right\rangle & & \\
\downarrow 26\ \text{W.u.} & & \downarrow 5.1\ \text{W.u.} & \searrow \tfrac{10}{16} 34\ \text{W.u.} & & \swarrow 34\ \text{W.u.} & \downarrow \tfrac{10}{(2020)^2} 5.1\ \text{W.u.} \\
|9/2^+\rangle & = & 0.985 \cdot \left|\nu 2g_{9/2} \times 0^+\right\rangle & + & 0.171 \cdot \left|\nu 1j_{15/2} \times 3^-\right\rangle & &
\end{array}
$$

Figure 3.13 Transition probabilities deduced for the stretched E3 transitions between the lowest $21/2^+$, $15/2^-$ and $9/2^+$ states.

Table 3.9 Energies and wave functions of the excited states of $^{209}$Pb, $^{207}$Pb and $^{207}$Tl from the particle octupole-vibration calculations. The energies that have been used to determine the parameters are marked by an asterisk.

| $^{209}$Pb | | | |
|---|---|---|---|
| $E_{\mathrm{CAL}}$ [MeV] | $I^\pi$ [$\hbar$] | amplitude of wave function | |
| | | $\nu 2g_{9/2}$ | $\nu 1j_{15/2} \times 3^-$ |
| 0.000* | $9/2^+$ | +0.985 | +0.171 |
| 4.432 | $9/2^+$ | −0.171 | +0.985 |
| | | $\nu 1j_{15/2}$ | $\nu 2g_{9/2} \times 3^-$ |
| 1.423* | $15/2^-$ | +0.913 | +0.408 |
| 3.009 | $15/2^-$ | −0.408 | +0.913 |
| | | $\nu 1j_{15/2} \times 3^-$ | $\nu 2g_{9/2} \times (3^-)^2$ |
| 3.842* | $21/2^+$ | +0.876 | +0.482 |
| 5.820 | $21/2^+$ | −0.482 | +0.876 |
| $^{207}$Pb | | | |
| | | $\nu 2f^{-1}_{7/2}$ | $\nu 1i^{-1}_{13/2} \times 3^-$ |
| 2.340* | $7/2^-$ | +0.906 | −0.424 |
| 4.836 | $7/2^-$ | +0.424 | +0.906 |
| | | $\nu 1i^{-1}_{13/2}$ | $\nu 2f^{-1}_{7/2} \times 3^-$ |
| 1.633* | $13/2^+$ | +0.982 | −0.189 |
| 5.543 | $13/2^+$ | +0.189 | +0.982 |
| | | $\nu 1i^{-1}_{13/2} \times 3^-$ | $\nu 2f^{-1}_{7/2} \times (3^-)^2$ |
| 4.118* | $19/2^-$ | +0.967 | −0.254 |
| 8.288 | $19/2^-$ | +0.254 | +0.967 |
| $^{207}$Tl | | | |
| | | $\pi 2d^{-1}_{5/2}$ | $\pi 1h^{-1}_{11/2} \times 3^-$ |
| 1.683* | $5/2^+$ | +0.918 | −0.397 |
| 4.584 | $5/2^+$ | +0.397 | +0.918 |
| | | $\pi 1h^{-1}_{11/2}$ | $\pi 2d^{-1}_{5/2} \times 3^-$ |
| 1.348* | $11/2^-$ | +0.977 | −0.214 |
| 4.919 | $11/2^-$ | +0.214 | +0.977 |
| | | $\pi 1h^{-1}_{11/2} \times 3^-$ | $\pi 2d^{-1}_{5/2} \times (3^-)^2$ |
| 3.813* | $17/2^+$ | +0.959 | −0.285 |
| 7.684 | $17/2^+$ | +0.285 | +0.959 |

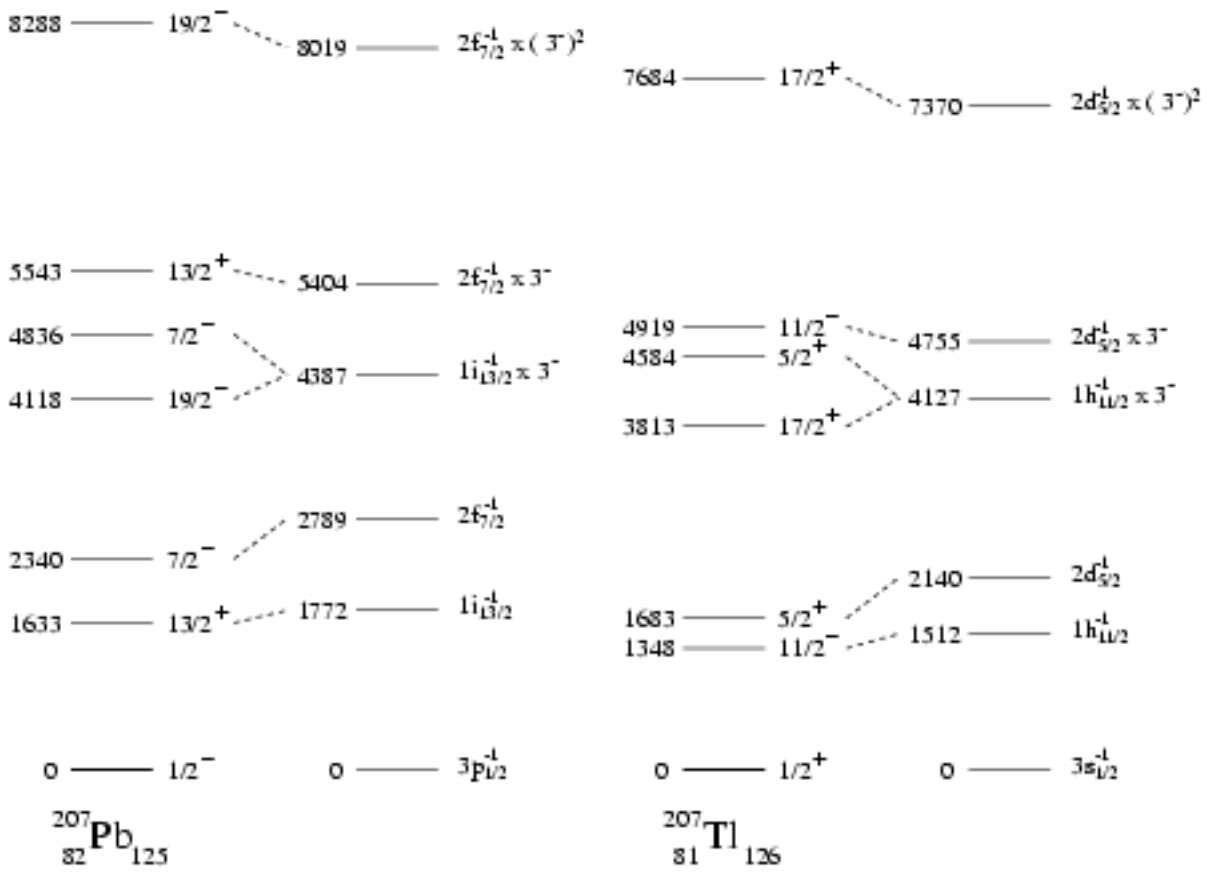


Figure 3.14 The partial level schemes of $^{207}$Pb and $^{207}$Tl resulting from the particle octupole-vibration coupling calculations (left) are compared with the energies of uncoupled states (right). All energies are given in keV.

Sizeable shifts are observed of the energies of the predominant single particle states $\nu 2g_{9/2}$ and $\nu 1j_{15/2}$, that are caused by the coupling of the particles to the low frequency $3^-$ vibration.

Table 3.9 on page 56. gives the calculated wave functions of the relevant states. It is seen that the admixture of the $\nu 1j_{15/2} \times 3^-$ configuration to the ground state is small $\simeq 3\%$. This is due to the large, energy separation of about 4.2 MeV between the levels that mix. The admixture of the $\nu 2g_{9/2} \times 3^-$ in the $15/2^-$ state however is about 17% as the energy separation of the pure states is about 1.0 MeV. The double octupole admixture of $\nu 2g_{9/2} \times (3^-)^2$ in the $21/2^+$ state is about 23%.

The mixing between the $15/2^-$ states can be directly compared with the spectroscopic factors measured in the $^{208}$Pb(d, p) reaction. Kovar, Stein and Bock-

elman [Kov74] give the following spectroscopic factors for $l = 7$ transfer: $S = 0.77,\ 0.090,\ 0.042,\ 0.042$ for levels at 1.424, 3.052, 3.556 and 3.716 MeV. The corresponding squared amplitudes from the model are 0.83 and 0.17 for the two lowest states. The absolute normalisation of the measured spectroscopic factors is subject to some uncertainty. Therefore the agreement for the 1423 keV state might be somewhat fortuitous. A comparison of the strengths for the 3047 keV level is however meaningful, and the agreement within a factor 2 is satisfactory. Our model, that only considers particle octupole-vibration coupling, is of course a simplification. There are other $15/2^-$ states that can also mix, like $\nu 2g_{9/2} \times 5^-(^{208}\mathrm{Pb})$ or $\nu 1i_{11/2} \times 3^-$. If this mixing should be mainly between the three higher levels, then the sum of the 3 spectroscopic factors should be compared with the model, and the agreement is perfect.

The measured $B(E3, 15/2^- \rightarrow 9/2^+) = 26(4)$ W.u. [Ell67] in $^{209}$Pb can also be compared with the model. The contributions to the E3 transition are shown in Figure 3.13 on page 55. The total B(E3) value is the coherent sum over the individual contributions. However the $B(E3, \nu 1j_{15/2} \rightarrow \nu 2g_{9/2})$ value for the pure single particles is not known. Therefore we reverse the procedure and calculate it from the measured value and the model wave function as:

$$B(E3, \nu 1j_{15/2} \rightarrow \nu 2g_{9/2}) = 5.1 \text{ W.u.} = 13234.5 \text{ e}^2 \text{ fm}^6$$

On the other hand the theoretical transition probability[2] is [Bohr69, (p. 387)]

$$B_{\text{theo}}(E3, \nu 1j_{15/2} \rightarrow \nu 2g_{9/2}) = \frac{245}{\pi\, 572} \cdot e^2 \cdot \left\langle \nu 2g_{9/2} \left| r^3 \right| \nu 1j_{15/2} \right\rangle^2 = 7273.3 \text{ e}^2 \text{ fm}^6$$

with the radial matrix element $\left\langle \nu 2g_{9/2} \left| r^3 \right| \nu 1j_{15/2} \right\rangle = 230.97$ fm$^3$. The comparison of the two values gives the effective E3 charge:

$$e_{\text{eff}} = 1.35\ e$$

[2] The reduced angular matrix element writes [Bohr69, (p. 387)]

$$\langle n_2 l_2 j_2 \| Y_\lambda \| n_1 l_1 j_1 \rangle = i^{l_1+\lambda-l_2} \cdot (-1)^{j_1+\lambda-j_2} \cdot \left( \frac{(2\lambda+1)(2j_1+1)}{4\pi} \right)^{1/2} \cdot \left\langle j_1 \tfrac{1}{2} \lambda 0 \left| j_2 \tfrac{1}{2} \right. \right\rangle$$

and radial matrix element

$$\left\langle n_2 l_2 j_2 \left| r^\lambda \right| n_1 l_1 j_1 \right\rangle = \int_0^\infty \mathcal{R}_{n_2 l_2 j_2} r^\lambda \mathcal{R}_{n_1 l_1 j_1} r^2 dr$$

which represents the coupling to the higher frequency $3^-$ core excitations. The range, that is compatible with the experimental error is $0.95\ e \leq e_{\rm eff} \leq 1.6\ e$. In her earlier work, I. Hamamoto deduced $e_{\rm eff} \geq 0.9\ e$ [Ham69, Ham74], at the lower limit of the experimental uncertainties. The presently obtained neutron polarization charge compares well to the $e_{\rm eff} = 1.5\ e$ deduced for a very similar transition in $^{147}$Gd, $B(E3, \nu 1i_{13/2} \rightarrow \nu 2f_{7/2}) = 8.1$ W.u. [Pii90]. Therefore the model reproduces the measured $B(E3, 15/2^- \rightarrow 9/2^+)$ in $^{209}$Pb with a reasonable effective charge for the single particle transition.

With the results from above and $B(E3, 6^+ \rightarrow 3^-) = 2 \times 34.0(5)$ W.u. the model E3 transition strength for the decay of the $21/2^+$ to the $15/2^-$ state (see also Figure 3.13 for details) is

$$B(E3, 21/2^+ \rightarrow 15/2^-) = 50 \text{ W.u.} = 129750 \text{ e}^2 \text{ fm}^6$$

which with the transition energy of $E_\gamma = 2419$ keV leads to the half life of $T_{1/2} \simeq 20$ ps. The transition is enhanced by a factor of 1.5 relative to the $3^- \rightarrow 0^+$ in $^{208}$Pb, which is a signature for the double octupole admixture to the $21/2^+$ state. The measurement of the reduced transition probability $B(E3, 21/2^+ \rightarrow 15/2^-)$ would certainly give us a chance to learn more about particle octupole-vibration coupling.

In analogy to $^{209}$Pb we evaluated the data available for $^{207}$Pb and $^{207}$Tl. The shell-model orbitals corresponding to $\nu 2g_{9/2}$ and $\nu 1j_{15/2}$ in $^{209}$Pb are $\nu 2f_{7/2}^{-1}$ and $\nu 1i_{13/2}^{-1}$ in $^{207}$Pb and $\pi 2d_{5/2}^{-1}$ and $\pi 1h_{11/2}^{-1}$ in $^{207}$Tl; they differ in orbital angular momentum by $1\hbar$ and $2\hbar$ respectively, relative to those in $^{209}$Pb. A major difference arises however from the fact that the $\nu 2f_{7/2}^{-1}$ and $\pi 2d_{5/2}^{-1}$ orbitals are located at higher energy than the $\nu 1i_{13/2}^{-1}$ and $\pi 1h_{11/2}^{-1}$, whereas in $^{209}$Pb $\nu 2g_{9/2}$ is below $\nu 1j_{15/2}$. Therefore the mixing is expected to be larger for the $7/2^-$ states in $^{207}$Pb and the $5/2^+$ states in $^{207}$Tl and smaller for the higher spin states in these nuclei. Table 3.9 shows the level energies that have been used to determine the parameters of the model and the calculated energies and wave functions. The level schemes and the energies of the unperturbed states that result from the calculations are presented in Figure 3.14. The model wave function of the $7/2^-$ levels in $^{207}$Pb predicts that 22% of the $\nu 2f_{7/2}$ strength in the neutron pick up from $^{208}$Pb is shifted from the 2340 keV level to a level at 4836 keV. The results of the $^{208}$Pb(p,d) reaction [Smi71] give 10% of the strength in a level at 4520 keV and 6% in a $(7/2, 5/2)^-$ level at 5470 keV. The summed strength of these two states and their weighted mean energy are close to the model predictions. The result of an analogous measurement with the (d,t)-reaction [Moy70] shows 20% strength in only one level at 4546 keV. The experimental data agree with the model, as they show that about 20% of the single particle $\nu 2f_{7/2}$ strength is shifted to the energy region, where the $\nu 1i_{13/2} \times 3^-$ multiplet lies.

The particle octupole vibration calculations for $^{207}$Tl (see Table 3.9), predict around 19% $\pi 2d_{5/2}$ pick up strength in a level at 4584 keV relative to the main one hole state at 1683 keV. Grabmayr et al. found in the $^{208}$Pb(d,$^3$He) reaction [Gra92] 4% at 4696 keV, $\leq$ 6% for a state at 4574 keV and $\leq$ 3% at 4296 keV. The absolute spectroscopic factor for the 1683 keV level is only 63% of the sum rule strength. So again the main feature, that around 10% of the $\pi 2d_{5/2}$ single hole is found at the energy of the $\pi 1h_{11/2} \times 3^-$ multiplet agrees between model and experiment. Possible reasons, that this simple model cannot describe reality in detail, are discussed below.

So far it has been checked, if the model reproduces the experimental data with coupling matrix elements taken from part of the experimental data. Another criterion for the validity of particle octupole coupling is, if these empirical matrix elements agree with the theoretical estimate, as presented above. The comparison is to be found in Table 3.8. Astonishingly good agreement is found; the empirical element is 70, 87 and 100% of the theoretical for $^{209}$Pb, $^{207}$Pb and $^{207}$Tl. Therefore a slightly reduced theoretical matrix element should also be applicable for other single particle orbitals. The presently derived coupling matrix elements are also in excellent agreement with the values calculated by I. Hamamoto [Ham74] and used later to reproduce the experimental data in At, Rn and Fr nuclei [Pol86, Byr86, Byr94, Byr98].

The coupling element has also been derived for the very similar case of the $2f_{7/2}$ and $1i_{13/2}$ proton from more complicated many particle states in astatin nuclei [Byr98] as $h(1i_{13/2},\ 2f_{7/2} \times 3^-) = -910$ keV also in very good agreement with theory [Ham74].

The exact calculations describing the particle octupole-vibration phenomenon in nuclei with more valence particles(holes) like $^{206}$Pb and $^{205}$Tl or characterized by the particle-hole excitations ($^{208}$Pb) are more difficult. Also the additional information on the two body residual interaction between the valence particles is often not available. Therefore, we restrict ourselves only to the qualitative description concerning these nuclei using however, the information deduced already from the levels observed in the one particle(hole) neighbours of $^{208}$Pb.

An interesting and very useful feature, for the first time evident in the present data, is presented in Table 3.10. The energy shift of the octupole vibration based on states with two excited particles or holes is compared with that of the individual particles (holes). It turns out that the individual shifts can be simply added for stretched configurations or more generally calculated by simple angular momentum recoupling. This is accurate within 2 to 36 keV. The reason for this additivity is that the coupling is still small and therefore higher order terms like an octupole-octupole interaction can be neglected. This feature complements the fact, that one

Table 3.10 The energy shifts for the states resulting from particle octupole-vibration coupling in nuclei with two quasi-particles outside the $^{208}$Pb core. The following shorthand was used for the energy shifts: $\Delta E_1 \equiv \Delta E(^{209}\mathrm{Pb},\ 21/2^+)$, $\Delta E_2 \equiv \Delta E(^{207}\mathrm{Pb},\ 19/2^-)$, $\Delta E_3 \equiv \Delta E(^{207}\mathrm{Pb},\ 11/2^+)^\dagger$, $\Delta E_4 \equiv \Delta E(^{207}\mathrm{Tl},\ 17/2^+)$. All energies are given in keV.

| Nucleus | $^{208}$Pb | $^{206}$Tl | $^{205}$Pb | $^{205}$Pb |
|---|---|---|---|---|
| State | 9062 | 4976 | 6430 | 5218 |
| Spin | $(17^+)$ | $(15^+)$ | $15^-$ | $12^+$ |
| Conf. | $\nu 1j_{15/2}1i_{13/2}^{-1} \times 3^-$ | $\pi 1h_{11/2}^{-1}\nu 1i_{13/2}^{-1} \times 3^-$ | $\nu 1i_{13/2}^{-2} \times 3^-$ | $\nu 1i_{13/2}^{-1}2f_{5/2}^{-1} \times 3^-$ |
| $\Delta E_{\mathrm{EXP}}$ | $-297$ | $-282$ | $-212$ | $-56$ |
| $\Delta E_{\mathrm{CAL}}$ | $-326$ | $-280$ | $-200$ | $-92$ |
| Comments | $\Delta E_1 + \Delta E_2$ | $\Delta E_4 + \Delta E_2$ | $\frac{20}{13} \cdot \Delta E_2$ | $\Delta E_2 + \Delta E_3$ |
| | $(-196) + (-130)$ | $(-150) + (-130)$ | $\frac{20}{13} \cdot (-130)$ | $(-130) + (38)$ |

† - The candidate for the state of $(\nu 2f_{5/2}^{-1} \times 3^-,\ 11/2^+)$ configuration in $^{207}$Pb has been observed at 3223(2) keV in $^{207}$Pb(p, p′) reaction [Wag75].

can usually treat the real single particles, that often contain an octupole admixture, as pure single particles. This has been used frequently in the interpretations of the level schemes as presented above, for instance the $11^-$ level in $^{210}$Pb has been described as $\nu 2g_{9/2}1j_{15/2}$ without considering the sizeable admixtures of the $\nu 1j_{15/2}$ orbital explicitly. Only, if the Pauli principle blocks the $3^-$ admixture in a particular state, this is no longer possible.

The results on particle octupole-vibration coupling might be summarized as follows:

1. The cases that have been found here are strongly influenced by this coupling, the coupling matrix elements are large.

2. The relevant states are on or close to the yrast line in a region of low level density; therefore mixing with other configurations is not very important. It does however exist and causes deviations between model and reality.

3. The previous two points combined mean, that the presented cases are especially well suited to explore the particle octupole-vibration coupling.

4. The model gives a consistent description of the measured data, meaning that

parameters derived from one part of the data describe other data well. The deviations can be attributed to point 2 above.

5. The theoretically expected coupling matrix elements agree astonishingly well with experiment.

6. It has been verified by experiment that the effects due to octupole admixtures of two particle states can be calculated from those of the one particle states. The model is therefore applicable for a range of nuclei.

# Chapter 4

# Shell-Model Calculations

## 4.1 Two Body Residual Interaction and Single-Particle Energies

Since the introduction of the nuclear shell model it has been tried extensively to determine the residual interaction well enough, that it can describe detailed nuclear properties. These attempts have been especially successful for the nuclei in the $^{208}$Pb region. $^{208}$Pb is often considered to be the best doubly magic nucleus, in other words it might be considered as a spherical, inert hard core, when describing neighbouring nuclei. The excitations in nuclei in the vicinity of $^{208}$Pb involve then only few particles or holes. Therefore, this region of nuclei has attracted the interest of experimentalists and theoreticians. It serves as a crucial test ground for the nuclear shell model theory and in particular for parameterizations of the residual interaction.

Residual interactions, that are derived from the measured interaction between free nucleons, are of fundamental interest. A particularly successful approach to derive the residual interaction is that of Kuo and Herling (KH) [Kuo68, Kuo71]. They derived the residual interaction of particle-particle and hole-hole type from the free nucleon-nucleon potential of Hamada and Jonston [Ham62] using reaction-matrix techniques as in ref. [Kuo66] and with renormalizations to account for the truncated model space. Many properties of the nuclei around $^{208}$Pb could be well described with this interaction and an inert $^{208}$Pb core. McGrory and Kuo [McG75] and later on Warburton and Brown [War91] have shown that minor modifications applied to the core polarization component of the (KH) residual interaction result in still significantly improved agreement with the experimental data.

To perform shell-model calculations for states in nuclei near $^{208}$Pb of a higher spin, than is allowed for the valence particles or holes alone, particle-hole core excitations have to be included. Since the calculations become rapidly more arduous with the number of active particles and orbitals such calculations are especially difficult for this region of nuclei. The most extensive calculations so far, including particle-hole excitations of the $^{208}$Pb core, were performed by Poppelier et al. [Pop88]. The authors calculated excited states in several nuclei in this region using the schematic Surface Delta Interaction (SDI). The single particle energies and SDI strength parameters were determined from a fit to the available set of experimental level energies. The configuration space was truncated due to computational limits to 14 orbits, i.e. the 3 proton and 3 neutron particle orbits and 4 proton and 4 neutron hole orbits, that are lowest in energy. The Coulomb repulsion of protons was omitted in this approach.

The development of experimental techniques has greatly improved the information about nuclei in this region especially on high spin excited states. This fact triggered studies to develop a residual interaction for an extended configuration space that is capable to reproduce and predict with high accuracy the high spin states in nuclei of interest. The previous computational limits were removed with modern and powerful computers. The shell-model codes allow to handle calculations of large dimensions. The aim of the present work is to test a set of realistic residual interaction matrix elements for the full Kuo-Herling configuration space.

The Kuo and Herling [Kuo68, Kuo71] residual interaction of particle-particle type for protons and neutrons modified by Warburton and Brown [War91] has been used in our present shell-model calculations for the orbitals above $^{208}$Pb. For the hole-hole interaction (the orbitals below $^{208}$Pb) TBME of Kuo and Herling [Kuo68, Kuo71] were used as given by Rydström and Blomqvist et al. [Ryd90] for proton-proton and proton-neutron multiplets. The neutron-neutron TBME were taken from McGrory and Kuo [McG75]. Kuo and Herling did not calculate the interaction between particle and hole orbitals. These TBME were now calculated by B.A. Brown [Bro] according to the Kuo-Brown procedure from the H7B free nucleon potential [Hos85].

This set of residual interaction matrix elements was the input for the shell-model code OXBASH [Bro84], which we used to perform the numerical calculations. The calculations were performed in all-particles mode and the proton-neutron formalism. The diagonal two body matrix elements for protons included the Coulomb contribution which averages $\sim 250$ keV.

Our calculations used a model space consisting of the 24 lowest orbits in $^{208}$Pb, i.e. the nearest 5 proton-hole, 6 neutron-hole, 6 proton-particle and 7 neutron-particle

orbits (see Figure 1.2). This space has $^{132}_{50}Sn_{82}$ as core and extends to $^{310}_{126}X_{184}$. The single particle energies were taken from the yrast states of $^{207}$Tl, $^{207}$Pb, $^{209}$Bi, and $^{209}$Pb and their energy is given relative to $^{208}$Pb in the Figure. 1.2. This is the usual choice together with the Kuo-Herling interaction [War91]. The structure of these yrast states is also predominantly of one particle(hole) character. This is indicated in the Figure 1.2. There are however admixtures to these states of one particle-one hole or collective character, that influence their experimental energy. If, as in most previous calculations, core excitations are not included, then these empirical single particle energies are the best choice. If on the other hand the calculations can include explicitly admixtures of core excitations, different single particle energies should be used. Examples for these effects will be presented for individual states below. Another complication arises when a given admixture of an effective single particle state is forbidden by the Pauli principle in a coupled many particle state. Often the levels with the highest spin of a given configuration cannot be composed from the admixed configurations. Then the appropriate single particle energies are also different. Points like this have to be considered in the interpretation of results of the calculations below.

## 4.2 Particle-Hole Excitations in $^{208}$Pb

The new part of the interaction is between particles and holes. It therefore manifests itself directly in the states of $^{208}$Bi for proton neutron-hole states, $^{208}$Tl for neutron proton-hole states and in the excited states of $^{208}$Pb for proton proton-hole and neutron neutron-hole levels. Much detailed new information has been gained on $^{208}$Pb recently [Sch97, Val97, Yeh97], while still very little is known about $^{208}$Tl, and $^{208}$Bi is not well known either. Particle-hole excitations of the $^{208}$Pb core are also essential for the low lying high spin states in nuclei near $^{208}$Pb. Therefore, in this section we treat first calculations of one particle - one hole and two particle - two hole states in $^{208}$Pb with the new residual interaction [Bro, Hos85] based on the H7B potential.

In the following only the example represantative states are detailed. The complete list of the calculated excitation energies of levels in $^{208}$Pb is to be found in Tables 6.3 and 6.4.

The calculated wave functions and excitation energies of the lowest six states of spin-parity $5^-$ in $^{208}$Pb are presented in Table 4.1. These calculations allowed only one particle to be excited from $^{208}$Pb. More precisely, Table 4.1 gives the squared amplitudes of the six particle-hole configurations of lowest unperturbed energy. The

Table 4.1 The energies and the wave functions of the lowest six $5^-$ states as calculated in the present work. The squared amplitudes of the wave functions are given, the level energies are in keV. The experimental energies of the levels [Sch97] and the empirical wave functions [Sch93, Rej95] are presented in *italic*. See also text.

| Energy[keV] | 3267 | 3875 | 4037 | 4238 | 4302 | 4430 |
|---|---|---|---|---|---|---|
| | *3197.7* | *3708.5* | *3961.1* | *4125.4* | *4180.2* | *4296.7* |
| Configuration | Occupation | | | | | |
| $\nu 2g_{9/2}3p^{-1}_{1/2}$ | 0.743 | 0.194 | 0.000 | 0.023 | 0.000 | 0.004 |
| | *0.903* | *0.068* | *0.002* | *0.002* | *0.006* | *0.005* |
| $\pi 1h_{9/2}3s^{-1}_{1/2}$ | 0.011 | 0.109 | 0.473 | 0.097 | 0.260 | 0.005 |
| | *0.063* | *0.372* | *0.384* | *0.053* | *0.068* | *0.040* |
| $\nu 2g_{9/2}2f^{-1}_{5/2}$ | 0.020 | 0.325 | 0.313 | 0.246 | 0.000 | 0.001 |
| | *0.023* | *0.397* | *0.518* | *0.017* | *0.012* | *0.012* |
| $\nu 1i_{11/2}3p^{-1}_{1/2}$ | 0.014 | 0.095 | 0.183 | 0.002 | 0.682 | 0.014 |
| | *0.000* | *0.068* | *0.002* | *0.314* | *0.314* | *0.292* |
| $\pi 1h_{9/2}2d^{-1}_{3/2}$ | 0.039 | 0.064 | 0.000 | 0.198 | 0.000 | 0.559 |
| | *0.000* | *0.068* | *0.068* | *0.578* | *0.032* | *0.250* |
| $\nu 2g_{9/2}3p^{-1}_{3/2}$ | 0.019 | 0.070 | 0.006 | 0.411 | 0.023 | 0.387 |
| | *0.000* | *0.006* | *0.006* | *0.029* | *0.548* | *0.384* |
| $\sum$ | 0.846 | 0.857 | 0.975 | 0.977 | 0.965 | 0.970 |
| | *0.989* | *0.979* | *0.980* | *0.993* | *0.980* | *0.983* |

experimental energies of the relevant levels [Sch97] and their empirical wave functions [Sch93, Rej95], derived from experimental data, are shown for comparison in *italic*.

The lowest $5^-$ level is calculated to be at 3267 keV which agrees with the observed energy of 3198 keV. Its main component is the $\nu 2g_{9/2}3p^{-1}_{1/2}$ configuration that contributes 75%. A value of 80% has been deduced from the $^{207}$Pb(d, p) reaction [Sch97] which is in excellent agreement. The empirical wave function indicates a smaller mixing and the $\nu 2g_{9/2}3p^{-1}_{1/2}$ configuration contributes 90%. All other configurations that make up this state have very small amplitudes in the present calculations. This is also in accordance with the empirical approach.

The second $5^-$ state is calculated at 3875 keV, 166 keV higher than the exper-

imental level. Its wave function is significantly more mixed than that of the first $5^-$ state. The $\nu 2g_{9/2}2f_{5/2}^{-1}$ configuration is with 33% strongest, which compares very well to 39% in the empirical approach. For the second and third strong components of $5_2^-$, 19% of $\nu 2g_{9/2}3p_{1/2}^{-1}$ and 11% of $\pi 1h_{9/2}3s_{1/2}^{-1}$, the agreement is worse however. In the empirical wave function $\pi 1h_{9/2}3s_{1/2}^{-1}$ contributes 37% and $\nu 2g_{9/2}3p_{1/2}^{-1}$ about 7%. On the other hand 19% of $\nu 2g_{9/2}3p_{1/2}^{-1}$ excitation in $5_2^-$ was deduced from the $^{207}$Pb(d,p) reaction [Sch97] which is in accordance with our present result. Spectroscopic factors were also measured for $\pi 1h_{9/2}3s_{1/2}^{-1}$ in the $^{209}$Bi(t,$\alpha$) proton pick-up reaction [Sch97] and the corresponding strength is 34% in $5_2^-$ which confirms the empirical wave function. The calculated contributions of higher lying particle-hole excitations, 10% of $\nu 1i_{11/2}3p_{1/2}^{-1}$, 6% of $\pi 1h_{9/2}2d_{3/2}^{-1}$ and 7% of $\nu 2g_{9/2}3p_{3/2}^{-1}$, compare well with the results of the empirical approach; the strength of the last configuration, $\nu 2g_{9/2}3p_{3/2}^{-1}$, is not well determined from experiment.

The third $5^-$ state of excitation energy 3961 keV is calculated to be at 4037 keV. The three leading components of this state, $\pi 1h_{9/2}3s_{1/2}^{-1}$, $\nu 2g_{9/2}2f_{5/2}^{-1}$ and $\nu 1i_{11/2}3p_{1/2}^{-1}$, are calculated to contribute 47%, 31% and 18% respectively. According to the empirical wave function the strength is carried by $\pi 1h_{9/2}3s_{1/2}^{-1}$ (38%) $\nu 2g_{9/2}2f_{5/2}^{-1}$ (52%) and $\pi 1h_{9/2}2d_{3/2}^{-1}$ (7%). Similarly as for the $5_2^-$ some expected strength of the proton particle-hole component is missing and shifted to higher lying states.

For the higher lying $5^-$ states the agreement between the experimental and calculated energy of the levels is of similar quality as for the lowest three. The calculated wave functions however, show greater discrepancies, when compared to the empirical ones. The leading components of the states are interchanged and too large strength of the low lying proton configurations $\pi 1h_{9/2}3s_{1/2}^{-1}$ or $\pi 1h_{9/2}2d_{3/2}^{-1}$ is found in these states as compared to the empirical wave functions and the spectroscopic factors [Sch97].

Another set of representative results, namely the $6^-$ unnatural parity states, are presented in Table 4.2. Again only the squared amplitudes of the five lowest particle-hole configurations are presented. Good agreement, as in the case of the $5^-$ states, has been obtained for the excitation energies of the levels, that are calculated too high by about 100 keV. The empirical wave functions of the $6^-$ states exhibit very little configuration mixing. This feature is typical for unnatural parity states in general and is excellently reproduced by the present calculations. Moreover, the strength of the leading configuration agrees for all states within 5% in both approaches.

The result for the $10^+$ states is presented in Table 4.3. The calculated excitation energies are again too large by about 100 keV. The wave functions are moderately

Table 4.2 The energies and the wave functions of the lowest five $6^-$ states as calculated in the present work. The squared amplitudes of the wave functions are given, the level energies are in keV. The experimental energies of the levels [Sch97] and the empirical wave functions [Sch93, Rej95] are presented in *italic*. See also text.

| Energy[keV] | 4047 | 4298 | 4493 | 4571 | 4824 |
|---|---|---|---|---|---|
| | *3919.9* | *4206.2* | *4383.2* | *4480.7* | *4761.8* |
| Configuration | Occupation | | | | |
| $\nu 2g_{9/2}2f_{5/2}^{-1}$ | 0.980 | 0.000 | 0.000 | 0.014 | 0.000 |
| | *0.980* | *0.000* | *0.008* | *0.000* | *0.000* |
| $\nu 1i_{11/2}3p_{1/2}^{-1}$ | 0.000 | 0.948 | 0.022 | 0.015 | 0.005 |
| | *0.000* | *0.941* | *0.032* | *0.014* | *0.000* |
| $\pi 1h_{9/2}2d_{3/2}^{-1}$ | 0.001 | 0.024 | 0.905 | 0.032 | 0.029 |
| | *0.010* | *0.044* | *0.865* | *0.073* | *0.003* |
| $\nu 2g_{9/2}3p_{3/2}^{-1}$ | 0.015 | 0.008 | 0.043 | 0.924 | 0.002 |
| | *0.001* | *0.005* | *0.084* | *0.865* | *0.036* |
| $\nu 1i_{11/2}2f_{5/2}^{-1}$ | 0.000 | 0.014 | 0.019 | 0.004 | 0.938 |
| | *0.000* | *0.000* | *0.000* | *0.040* | *0.941* |
| $\sum$ | 0.996 | 0.994 | 0.989 | 0.989 | 0.974 |
| | *0.991* | *0.990* | *0.989* | *0.992* | *0.980* |

mixed. The main configurations of the first two $10^+$ states, that lie close to each other, are interchanged in our present calculations relative to the empirical wave functions [Sch93, Rej95]. The empirical wave functions are based on many experimental data and very reliable in this case [Mai97]. The wave functions of the two higher $10^+$ states, that are separated from the lower levels by more than 400 keV, are reproduced with high accuracy.

The yrast states of $^{208}$Pb resulting from the present calculation are presented in Figure 4.1 . Column (a) displays the negative and column (c) the positive parity states. Although the wave functions of the excited states are often mixed, only the leading one particle - one hole and, for states of spin $I \geq 14$, two particle - two hole component is given in the figure. The shell-model predictions are compared to the experimental level scheme of the yrast states in $^{208}$Pb [Sch97], which is shown in column (b).

Table 4.3 The energies and the wave functions of the lowest four $10^+$ states as calculated in the present work. The squared amplitudes of the wave functions are given, the level energies are in keV. The experimental energies of the levels [Sch97] and the empirical wave functions [Sch93, Rej95] are presented in *italic*. See also text.

| Energy[keV] | 4946 | 5178 | 5617 | 6062 |
|---|---|---|---|---|
| | *4895.3* | *5069.4* | *5536.6* | *5928.0* |
| Configuration | Occupation | | | |
| $\nu 2g_{9/2}1i^{-1}_{13/2}$ | 0.267 | 0.714 | 0.018 | 0.000 |
| | *0.624* | *0.144* | *0.212* | *0.017* |
| $\pi 1h_{9/2}1h^{-1}_{11/2}$ | 0.431 | 0.096 | 0.287 | 0.160 |
| | *0.325* | *0.436* | *0.130* | *0.109* |
| $\nu 1j_{15/2}2f^{-1}_{5/2}$ | 0.162 | 0.142 | 0.674 | 0.016 |
| | *0.036* | *0.260* | *0.656* | *0.044* |
| $\nu 1i_{11/2}1i^{-1}_{13/2}$ | 0.113 | 0.038 | 0.014 | 0.820 |
| | *0.002* | *0.168* | *0.000* | *0.828* |
| $\sum$ | 0.973 | 0.990 | 0.993 | 0.996 |
| | *0.987* | *1.008* | *0.998* | *0.998* |

The first excited state is the collective $3^-$. This state is interpreted as an octupole surface vibration of the nucleus in a macroscopic approach. In a microscopic description it is built mainly by many one particle - one hole excitations. In our calculations for the $3^-$ excitation we allowed only one particle to be excited from $^{208}$Pb core. The resulting excitation energy, as shown in Figure 4.1a, is 150 keV lower than in experiment. The calculated particle-hole wave function of the lowest $3^-$ state is presented in Table 4.4. The collectivity of this state is exhibited by the great fragmentation of the wave function over many components. The contribution of the strongest configuration does not exceed 20%. The leading three configurations, with contributions larger than 10% each, follow the rule of the stretched anti-parallel coupling with respect to the $(l)$ and $(j)$ quantum numbers of particles and holes.

The states of spin-parity $5^-$, $6^-$ and $10^+$ were discussed already earlier. The $7^-$ state observed experimentally at 4038 keV excitation energy [Sch97], is reproduced very well in our present work. Its calculated wave function consist of 98%

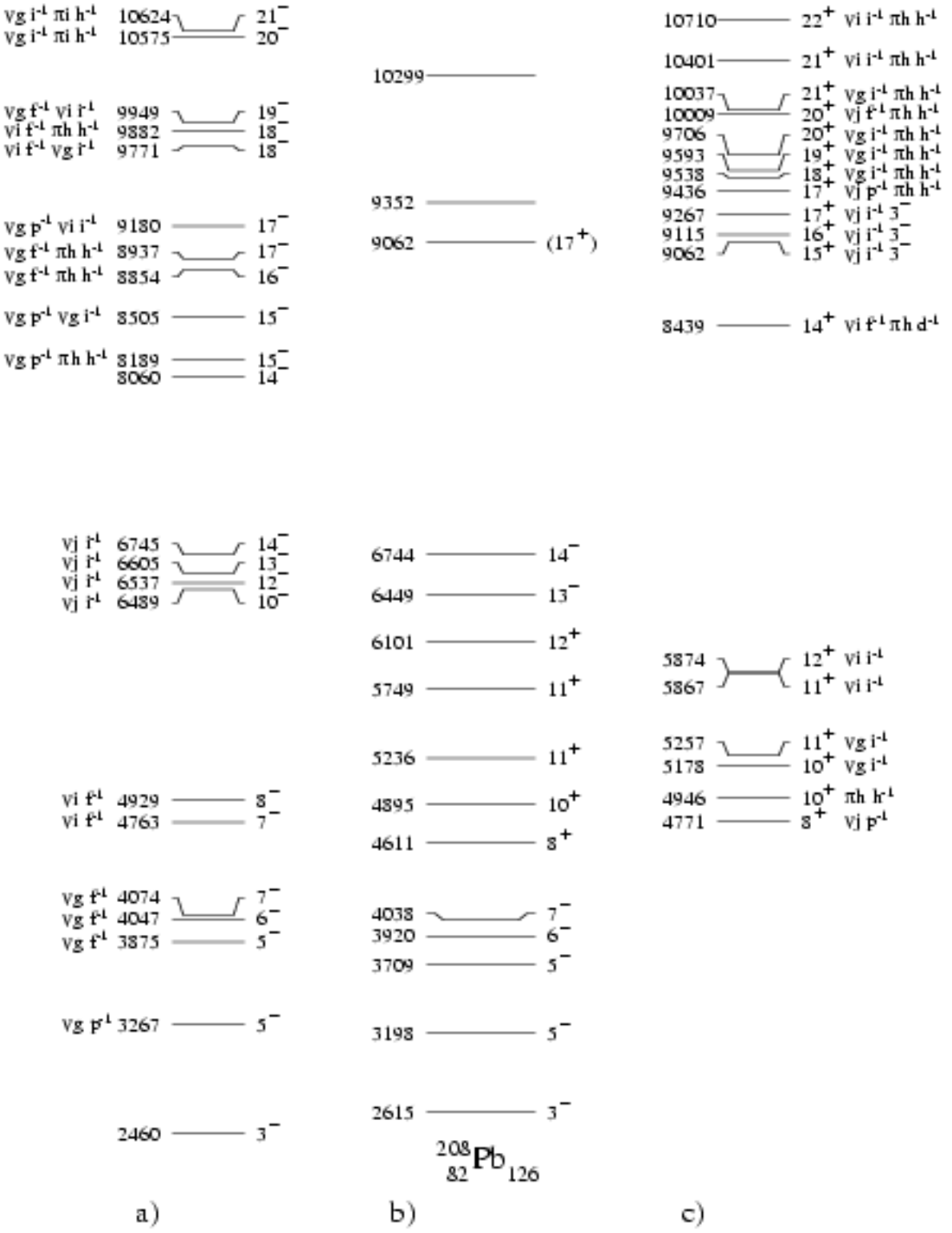


Figure 4.1 Comparison of the experimental b) level scheme of $^{208}$Pb with the results of shell-model calculations. Column a) shows the negative and c) the positive parity states. The leading configuration of the state is also given. The following shorthand is used for the configurations: protons ($\pi$) $h \equiv 1h_{9/2}$, $i \equiv 1i_{13/2}$, $h^{-1} \equiv 1h^{-1}_{11/2}$ and neutrons ($\nu$) $g \equiv 2g_{9/2}$, $i \equiv 1i_{11/2}$, $j \equiv 1j_{15/2}$, $p^{-1} \equiv 3p^{-1}_{1/2}$, $f^{-1} \equiv 2f^{-1}_{5/2}$, $i^{-1} \equiv 1i^{-1}_{13/2}$. All energies are given in keV.

Table 4.4 The squared amplitudes ($A^2$) of the wave function of the lowest collective $3^-$ state in $^{208}$Pb, as calculated in the present work. The calculations allowed only the excitation of one particle. Only components with $A^2 \geq 0.001$ are listed.

| Configuration | $A^2$ | Configuration | $A^2$ | Configuration | $A^2$ |
|---|---|---|---|---|---|
| $\pi 1h_{9/2}2d^{-1}_{3/2}$ | 0.170 | $\nu 2g_{9/2}2f^{-1}_{5/2}$ | 0.026 | $\nu 2g_{7/2}3p^{-1}_{3/2}$ | 0.007 |
| $\nu 2g_{9/2}3p^{-1}_{3/2}$ | 0.124 | $\nu 2g_{7/2}3p^{-1}_{1/2}$ | 0.023 | $\nu 3d_{5/2}2f^{-1}_{7/2}$ | 0.007 |
| $\nu 1i_{11/2}2f^{-1}_{5/2}$ | 0.108 | $\pi 2f_{7/2}2d^{-1}_{3/2}$ | 0.023 | $\nu 2g_{7/2}2f^{-1}_{7/2}$ | 0.006 |
| $\nu 1j_{15/2}1i^{-1}_{13/2}$ | 0.082 | $\nu 2g_{7/2}2f^{-1}_{5/2}$ | 0.022 | $\nu 3d_{5/2}2f^{-1}_{5/2}$ | 0.005 |
| $\pi 1i_{13/2}1h^{-1}_{11/2}$ | 0.068 | $\nu 3d_{3/2}3p^{-1}_{3/2}$ | 0.017 | $\pi 3p_{1/2}2d^{-1}_{5/2}$ | 0.005 |
| $\pi 2f_{7/2}3s^{-1}_{1/2}$ | 0.055 | $\pi 2f_{5/2}2d^{-1}_{3/2}$ | 0.016 | $\nu 3d_{3/2}2f^{-1}_{5/2}$ | 0.004 |
| $\nu 2g_{9/2}2f^{-1}_{7/2}$ | 0.037 | $\pi 2f_{5/2}3s^{-1}_{1/2}$ | 0.016 | $\pi 3p_{3/2}2d^{-1}_{5/2}$ | 0.004 |
| $\nu 1i_{11/2}1h^{-1}_{9/2}$ | 0.036 | $\nu 3d_{5/2}3p^{-1}_{3/2}$ | 0.012 | $\nu 1i_{11/2}2f^{-1}_{7/2}$ | 0.003 |
| $\pi 2f_{7/2}2d^{-1}_{5/2}$ | 0.032 | $\pi 3p_{3/2}2d^{-1}_{3/2}$ | 0.009 | $\nu 3d_{3/2}2f^{-1}_{7/2}$ | 0.003 |
| $\pi 1h_{9/2}1g^{-1}_{7/2}$ | 0.032 | $\pi 1h_{9/2}2d^{-1}_{5/2}$ | 0.009 | $\pi 2f_{5/2}1g^{-1}_{7/2}$ | 0.002 |
| $\nu 3d_{5/2}3p^{-1}_{1/2}$ | 0.027 | $\pi 2f_{5/2}2d^{-1}_{5/2}$ | 0.008 | $\nu 2g_{7/2}1h^{-1}_{9/2}$ | 0.001 |

of the $\nu 2g_{9/2}2f^{-1}_{5/2}$ configuration, which is in excellent agreement with the empirical counterpart [Sch93, Rej95]. The next $7^-_2$ state was observed at 4680 keV [Sch97]; it is not present in the figure. Its wave function was estimated to be mainly of $\nu 1i_{11/2}2f^{-1}_{5/2}$ configuration [Sch93, Rej95]. The calculated $7^-_2$ is only about 80 keV too high in the excitation energy and its main ingredient, $\nu 1i_{11/2}2f^{-1}_{5/2}$ configuration, constitutes 86% of the state. The next yrast state with $I^\pi = 8^+$ is calculated too high in energy by about 160 keV and its main component is $\nu 1j_{15/2}3p^{-1}_{1/2}$ with 74%. The empirical wave function indicates larger mixing however, the leading particle-hole configuration contributes only about 60%, which causes a stronger binding of the $8^+$ state. The calculated energies of the two lowest $11^+$ states are 5257 keV and 5867 keV and their wave functions are very pure. The leading particle-hole components, $\nu 2g_{9/2}1i^{-1}_{13/2}$ and $\nu 1i_{11/2}1i^{-1}_{13/2}$ respectively, contribute more than 99% to the corresponding states. This is due to the large energy separation, about 780 keV, between the unperturbed levels. No $\gamma$ transition has been found, that connects the two $11^+$ levels, which is a direct proof that there is very little configuration mixing. The agreement with the experimental excitation energy is very good for $11^+_1$, the second $11^+$ state is about 120 keV too high. The $12^+$ state is calculated by about 230 keV too low, relative to the experimental level. It is a very pure state of the $\nu 1i_{11/2}1i^{-1}_{13/2}$

configuration. The next particle-hole excitation that can contribute to the $12^+$ state is $\nu 1j_{15/2}1h_{9/2}^{-1}$, but its unperturbed energy is higher by about 2.4 MeV. The calculated energy of the $12^+$ level 5874 keV, is very little shifted from the unperturbed energy 5843 keV of the leading configuration $\nu 1i_{11/2}1i_{13/2}^{-1}$. The experimental energy of 6101 keV indicates a much greater repulsion, between the neutron $1i_{11/2}$ and the neutron-hole $1i_{13/2}$ in this state of stretched spin than has been calculated. The $13^-$ and $14^-$ states are both of $\nu 1j_{15/2}1i_{13/2}^{-1}$ configuration. Excellent agreement in energy is found for the $14^-$ state. The $13^-$ state is calculated too high by 156 keV, which is due to an overestimated repulsion; the unperturbed energy of the $\nu 1j_{15/2}1i_{13/2}^{-1}$ is 6487 keV (see Figure 1.2).

The experimental data on states that are dominantly of two particle - two hole character is very scarce. Only three levels are known [Bro96] above the $14^-$ state, and the spin assignments and structure of the two higher are completely unclear. For these states we performed shell-model calculations that allowed two particles to be excited from the $^{208}$Pb core. The results are also included in Figure 4.1 in columns (a) and (c). The level at 9062 keV (column b) is understood as the $17^+$ state, namely the collective $3^-$ built on top of the $14^-$ level, as discussed already in Section 3.5. The calculation indeed shows a multiplet of the $\nu 1j_{15/2}1i_{13/2} \times 3^-$ configuration at about this energy. The shell model calculation does however not reproduce the energy shift as obtained from particle octupole-vibration coupling (see Section 3.5). The unperturbed energy of the $\nu 1j_{15/2}1i_{13/2} \times 3^-$ configuration is 9204 keV, if the calculated energies 6744 keV for the $14^-$ level and 2460 keV for the $3^-$ are added. The calculated energy of the $17^+$ state is 9267 keV, closed to the unperturbed energy. The downward shift, missing in the calculated energy of the $17^+$ state, reflects the fact that admixtures of $\nu 2g_{9/2}1i_{13/2}^{-1} \times (3^-)^2$ and $\nu 1j_{15/2}2f_{7/2}^{-1} \times (3^-)^2$ states (see Section 3.5), are excluded by the restriction to only 2p-2h states in the calculations. No assignments can be made for the two states of highest excitation energy from the present results and their spins and structure remain unknown.

The above comparison of the results of the present calculation to the experimental data is very satisfactory. The realistic H7B residual force [Hos85], that has no free parameters fitted to the experimental data, predicts the excitation energies of the levels in $^{208}$Pb well. On the average the excitation energies are calculated about 130 keV too high, or the ground state is too low. If one corrects for this most energies are in agreement within 50 keV. It is also capable to reasonably well reproduce the main features of the wave functions. For the states of unnatural parity, that are usually very little mixed, excellent agreement has been obtained between empirical and calculated wave functions. But the interaction reproduces also the

extreme mixing and collectivity of the first $3^-$ level. It is usually very difficult to get the $3^-$ energy low enough in shell model calculations. The large configuration space that has been used here and the H7B interaction give even a too small energy. For the natural parity $5^-$ and $10^+$ states, that show moderate configuration mixing, reasonable to good agreement has been found.

Concerning the particle-hole excitations in a coupled state of spin near maximal angular momentum the following systematic trends have been found for yrast states; ($j_p$ and $j_h$ are spins of particle and hole, $l$ and $s$ are orbital and spin angular momentum of particle(hole) respectively)

- states of natural parity with $j_p = l_p + s_p$ and $j_h = l_h + s_h$ are calculated too high in energy
- states of natural parity with $j_p = l_p - s_p$ and $j_h = l_h + s_h$ or $j_p = l_p + s_p$ and $j_h = l_h - s_h$ are calculated too low in energy
- states of unnatural parity with $j_p = l_p + s_p$ and $j_h = l_h + s_h$ are calculated too low in energy

## 4.3 Core Excitations in Nuclei Adjacent to $^{208}$Pb

New experimental information on high spin states in nuclei adjacent to $^{208}$Pb has been established in the present study. In particular for $^{209}$Pb levels involving particle-hole excitations of the $^{208}$Pb core coupled to a valence neutron have been recognized and discussed based on the experimental evidence and empirical shell model calculations as described in detail in Section 3.2.

In this section we present the results of shell model calculations and compare them to the presently available experimental data. The important TBME of the residual interaction for this comparison are those describing two particle - one hole (2p - 1h) multiplets. Of those, the neutron-neutron TBME (see Figure 3.3 and ref. [War91]) and proton-neutron TBME (see ref. [War91]) were shown to excellently describe the experimental data of the states with a few particles outside of $^{208}$Pb in its ground state as core. The newly calculated particle-hole TBME, as described in the previous section, also provide a good description of experimentally observed levels in $^{208}$Pb.

In Figure 4.2, the yrast states in $^{209}$Pb resulting from the shell-model calculations are presented. Only the levels built of dominantly 2p - 1h components, that is states involving one valence neutron coupled to one particle- one hole excited states of the

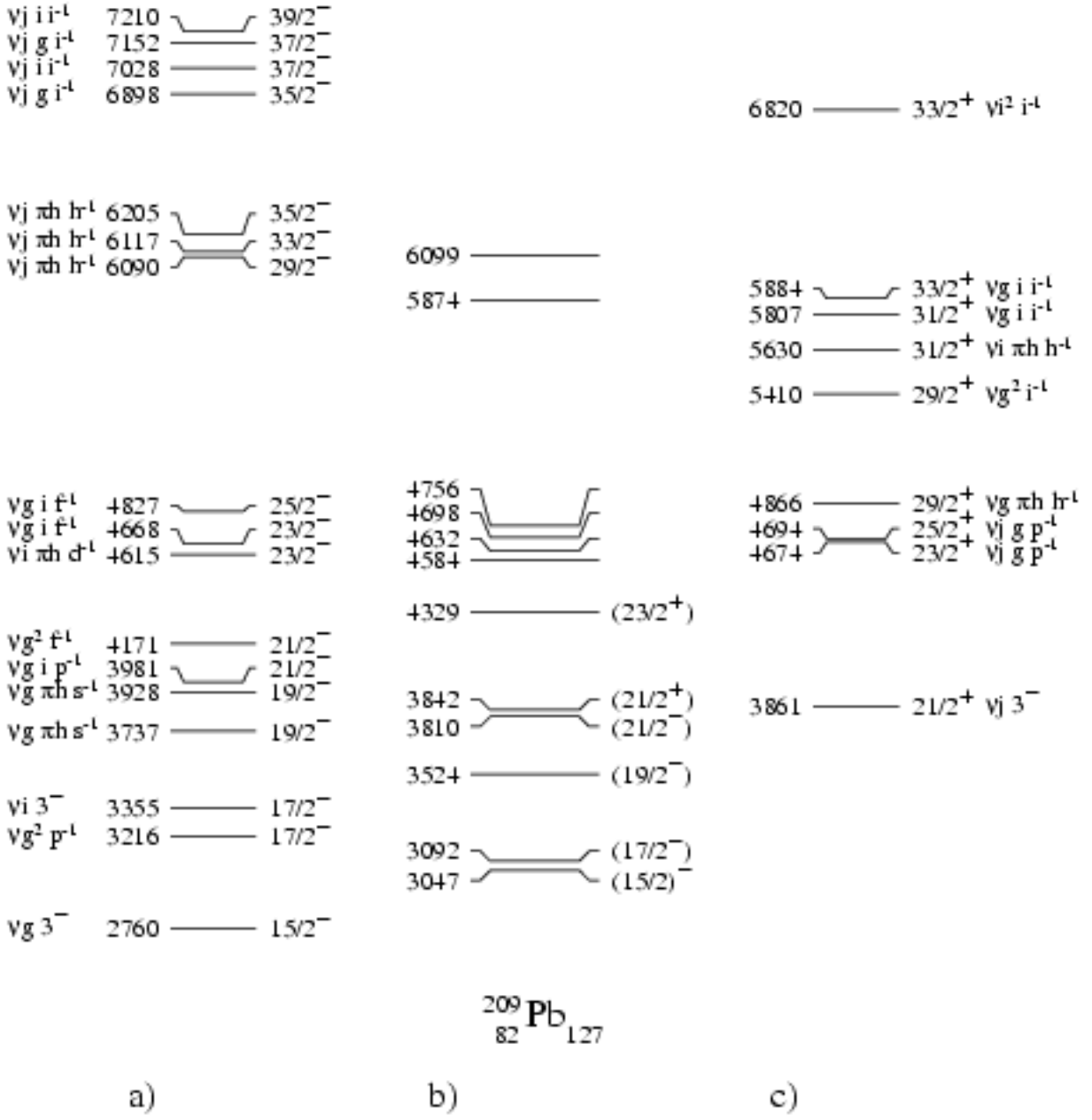


Figure 4.2 Comparison of the experimental b) level scheme of $^{209}$Pb with the results of shell-model calculations. Column a) shows the negative and c) the positive parity states. The leading configuration of the state is also given. The following shorthand is used for the configurations: protons ($\pi$) $h \equiv 1h_{9/2}$, $s^{-1} \equiv 3s^{-1}_{1/2}$, $d^{-1} \equiv 2d^{-1}_{3/2}$, $h^{-1} \equiv 1h^{-1}_{11/2}$ and neutrons ($\nu$) $g \equiv 2g_{9/2}$, $i \equiv 1i_{11/2}$, $j \equiv 1j_{15/2}$, $p^{-1} \equiv 3p^{-1}_{1/2}$, $f^{-1} \equiv 2f^{-1}_{5/2}$, $i^{-1} \equiv 1i^{-1}_{13/2}$. All energies are given in keV.

$^{208}$Pb core, are included in the figure. The leading configuration for each state is indicated. In column (a) the negative and in column (c) the positive parity states are shown. The shell-model predictions are compared to the experimental yrast levels of $^{209}$Pb that are shown in column (b) (see also Section 3.2).

The energies are presented as calculated without any shift, meaning that the ground state of $^{208}$Pb has energy 0 keV. Throughout these calculations the single particle energies are taken from the experimental levels, as an example the $\nu 2g_{9/2}$ energy from the ground state of $^{209}$Pb. Because the present calculations include particle-hole excitations of $^{208}$Pb, the calculated ground state of $^{209}$Pb will also contain some two particle - one hole components, and its energy is shifted consequently. (The predominantly single particle states $2g_{9/2}$, $1i_{11/2}$ and $1j_{15/2}$ are calculated too low by 500 keV). However, the levels, that are discussed here, are 2p - 1h states already with their main component. Therefore the model space, that is restricted to 2p - 1h configurations, does not allow any admixtures of 3p - 2h configurations. Consequently the "particles" have to be "pure particles", not "dressed" by particle-hole excitations, and the chosen single particle energies are appropriate.

The second $15/2^-$ state is calculated to be at 2760 keV excitation energy which compares to 3047 keV observed in the experiment. The structure of this level has been described earlier, in terms of the particle to octupole-vibration coupling model (see Section 3.5), as mainly $\nu 2g_{9/2} \times (3^-,\ ^{208}\mathrm{Pb})$ (83%) with a small admixture of the $\nu 1j_{15/2} \times (0^+,\ ^{208}\mathrm{Pb})$ configuration (17%). The presently calculated wave function of $15/2_2^-$ exhibits a large collectivity, thus a large contribution of the $\nu 2g_{9/2} \times (3^-,\ ^{208}\mathrm{Pb})$ configuration. The excitation of a single neutron in the $1j_{15/2}$ orbital contributes only about 5%. The calculated $15/2_2^-$ state lies 287 keV lower than its experimental counterpart. One reason for this is the too low energy of the $3^-$ excited state calculated in $^{208}$Pb at 2460 keV. The calculated energy of 2760 keV is larger by 300 keV than the unperturbed energy 2460 keV of the $(\nu 2g_{9/2} \times 3^-,\ 15/2^-)$ state due to mixing with the $\nu 1j_{15/2}$ state. There is, however much less mixing than deduced above from particle-octupole coupling. The $\nu 1j_{15/2}$ configuration contributes only 5% in the shell model calculation instead of 17% (see also Section 3.5). Larger mixing would increase the calculated energy of $15/2_2^-$ due to the increased repulsion of the two $15/2_2^-$ states.

The next yrast state observed in the experiment is $(17/2^-)$ at 3092 keV. It has been interpreted as dominantly belonging to the $\nu 2g_{9/2}^2 3p_{1/2}^{-1}$ configuration (see Section 3.2). In our calculations the lowest $17/2^-$ state is at 3216 keV and consists of about 70% of $\nu 2g_{9/2}^2 3p_{1/2}^{-1}$ and a number of other core excitations coupled to the $2g_{9/2}$ neutron. The calculated structure of this level is very similar to the $5_1^-$ state in

$^{208}$Pb plus one neutron in the $2g_{9/2}$ orbital and therefore can be interpreted as mainly $\nu 2g_{9/2} \times 5^-_1$ configuration. Also the energy difference $(E_{cal} - E_{exp},\ 17/2^-) = 124$ keV in $^{209}$Pb compares well with $2 \times (E_{cal} - E_{exp},\ 5^-) = 138$ keV in $^{208}$Pb. The second $17/2^-$ level is calculated at 3355 keV and has not been observed in the experiment. Its structure, similarly as in the case of the $15/2^-_2$ level, indicates a parentage of the collective $3^-$ state. Here, the $3^-$ vibration is built on top of the $\nu 1i_{11/2}$ single particle state, instead of $\nu 2g_{9/2}$ in the previous case.

The lowest $19/2^-$ state is calculated at 3737 keV which is in good agreement with the experimental energy of 3524 keV. The leading configuration, 55% of the $19/2^-_1$ level, is $\nu 2g_{9/2}\pi 1h_{9/2}3s^{-1}_{1/2}$. The main admixtures to this state are 16% of $\nu 2g_{9/2}1i_{11/2}3p^{-1}_{1/2}$, 7% of $\nu 2g_{9/2}\pi 1h_{9/2}2d^{-1}_{3/2}$, 5% of $\nu 2g_{9/2}1i_{11/2}2f^{-1}_{5/2}$ and 4% of $\nu 2g^2_{9/2}2f^{-1}_{5/2}$ respectively where the configurations that contribute less than 4% have been omitted. This state can be also regarded as of the $\nu 2g_{9/2} \times (5^-_2,\ ^{208}\mathrm{Pb})$ configuration. There is, however a strong proton-neutron interaction in the $\nu 2g_{9/2}\pi 1h_{9/2}$ multiplet and neutron-neutron interaction in the $\nu 2g_{9/2}1i_{11/2}$ multiplet at high spin. Therefore the additional $2g_{9/2}$ neutron changes the strengths of the components in the parent $5^-$ state. The overlap of the wave functions describing the $19/2^-_1$ state and the single $5^-$ state, when picking-up the neutron from the $2g_{9/2}$ orbital in the $19/2^-_1$ state, is small. Thus the parentage of $19/2^-_1$ is fragmented over several $5^-$ states in $^{208}$Pb. The second $19/2^-$ has not been observed in the experiment. Its calculated excitation energy is 3928 keV; the leading components of the wave function are $\nu 2g_{9/2}\pi 1h_{9/2}3s^{-1}_{1/2}$, $\nu 2g_{9/2}\pi 1h_{9/2}2d^{-1}_{3/2}$ and $\nu 2g^2_{9/2}2f^{-1}_{5/2}$ contributing 31%, 29% and 23% respectively.

The $(21/2^-)$ level has been observed in experiment at 3810 keV. Its structure was interpreted as mainly due to the $\nu 1i_{11/2}2g_{9/2}3p^{-1}_{1/2}$ configuration with maximal angular momentum. The calculated $21/2^-_1$ level is at 3981 keV. The wave function of this level is dominated by $\nu 1i_{11/2}2g_{9/2}3p^{-1}_{1/2}$ that constitutes 73% of the state. Admixtures of $\nu 1i_{11/2}\pi 1h_{9/2}3d^{-1}_{3/2}$ and $\nu 1i_{11/2}\pi 2f_{7/2}3d^{-1}_{3/2}$ with 9% and 5% respectively have been calculated for this state. In terms of the $^{208}$Pb core excited states it is to be described as mainly $\nu 1i_{11/2} \times (5^-_1,\ ^{208}\mathrm{Pb})$ or the roughly equivalent $\nu 2g_{9/2} \times (6^-_2,\ ^{208}\mathrm{Pb})$. Therefore, we compare the energy shift of $(E_{cal} - E_{exp},\ 21/2^-) = 171$ keV in $^{209}$Pb to $(E_{cal} - E_{exp},\ 5^-_1) + (E_{cal} - E_{exp},\ 6^-_2) = 69$ keV $+ 92$ keV $= 161$ keV in $^{208}$Pb. The next higher $21/2^-$ level, calculated at 4171 keV, again has not been observed in the experiment. The structure of this state is very pure, namely 95% $\nu 2g^2_{9/2}2f^{-1}_{5/2}$, or predominantly $\nu 2g_{9/2} \times (7^-_1,\ ^{208}\mathrm{Pb})$.

The excited state observed in the experiment at 3842 keV has been assigned as the $(\nu 1j_{15/2} \times 3^-,\ 21/2^+)$ excitation (see Section 3.2 and 3.5). The calculations give

a $21/2^+$ state at 3861 keV with dominant $\nu 1j_{15/2} \times 3^-$ configuration. The excellent agreement between the calculated and experimental energy is however somewhat fortuitous, because the collective $3^-$ in $^{208}$Pb is calculated too low.

The next yrast $(23/2^+)$ state established in the experiment is at 4329 keV and was interpreted as mainly of $\nu 1j_{15/2}2g_{9/2}3p^{-1}_{1/2}$ configuration. The calculated level of spin-parity $23/2^+$ is at 4674 keV which is 345 keV higher than the experiment. The main configuration of this state, in accordance to our previous assignment, is $\nu 1j_{15/2}2g_{9/2}3p^{-1}_{1/2}$ that contributes 62%. Of other admixtures, the strongest are $\nu 2g_{9/2}\pi 1h_{9/2}1h^{-1}_{11/2}$ and $\nu 2g_{9/2}\pi 1i_{13/2}2d^{-1}_{3/2}$ which contribute 8% and 6% respectively. This state can be also interpreted, in terms of the parent $^{208}$Pb core excited states, as mainly due to the $\nu 1j_{15/2} \times (5^-_1,\ ^{208}\mathrm{Pb})$ excitation but also in part as the $\nu 2g_{9/2} \times (8^+_1,\ ^{208}\mathrm{Pb})$ configuration. Therefore the large 345 keV energy discrepancy between the calculated and the experimental level is acceptable as the $5^-$ level is calculated already too high by 70 keV and the $8^+$ by 160 keV in $^{208}$Pb.

We performed also shell-model calculations of excited states in $^{207}$Tl and $^{206}$Tl with the same interaction and configuration space. The relevant results are presented in Figures 4.3 and 4.4 respectively. Only the levels resulting from one particle - two hole excitations for $^{207}$Tl and from one particle - three hole excitations for $^{206}$Tl are presented. The calculated states of negative parity are shown in column (a) and states of positive parity in column (c). The experimental levels of $^{207}$Tl (see Section 3.3) are presented in column (b) of Figure 4.3 and the levels of $^{206}$Tl (see Section 3.4) in column (b) of Figure 4.4.

The experimental evidence on high spin states in $^{207}$Tl is very scarce at present. Three new states have been established above the $(\pi 1h^{-1}_{11/2},\ 11/2^-)$ isomer, however only the lowest of those, $(17/2^+)$ at 3813 keV, could be unambiguously identified as dominantly of the $\pi 1h^{-1}_{11/2} \times (3^-,\ ^{208}\mathrm{Pb})$ configuration. This is in accordance with the present calculations (Figure 4.3c) which predict a collective $17/2^+$ state at 3851 keV. The energy agreement is excellent, however again it follows in part from the too low excitation energy of the $3^-$ in $^{208}$Pb rather than from the strength of the particle to octupole-vibration coupling (see Section 3.5). It is not clear yet to which calculated levels the two other experimental states should be assigned.

Six new states have been assigned to $^{206}$Tl above the $(\pi 1h^{-1}_{11/2}\nu 1i^{-1}_{13/2},\ 12^-)$ isomeric state (see Section 3.4). The $(15^+)$ level is interpreted as an octupole vibration on top of the $12^-$ state in $^{206}$Tl. The calculated $15^+$ state exhibits this structure and indeed it is an yrast level.

The levels of spin-parity $(16^+)$ and $(17^+)$ have been observed in the experiment at 5689 keV and 5865 keV. Both were interpreted as dominated by the $\nu 2g_{9/2}3p^{-1}_{1/2}$

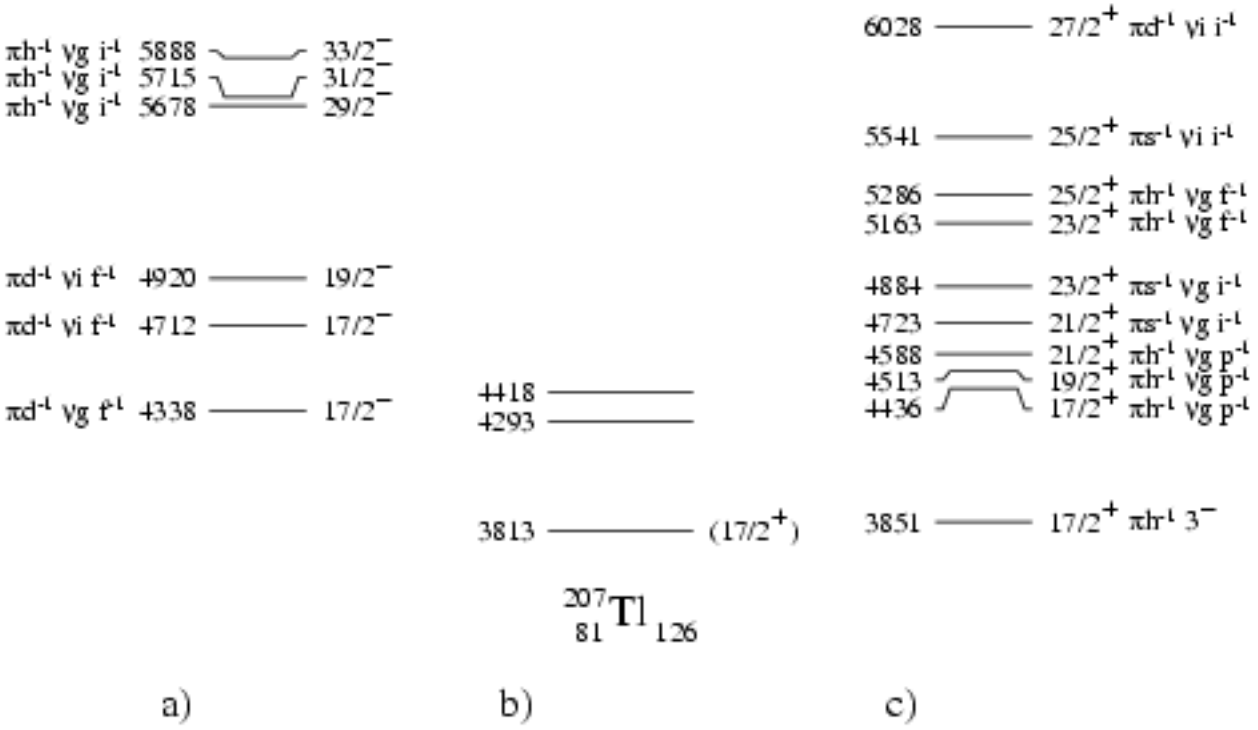


Figure 4.3 Comparison of the experimental b) level scheme of $^{207}$Tl with the results of shell-model calculations. Column a) shows the negative and c) the positive parity states. The leading configuration of the state is also given. The following shorthand is used for the configurations: protons ($\pi$) $h \equiv 1h_{9/2}$, $s^{-1} \equiv 3s^{-1}_{1/2}$, $d^{-1} \equiv 2d^{-1}_{3/2}$, $h^{-1} \equiv 1h^{-1}_{11/2}$ and neutrons ($\nu$) $g \equiv 2g_{9/2}$, $i \equiv 1i_{11/2}$, $j \equiv 1j_{15/2}$, $p^{-1} \equiv 3p^{-1}_{1/2}$, $f^{-1} \equiv 2f^{-1}_{5/2}$, $i^{-1} \equiv 1i^{-1}_{13/2}$. All energies are given in keV.

core excited state on top of the $12^-$ ($^{206}$Tl) isomer. The calculated $16^+$ is at 5887 keV and the $17^+$ at 5947 keV which is in reasonable agreement with the experimental data. The wave functions of these states are only moderately mixed and the main configuration $\nu 2g_{9/2}3p^{-1}_{1/2} \times 12^-(^{206}\mathrm{Tl})$ contributes 70% to the $16^+$ level and 59% to $17^+$.

The next yrast states at 6318 keV and 6706 keV have been interpreted as $(18^+)$ and $(19^+)$ of the $\nu 2g_{9/2}2f^{-1}_{5/2} \times 12^-(^{206}\mathrm{Tl})$ configuration. The corresponding calculated levels are at 6439 keV and 6627 keV and their structure is of a very high purity with the main component contributing more than 96% in each case. It is strange, that the $(19^+)$ level is calculated too low in contrast to all other states.

The highest state observed in the experiment has the excitation energy of 7118 keV. It has been described as $(20^-)$ of mainly the $\nu 2g_{9/2}1i^{-1}_{13/2} \times 12^-(^{206}\mathrm{Tl})$ configuration.

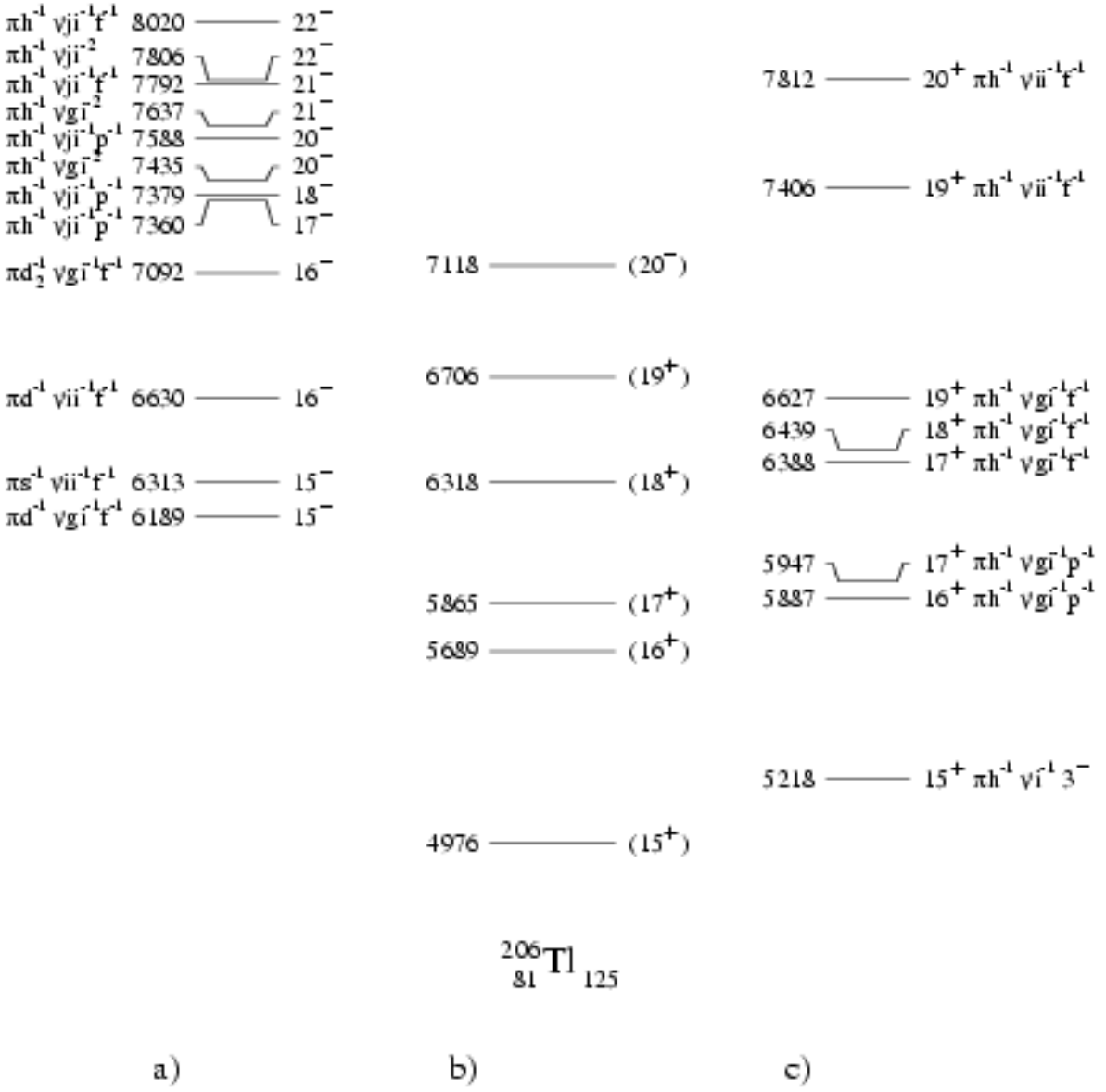


Figure 4.4 Comparison of the experimental b) level scheme of $^{205}$Tl with the results of shell-model calculations. Column a) shows the negative and c) the positive parity states. The leading configuration of the state is also given. The following shorthand is used for the configurations: protons ($\pi$) $s^{-1} \equiv 3s^{-1}_{1/2}$, $d^{-1} \equiv 2d^{-1}_{3/2}$, $d^{-1}_2 \equiv 2d^{-1}_{5/2}$, $h^{-1} \equiv 1h^{-1}_{11/2}$ and neutrons ($\nu$) $g \equiv 2g_{9/2}$, $i \equiv 1i_{11/2}$, $j \equiv 1j_{15/2}$, $p^{-1} \equiv 3p^{-1}_{1/2}$, $f^{-1} \equiv 2f^{-1}_{5/2}$, $i^{-1} \equiv 1i^{-1}_{13/2}$. All energies are given in keV.

The calculated $20^-$ state is at 7435 keV, which is 320 keV too high. The main component, the $\nu 2g_{9/2}1i^{-1}_{13/2} \times 12^-(^{206}\mathrm{Tl})$ configuration, contributes 52%. A sizeable admixture, 21% of $\pi 1h_{9/2}1h^{-1}_{11/2} \times 12^-(^{206}\mathrm{Tl})$, has been also predicted for this state.

The results of the shell-model calculation agree well with the experimental data as shown in the comparison above. The calculation accounts for all the experimentally observed levels. The calculated levels are generally too high in excitation energy. The difference between the calculated and the experimental level energy may reach up to about 300 keV. This is because the diagonal particle-hole matrix elements are wrong by about +130 keV on average, as the calculations for $^{208}$Pb have shown. It is clear that a slight adjustment of the particle-hole interaction could give results much closer to the experimental data.

# Chapter 5

# Summary and Conclusion

The subject of the present work was to study high spin states in nuclei near $^{208}$Pb by $\gamma$-ray spectroscopy methods. The experimental evidence on excited states at high spin in these nuclei was particularly scarce, because they are too neutron rich to be populated in fusion-evaporation reactions, the standard way to reach high spin states for $\gamma$-spectroscopy studies. Therefore, in our approach, deep inelastic collisions of heavy ion beams of $^{136}$Xe and $^{208}$Pb with $^{208}$Pb targets, were chosen to populate the nuclei in the $^{208}$Pb region. The $\gamma$-rays deexciting the high spin states in the nuclei of interest were measured using a multi-detector $\gamma$-spectrometer consisting of five HPGe-Cluster detectors and 132 NaI detectors of the EUROBALL and Crystal Ball arrays, respectively.

In the course of our studies experimental evidence on new high spin states in several nuclei lying close to $^{208}$Pb has been gained by the analysis of $\gamma$-ray decay patterns. The performed experiments gave neither angular distributions of the $\gamma$-transitions nor any other direct information on level spins and transition multipolarities. There is however clear and ample evidence, from previous experiments, that deep inelastic reactions populate almost exclusively yrast states. Combining this knowledge with information from other experiments and clear theoretical predictions allowed often to assign spins and parities to new levels.

The main achievements of the present study can be summarized as follows:

- The experiments revealed five new $\gamma$-transitions in $^{210}$Pb. They establish four new levels, above the previously known $8^+$ isomeric state, extending the level scheme of $^{210}$Pb up to 4.1 MeV of excitation energy. The new levels result from coupling of two neutrons in the $2g_{9/2}$, $1i_{11/2}$ and $1j_{15/2}$ shell-model orbitals and the highest state, $(\nu 1j^2_{15/2}, 14^+)$, has the maximum spin allowed for pure two

neutron excitations. The measured spectrum of the two-particle nucleus $^{210}$Pb yields directly the neutron-neutron two body residual interaction.

- New $\gamma$-transitions were identified from the spectrum of $^{209}$Pb extending its level scheme up to 6.1 MeV of excitation energy. The new levels are interpreted as formed by the coupling of the valence neutron in the $2g_{9/2}$, $1i_{11/2}$ and $1j_{15/2}$ shell-model orbitals to the low lying particle-hole excitations of the $^{208}$Pb core. Empirical shell-model calculations have been performed for 2p - 1h states in $^{209}$Pb and spins, parities and configurations assigned for states up to 4.3 MeV of excitation energy. The results of these calculations are in excellent agreement with the experimental evidence.

- An interesting phenomenon that has been studied in nuclei near $^{208}$Pb since a long time is the particle octupole-vibration coupling. Now the levels due to coupling of the collective octupole vibration with the $\pi 2d_{5/2}^{-1}$ and $\pi 1h_{11/2}^{-1}$ particles in $^{207}$Tl and the $\nu 2g_{9/2}$ and $\nu 1j_{15/2}$ particles in $^{209}$Pb have been found and the systematics of such states completed for all one particle(hole) neighbours of $^{208}$Pb. The particle octupole-vibration coupling in these states is strong; the coupling matrix element is large. The investigated levels lie close to the yrast line in a region of low level density so that mixing with other configurations can be neglected. Therefore they are very well suited to explore the particle octupole-vibration coupling. The measured data have been consistently described by this simple model and a very good agreement between theory and experiment has been obtained. It has been also shown that the effects due to the octupole admixture of two particle states can be calculated from those of one particle states demonstrating that the model is applicable for a wide range of nuclei.

- Shell-model calculations have been performed for $^{208}$Pb and neighbouring nuclei using for the first time the complete Kuo-Herling configuration space of particles and holes. Two body matrix elements of the realistic residual interaction, derived from the measured interaction between free nucleons, have been used. Of those the residual particle-particle and hole-hole interaction was taken from earlier approaches [Kuo68, Kuo71, McG75, Ryd90, War91]. The residual interaction between particles and holes has been newly determined using the H7B potential [Hos85, Bro]. The particle-hole states in $^{208}$Pb have then been calculated for the first time with the realistic interaction, and the resulting excitation energies and wave functions of the levels were compared in detail to those derived from experiments [Sch97, Rej95]. The excitation

energies are reproduced very well in $^{208}$Pb. The model also predicts the main features of wave functions of the levels. The extreme mixing and collectivity of the first $3^-$ state is reproduced by the model too. A very good agreement between the theory and the experiment proves the applicability of the H7B interaction.

The experimental progress in measuring states at high angular momentum in neutron rich nuclei near $^{208}$Pb is very promising for further extensive study of this mass region. The main topics to be studied are: (i) the development of the shell-model structures at large excitation energy and high angular momentum, (ii) the development of nuclear collectivity, particularly coupling to the vibrational states of octupole character, (iii) the applicability of the shell model theory to nuclei with increasing neutron excess, (iv) the collection of information on the neutron excess, that is required to soften the stability of nuclei in this mass region against deformation. Future work shall primarily exploit deep inelastic reactions of heavy and neutron rich ions, to populate the high spin states in nuclei with even larger neutron excess than identified at present. This will be possible by utilizing ion beams like $^{208}$Pb and even more neutron rich $^{238}$U of improved duty cycle combined with more powerful $\gamma$ spectrometers. Actually, the required facilities are available at the Argonne National Laboratories. The ATLAS linear accelerator provides intense heavy ion beams up to $^{238}$U and the GAMMASPHERE $\gamma$ spectrometer, built of 110 HPGe detectors in a symmetric assembly, provides a high detection efficiency (10%). The repetition of our experiments with those facilities would result in a statistical increase of the $\gamma$-$\gamma$ coincidence data by more than a factor of 100 for two-fold coincidences and would also give sufficient triple and higher fold $\gamma$ coincidences for analysis. In these experiments also the angular distribution of the $\gamma$-rays should be measured and evaluated. This has not been done so far mainly because of too little statistics. Hopefully some procedure can be found to determine spins and multipolarities as the evaluation of DCO ratios for fusion-evaporation reactions.

The general goal of nuclear physics is to calculate the properties of nuclei from the interaction between free nucleons. The agreement between the shell model calculation with a realistic interaction and the experimental data is promising. Therefore it is well worth the effort to continue with the measurement of nuclear properties around $^{208}$Pb and to perform new calculations of the residual interaction that can be done now with much less computational constraints.

# Chapter 6

# Appendix

## 6.1 Empirical two-body matrix elements of residual interaction

Table 6.1 The two-body matrix elements of residual interaction used in the ESM calculations of states in $^{209}$Pb (see also Section 3.2). The energies are given in MeV.

| Nucleus | $i$ | $j$ | $I^\pi$ | $\langle i\ j\|V\|i\ j\rangle$ | Ref. |
|---|---|---|---|---|---|
| $^{210}$Pb | $\nu 2g_{9/2}$ | $\nu 2g_{9/2}$ | $8^+$ | +0.031 | [Rej98] |
| $^{210}$Pb | $\nu 2g_{9/2}$ | $\nu 1i_{11/2}$ | $9^+$ | +0.050 | [Kuo71] |
| $^{210}$Pb | $\nu 2g_{9/2}$ | $\nu 1i_{11/2}$ | $10^+$ | −0.220 | [Rej98] |
| $^{210}$Pb | $\nu 2g_{9/2}$ | $\nu 1j_{15/2}$ | $11^-$ | −0.159 | [Rej98] |
| $^{210}$Pb | $\nu 2g_{9/2}$ | $\nu 1j_{15/2}$ | $12^-$ | $\Delta > 0$ | [Rej98] |
| $^{210}$Bi | $\pi 1h_{9/2}$ | $\nu 2g_{9/2}$ | $7^-$ | −0.233 | [Mar91] |
| $^{210}$Bi | $\pi 1h_{9/2}$ | $\nu 2g_{9/2}$ | $8^-$ | −0.084 | [Mar91] |
| $^{210}$Bi | $\pi 1h_{9/2}$ | $\nu 2g_{9/2}$ | $9^-$ | −0.395 | [Mar91] |
| $^{210}$Bi | $\pi 1h_{9/2}$ | $\nu 1i_{11/2}$ | $10^-$ | −0.778 | [Mar91] |
| $^{210}$Bi | $\pi 1h_{9/2}$ | $\nu 1j_{15/2}$ | $11^+$ | +0.010 | [Mar91] |
| $^{210}$Bi | $\pi 1h_{9/2}$ | $\nu 1j_{15/2}$ | $12^+$ | −0.621 | [Mar91] |
| $^{208}$Tl | $\nu 2g_{9/2}$ | $\pi 3s^{-1}_{1/2}$ | $4^+$ | +0.180 | [Mar86] |
| $^{208}$Tl | $\nu 2g_{9/2}$ | $\pi 3s^{-1}_{1/2}$ | $5^+$ | +0.140 | [Mar86] |
| $^{208}$Tl | $\nu 1i_{11/2}$ | $\pi 3s^{-1}_{1/2}$ | $6^+$ | +0.181 | [Kim64] |
| $^{208}$Tl | $\nu 1i_{11/2}$ | $\pi 2d^{-1}_{3/2}$ | $7^+$ | +0.155 | [Kim64] |
| $^{208}$Tl | $\nu 1j_{15/2}$ | $\pi 1s^{-1}_{1/2}$ | $7^-$ | +0.159 | [Kim64] |
| $^{208}$Tl | $\nu 1j_{15/2}$ | $\pi 1s^{-1}_{1/2}$ | $8^-$ | +0.084 | [Kim64] |

Table 6.2 The two-body matrix elements of residual interaction used in the ESM calculations of states in $^{209}$Pb (see also Section 3.2). The energies are given in MeV.

| Nucleus | $i$ | $j$ | $I^\pi$ | $\langle i\,j\|V\|i\,j\rangle$ | Ref. |
|---|---|---|---|---|---|
| $^{208}$Pb | $\nu 2g_{9/2}$ | $\nu 3p^{-1}_{1/2}$ | $4^-$ | $+0.095$ | [Rej95] |
| $^{208}$Pb | $\nu 2g_{9/2}$ | $\nu 3p^{-1}_{1/2}$ | $5^-$ | $-0.182$ | [Rej95] |
| $^{208}$Pb | $\nu 2g_{9/2}$ | $\nu 2f^{-1}_{5/2}$ | $5^-$ | $-0.150$ | [Rej95] |
| $^{208}$Pb | $\nu 2g_{9/2}$ | $\nu 2f^{-1}_{5/2}$ | $6^-$ | $-0.076$ | [Rej95] |
| $^{208}$Pb | $\nu 2g_{9/2}$ | $\nu 2f^{-1}_{5/2}$ | $7^-$ | $+0.052$ | [Rej95] |
| $^{208}$Pb | $\nu 1i_{11/2}$ | $\nu 3p^{-1}_{1/2}$ | $5^-$ | $-0.043$ | [Rej95] |
| $^{208}$Pb | $\nu 1i_{11/2}$ | $\nu 3p^{-1}_{1/2}$ | $6^-$ | $+0.007$ | [Rej95] |
| $^{208}$Pb | $\nu 1j_{15/2}$ | $\nu 3p^{-1}_{1/2}$ | $7^+$ | $+0.014$ | [Rej95] |
| $^{208}$Pb | $\nu 1j_{15/2}$ | $\nu 3p^{-1}_{1/2}$ | $8^+$ | $-0.146$ | [Rej95] |
| $^{208}$Pb | $\pi 1h_{9/2}$ | $\nu 3s^{-1}_{1/2}$ | $4^-$ | $-0.224$ | [Rej95] |
| $^{208}$Pb | $\pi 1h_{9/2}$ | $\nu 3s^{-1}_{1/2}$ | $5^-$ | $-0.353$ | [Rej95] |
| $^{208}$Pb | $\pi 1h_{9/2}$ | $\nu 2d^{-1}_{3/2}$ | $5^-$ | $-0.429$ | [Rej95] |
| $^{208}$Pb | $\pi 1h_{9/2}$ | $\nu 2d^{-1}_{3/2}$ | $6^-$ | $-0.181$ | [Rej95] |

## 6.2 Shell-model states in $^{208}$Pb

Table 6.3 The energies of excited states in $^{208}$Pb as calculated in present work. The calculations allowed the excitations of one particle from the doubly closed $^{208}$Pb (see also Section 4.1 and 4.2). The energies of levels are given for the lowest six states of each spin-parity multiplet. All energies are given in MeV.

| Spin | Nr. | E [MeV] | Spin | Nr. | E [MeV] | Spin | Nr. | E [MeV] | Spin | Nr. | E [MeV] |
|---|---|---|---|---|---|---|---|---|---|---|---|
| $0^+$ | 1 | 0.000 | $3^-$ | 5 | 5.016 | $7^-$ | 4 | 5.732 | $8^-$ | 4 | 6.576 |
| $3^-$ | 1 | 2.460 | $7^-$ | 3 | 5.035 | $8^+$ | 5 | 5.772 | $9^-$ | 2 | 6.585 |
| $5^-$ | 1 | 3.267 | $8^+$ | 2 | 5.051 | $7^+$ | 5 | 5.772 | $11^-$ | 1 | 6.591 |
| $4^-$ | 1 | 3.558 | $1^-$ | 2 | 5.073 | $1^-$ | 4 | 5.774 | $0^-$ | 3 | 6.598 |
| $5^-$ | 2 | 3.875 | $5^+$ | 1 | 5.090 | $7^+$ | 6 | 5.801 | $4^+$ | 5 | 6.602 |
| $1^-$ | 1 | 4.033 | $3^+$ | 1 | 5.095 | $6^+$ | 5 | 5.853 | $13^-$ | 1 | 6.605 |
| $5^-$ | 3 | 4.037 | $7^+$ | 2 | 5.095 | $1^+$ | 1 | 5.854 | $2^+$ | 3 | 6.616 |
| $6^-$ | 1 | 4.047 | $9^+$ | 1 | 5.116 | $7^-$ | 5 | 5.860 | $14^-$ | 1 | 6.745 |
| $7^-$ | 1 | 4.074 | $2^-$ | 2 | 5.125 | $9^+$ | 4 | 5.861 | $4^+$ | 6 | 6.785 |
| $4^-$ | 2 | 4.126 | $6^-$ | 6 | 5.157 | $11^+$ | 2 | 5.867 | $2^+$ | 4 | 6.803 |
| $3^-$ | 2 | 4.188 | $3^-$ | 6 | 5.166 | $12^+$ | 1 | 5.874 | $8^-$ | 5 | 6.857 |
| $4^-$ | 3 | 4.194 | $10^+$ | 2 | 5.178 | $2^-$ | 6 | 5.886 | $9^-$ | 3 | 6.926 |
| $5^-$ | 4 | 4.238 | $11^+$ | 1 | 5.257 | $9^+$ | 5 | 5.984 | $0^-$ | 4 | 6.974 |
| $6^-$ | 2 | 4.298 | $8^+$ | 3 | 5.266 | $8^+$ | 6 | 5.990 | $8^-$ | 6 | 7.016 |
| $5^-$ | 5 | 4.302 | $6^+$ | 2 | 5.352 | $8^-$ | 2 | 6.001 | $10^-$ | 2 | 7.038 |
| $4^-$ | 4 | 4.361 | $9^+$ | 2 | 5.361 | $4^+$ | 3 | 6.009 | $11^-$ | 2 | 7.090 |
| $4^-$ | 5 | 4.402 | $7^+$ | 3 | 5.408 | $6^+$ | 6 | 6.050 | $9^-$ | 4 | 7.094 |
| $2^-$ | 1 | 4.403 | $2^-$ | 3 | 5.420 | $10^+$ | 4 | 6.062 | $10^+$ | 5 | 7.229 |
| $3^-$ | 3 | 4.424 | $9^+$ | 3 | 5.446 | $2^+$ | 2 | 6.093 | $12^-$ | 2 | 7.240 |
| $5^-$ | 6 | 4.430 | $5^+$ | 2 | 5.466 | $1^-$ | 5 | 6.095 | $11^+$ | 3 | 7.403 |
| $6^-$ | 3 | 4.493 | $0^-$ | 1 | 5.488 | $5^+$ | 4 | 6.107 | $0^-$ | 5 | 7.492 |
| $6^-$ | 4 | 4.571 | $7^+$ | 4 | 5.511 | $1^-$ | 6 | 6.107 | $10^+$ | 6 | 7.632 |
| $3^-$ | 4 | 4.597 | $6^+$ | 3 | 5.535 | $5^+$ | 5 | 6.219 | $1^+$ | 2 | 7.650 |
| $2^+$ | 1 | 4.662 | $8^+$ | 4 | 5.538 | $3^+$ | 3 | 6.228 | $9^-$ | 5 | 7.752 |
| $7^-$ | 2 | 4.763 | $1^-$ | 3 | 5.552 | $4^+$ | 4 | 6.307 | $10^-$ | 3 | 7.843 |
| $8^+$ | 1 | 4.771 | $2^-$ | 4 | 5.603 | $5^+$ | 6 | 6.348 | $0^-$ | 6 | 7.908 |
| $6^-$ | 5 | 4.824 | $3^+$ | 2 | 5.609 | $3^+$ | 4 | 6.359 | $3^+$ | 5 | 7.920 |
| $4^-$ | 6 | 4.825 | $10^+$ | 3 | 5.617 | $8^-$ | 3 | 6.438 | $11^+$ | 4 | 8.310 |
| $7^+$ | 1 | 4.908 | $0^-$ | 2 | 5.627 | $9^+$ | 6 | 6.455 | $12^+$ | 2 | 8.441 |
| $8^-$ | 1 | 4.929 | $4^+$ | 2 | 5.653 | $10^-$ | 1 | 6.489 | $3^+$ | 6 | 8.550 |
| $4^+$ | 1 | 4.945 | $2^-$ | 5 | 5.670 | $7^-$ | 6 | 6.508 | | | |
| $10^+$ | 1 | 4.946 | $6^+$ | 4 | 5.693 | $9^-$ | 1 | 6.523 | | | |
| $6^+$ | 1 | 5.010 | $5^+$ | 3 | 5.717 | $12^-$ | 1 | 6.537 | | | |

Table 6.4 The energies of excited states in $^{208}$Pb as calculated in present work. The calculations allowed the excitations of two particles from the doubly closed $^{208}$Pb (see also Section 4.1 and 4.2). The energies of levels are given for the lowest six states of each spin-parity multiplet with spin $I \geq 14$. All energies are given in MeV.

| Spin | Nr. | E [MeV] | Spin | Nr. | E [MeV] | Spin | Nr. | E [MeV] | Spin | Nr. | E [MeV] |
|---|---|---|---|---|---|---|---|---|---|---|---|
| $14^-$ | 2 | 8.060 | $15^+$ | 5 | 9.444 | $21^+$ | 2 | 10.401 | $22^-$ | 5 | 11.547 |
| $14^-$ | 3 | 8.173 | $17^-$ | 4 | 9.462 | $18^-$ | 6 | 10.406 | $23^-$ | 3 | 11.582 |
| $15^-$ | 1 | 8.189 | $15^+$ | 6 | 9.498 | $20^+$ | 5 | 10.478 | $22^-$ | 6 | 11.608 |
| $14^-$ | 4 | 8.326 | $18^+$ | 1 | 9.538 | $19^-$ | 2 | 10.559 | $23^-$ | 4 | 11.952 |
| $14^+$ | 1 | 8.439 | $16^+$ | 4 | 9.546 | $20^+$ | 6 | 10.570 | $22^+$ | 4 | 12.010 |
| $14^-$ | 5 | 8.449 | $17^-$ | 5 | 9.566 | $20^-$ | 1 | 10.575 | $23^+$ | 1 | 12.031 |
| $14^-$ | 6 | 8.455 | $17^+$ | 3 | 9.571 | $21^-$ | 1 | 10.624 | $24^+$ | 1 | 12.092 |
| $15^-$ | 2 | 8.505 | $16^+$ | 5 | 9.575 | $22^+$ | 1 | 10.710 | $22^+$ | 5 | 12.120 |
| $15^-$ | 3 | 8.527 | $17^+$ | 4 | 9.583 | $22^-$ | 1 | 10.749 | $23^-$ | 5 | 12.121 |
| $15^-$ | 4 | 8.688 | $19^+$ | 1 | 9.593 | $20^-$ | 2 | 10.829 | $25^+$ | 1 | 12.224 |
| $15^-$ | 5 | 8.717 | $16^+$ | 6 | 9.593 | $19^-$ | 3 | 10.835 | $23^-$ | 6 | 12.292 |
| $15^-$ | 6 | 8.798 | $18^+$ | 2 | 9.615 | $21^-$ | 2 | 10.837 | $24^-$ | 2 | 12.415 |
| $14^+$ | 2 | 8.834 | $20^+$ | 1 | 9.706 | $22^-$ | 2 | 10.869 | $26^+$ | 1 | 12.445 |
| $16^-$ | 1 | 8.854 | $17^+$ | 5 | 9.710 | $19^-$ | 4 | 10.913 | $24^-$ | 3 | 12.553 |
| $17^-$ | 1 | 8.937 | $17^+$ | 6 | 9.718 | $19^-$ | 5 | 10.935 | $25^-$ | 1 | 12.632 |
| $16^-$ | 2 | 8.960 | $17^-$ | 6 | 9.724 | $21^+$ | 3 | 10.956 | $24^-$ | 4 | 12.683 |
| $15^+$ | 1 | 9.062 | $18^-$ | 1 | 9.771 | $23^-$ | 1 | 10.966 | $22^+$ | 6 | 12.746 |
| $16^-$ | 3 | 9.079 | $18^+$ | 3 | 9.798 | $19^-$ | 6 | 11.020 | $23^+$ | 2 | 12.831 |
| $14^+$ | 3 | 9.094 | $18^+$ | 4 | 9.852 | $21^+$ | 4 | 11.022 | $24^+$ | 2 | 12.940 |
| $16^+$ | 1 | 9.115 | $18^+$ | 5 | 9.869 | $23^-$ | 2 | 11.033 | $24^-$ | 5 | 12.963 |
| $16^-$ | 4 | 9.123 | $18^-$ | 2 | 9.882 | $20^-$ | 3 | 11.082 | $23^+$ | 3 | 12.979 |
| $14^+$ | 4 | 9.146 | $19^+$ | 2 | 9.903 | $21^+$ | 5 | 11.141 | $23^+$ | 4 | 12.983 |
| $16^-$ | 5 | 9.160 | $18^+$ | 6 | 9.907 | $20^-$ | 4 | 11.159 | $23^+$ | 5 | 12.987 |
| $17^-$ | 2 | 9.180 | $19^-$ | 1 | 9.949 | $21^-$ | 3 | 11.225 | $24^+$ | 3 | 13.018 |
| $14^+$ | 5 | 9.182 | $20^+$ | 2 | 10.009 | $22^+$ | 2 | 11.239 | $25^+$ | 2 | 13.072 |
| $16^-$ | 6 | 9.184 | $19^+$ | 3 | 10.022 | $21^+$ | 6 | 11.248 | $24^+$ | 4 | 13.094 |
| $14^+$ | 6 | 9.208 | $21^+$ | 1 | 10.037 | $20^-$ | 5 | 11.294 | $23^+$ | 6 | 13.150 |
| $15^+$ | 2 | 9.246 | $19^+$ | 4 | 10.052 | $21^-$ | 4 | 11.319 | $25^+$ | 3 | 13.222 |
| $17^+$ | 1 | 9.267 | $18^-$ | 3 | 10.074 | $20^-$ | 6 | 11.333 | $24^+$ | 5 | 13.361 |
| $16^+$ | 2 | 9.334 | $19^+$ | 5 | 10.123 | $22^+$ | 3 | 11.342 | $24^+$ | 6 | 13.658 |
| $15^+$ | 3 | 9.371 | $19^+$ | 6 | 10.148 | $22^-$ | 3 | 11.343 | $25^+$ | 4 | 13.862 |
| $17^-$ | 3 | 9.385 | $20^+$ | 3 | 10.151 | $21^-$ | 5 | 11.372 | $26^+$ | 2 | 13.966 |
| $15^+$ | 4 | 9.390 | $18^-$ | 4 | 10.158 | $24^-$ | 1 | 11.387 | $24^-$ | 6 | 14.703 |
| $16^+$ | 3 | 9.393 | $18^-$ | 5 | 10.191 | $21^-$ | 6 | 11.433 | $25^-$ | 2 | 15.170 |
| $17^+$ | 2 | 9.436 | $20^+$ | 4 | 10.252 | $22^-$ | 4 | 11.517 | | | |

# Bibliography


[Bar70] P.D. Barnes, E.R. Flynn, G.J. Igo, D.D. Armstrong, Phys. Rev. C1, 228 (1970)

[Bee78] J.R. Beene, O. Häusser, T.K. Alexander, A.B. McDonald, Phys. Rev. C17, 1359 (1978)

[Ber76] I. Bergstrom, J. Blomqvist, C.J. Herrlander, C.G. Linden, Z.Phys. A278, 257 (1976)

[Blo93] J. Blomqvist, R. Liotta, L.O. Norlin, U. Rosengard, B. Fant, T. Weckström, H.C. Jain, T. Lönroth, Nucl. Phys. A554, 45, (1993)

[Blo] J. Blomqvist, Private Communication

[Bro] B.A. Brown, Private Communication

[Bro84] B.A. Brown, A. Etchegoyen, W.D.M. Rae, N.S. Godwin, OXBASH, 1984 (unpublished)

[Bro92] E. Browne, Nucl. Data Sheets 65, 209 (1992)

[Bro94] R. Broda, C. T. Zhang, P. Kleinheinz, R. Menegazzo, K. H. Maier, H. Grawe, M. Schramm, R. Schubart, M. Lach, S. Hofmann , Phys. Rev. C49, R575 (1994)

[Bro96] R. Broda J. Wrzesiński, T. Pawlat, B. Fornal, Z. Grabowski, D. Bazzacco, S. Lunardi, C. Rossi-Alvarez, G. de Angelis, A. Gadea, K. H. Maier, Proceedings of the Conference on Nuclear Structure at the Limits, Argonne, Illinois, July 1996, ANL/PHY-97/1 p. 276

[Bru77] P.J. Brussaard, P.W.M. Glaudemans, Shell-model applications in nuclear spectroscopy, North-Holland Publishing Company, 1977

[Bohn81] H. Bohn, E. Endres, T. Faestermann, P. Kienle, Z. Phys A302, 51 (1981)

[Bohr69] A. Bohr, B.R. Mottelson, Nuclear Structure vol. 1, W.A. Benjamin, INC., 1969

[Bohr75] A. Bohr, B.R. Mottelson, Nuclear Structure vol. 2, W.A. Benjamin, INC., 1975

[Byr86] A.P. Byrne, G.D. Dracoulis, C. Fahlander, H. Hubel, A.R. Poletti, A.E. Stuchbery, J. Gerl, R.F. Davie, S.J. Poletti, Nucl. Phys. A448, 137 (1986)

[Byr94] A.P. Byrne, G.J. Lane, G.D. Dracoulis, B. Fabricius, T. Kibedi, A.E. Stuchbery, A.M. Baxter, K.J. Schiffer, Nucl. Phys. A567, 445 (1994)

[Byr98] A.P. Byrne, S. Bayer, G.D. Dracoulis, T. Kibedi, Phys. Rev. Lett. 80, 2077 (1998)

[Cle74] T.P. Cleary, N. Stein, P.R. Maurenzig, Nucl. Phys. A232, 287 and 311 (1974)

[Dec83] D.J. Decman, J. A. Becker, J. B. Carlson, R. G. Lanier, L. G. Mann, G. L. Struble, K. H. Maier, W. Stöffl, R. K. Sheline, Phys. Rev. C28, 1060 (1983)

[Don75] D.J. Donahue, O. Häusser, R.L. Hershberger, R. Lutter, F. Riess, Phys. Rev. C12, 1547 (1975)

[Dün75] W. Dünnweber, E.R. Cosman, E. Grosse, W.R. Hering, P. von Brentano, Nucl. Phys. A247, 251 (1975)

[Ebe94] J. Eberth, Proc. Conf. on Physics from Large $\gamma$- Detector Arrays, August 2-6, 1994, Berkeley, Ca., USA, vol. II, LBL-356

[Ecc65] D. Eccleshall, M.J.L Yates, Phys. Lett. 19, 301 (1965)

[Ell67] C. Ellegaard, J. Kantele and P. Vedelsby, Phys. Lett. 25B, 512 (1967)

[Ers65] J.R. Erskine, Phys. Rev. 138, B851 (1965)

[Fly71] E.R. Flynn, G. Igo, P.D. Barnes, D. Kovar, D. Bes, R. Broglia, Phys. Rev. C3, 2371 (1971)

[Fly72] E.R. Flynn, G. J. Igo, R. A. Broglia, S. Landowne, V. Paar, B. Nilsson, Nucl. Phys. A195, 97 (1972)

[Fly77] E.R. Flynn, R.A. Hardekopf, J.D. Sherman, J.W. Sunier, J.P. Coffin, Nucl. Phys. A279, 394 (1977)

[Gra92] P. Grabmayr, A. Mondry, G.J. Wagner, P. Woldt, G.P.A. Berg, J. Lisantti, D.W. Miller, H. Nann, P.P. Singh, E.J. Stephenson, J. Phys G18, 1753 (1992)

[Ham62] T. Hamada, I.D. Jonston, Nucl. Phys. 34, 382 (1962)

[Ham69] I. Hamamoto, Nucl. Phys. A126, 545 (1969)

[Ham70] I. Hamamoto, Nucl. Phys. A141, 1 (1970)

[Ham74] I. Hamamoto, Phys. Reports 10, 63 (1974)

[Han69] O. Hansen, O. Nathan, R. Chapman, S. Hinds, Nucl. Phys. A127, 71 (1969)

[Han77] O. Hansen, N. Stein, D.G. Burke, E.R. Flynn, J.D. Sherman, J.W. Sunier, R.K. Sheline, Nucl. Phys. A277, 451 (1977)

[Har81] B. Harmatz, Nucl. Data Sheets 34, 735 (1981)

[Häu76] O. Häusser, J.R. Beene, T.K. Alexander, A.B. McDonald, T. Faestermann, Phys. Lett. 64B, 273 (1976)

[Hey90] K.L.G. Heyde, The Nuclear Shell Model, Springer-Verlag, 1990

[Hos85] A. Hosaka, K.I. Kubo, H. Toki, Nucl. Phys. A444, 76 (1985)

[Igo69] G.J. Igo, P.D. Barnes, E.R. Flynn, and D.D. Armstrong, Phys. Rev. 177, 1831 (1969)

[Igo71] G. Igo, E.R. Flynn, B.J. Dropesky, P.D. Barnes, Phys. Rev. C3, 349 (1971)

[Jon81] B. Jonson, O.B. Nielsen, L. Westgaard, J. Żylicz, Proc. Int. Conf. Nuclei Far from Stability, Helsingør, Denmark, vol. 2, p. 640 (1981); CERN-81-09 (1981)

[Kim64] Y.E. Kim, J.O. Rasmussen, Phys. Rev. B135, B44 (1964)

[Kle79] P. Kleinheinz, R. Broda, P.J. Daly, S. Lunardi, M. Ogawa, J. Blomqvist, Z. Phys A290, 279 (1979)

[Kou89] M.C. Kouassi, A. Hachem, C. Ardisson, G. Ardisson, Nucl. Instrum. Methods A280, 424 (1989)

[Kov74] D.G. Kovar, N. Stein, C.K. Bockelman, Nucl. Phys. A231, 266 (1974)

[Kró96] W. Królas, PhD Thesis, Inst. of Nucl. Phys. Kraków Report No 1738/PL (1996)

[Kuo66] T.T.S. Kuo, G.E. Brown, Nucl. Phys. 85, 40 (1966)

[Kuo68] T.T.S. Kuo, Nucl. Phys. A122, 325 (1968)

[Kuo71] T.T.S. Kuo, G.H. Herling, US Naval Research Laboratory Report No. 2258, 1971 (unpublished)

[Law80] R.D. Lawson, Theory of the nuclear shell model, Clarendon Press Oxford, 1980

[Lac90] M. Lacombe, B. Loiseau, J.M. Richard, R. Vinh Mau, J. Côté, P. Pirès, R. de Tourreil, Phys. Rev. C21, 861 (1980)

[Lew70] M.B. Lewis, W.W. Daehnick, Phys. Rev. C1, 1577 (1970)

[Mai83] K.H. Maier, T. Nail, R.K. Sheline, W. Stöffl, J.A. Becker, J.B. Carlson, R.G. Lanier, L.G. Mann, G.L.Struble, J.A. Cizewski, B.H. Erkkila, Phys. Rev. C27, 1431 (1983)

[Mai97] K.H. Maier, Acta Physica Polonica B28, 277 (1997)

[Man88] L. G. Mann, K. H. Maier, A. Aprahamian, J. A. Becker, D. J. Decman, E. A. Henry, R. A. Meyer, N. Roy, W. Stöffl, G. L. Struble, Phys. Rev. C38, 74 (1988)

[Mar86] M.J. Martin, Nucl. Data Sheets 47, 797 (1986)

[Mar91] M.J. Martin, Nucl. Data Sheets 63, 723 (1991)

[Mar93] M.J. Martin, Nucl. Data Sheets 70, 315 (1993)

[McG75] J.B. McGrory, T.T.S. Kuo, Nucl. Phys. A247, 283 (1975)

[Met83] V. Metag, D. Habs, K. Helmer, V. v. Helmdt, H. W. Heyng, B. Kolb, D. Pelte,D. Schwalm, et al., Lecture Notes in Physics 178, ISBN 3-540-12001-7 Springer-Verlag Berlin (1983)

[Moy70] R.A. Moyer, B.L. Cohen, R.C. Diehl, Phys. Rev C2, 1898 (1970)

[Neu93] P. von Neumann-Cosel, P. Schenk, U. Fister, T.K. Trelle, R. Jahn, Phys. Rev C47, 1027 (1993)

[Paw94] T. Pawłat, R. Broda, W. Królas, A. Maj, M. Ziębliński, H. Grawe, R. Schubart, K.H. Maier, J. Heese, H. Kluge, M. Schramm, Nucl. Phys. A574, 623 (1994)

[Pii90] M. Piiparinen, P. Kleinheinz, S. Lunardi, M. Ogawa, G. de Angelis, F. Soramel, W. Męczyński, J. Blomqvist, Z. Phys. A337, 387 (1990)

[Pol86] S.J. Polleti, G.D. Dracoulis, A.R. Poletti, A.P. Byrne, A.E. Stuchbery, J. Gerl, Nucl. Phys. A448, 189 (1986)

[Pop88] N.A.F.M. Poppelier, P. W. M. Glaudemans, Z. Phys. A329, 275 (1988)

[Rej95] M. Rejmund, Diploma thesis, Warsaw University, 1995, (unpublished)

[Rej97] M. Rejmund, K.H. Maier, R. Broda, M. Lach, J. Wrzesiński, J. Agramunt, J. Blomqvist, A. Gadea, J. Gerl, M. Górska, H. Grawe, M. Kaspar, I. Kozhoukharow, I. Peter, H. Schaffner, R. Schubart, Ch. Schlegel, G. Stengel, S. Wan, H.J. Wollersheim, Z. Phys. A359, 243 (1997)

[Rej98] M. Rejmund, K.H. Maier, R. Broda, B. Fornal, M. Lach, J. Wrzesiński, J. Blomqvist, A. Gadea, J. Gerl, M. Górska, H. Grawe, M. Kaspar, H. Schaffner, Ch. Schlegel, R. Schubart, H.J. Wollersheim, EPJ A1, 261 (1998)

[Rej(a)] M. Rejmund et al., to be published

[Ryd90] L. Rydström, J. Blomqvist, R.J. Liotta, C. Pomar, Nucl. Phys A512, 217 (1990)

[Schl] Ch. Schlegel et al. to be published

[Sch92] M. Schramm, H. Grawe, J. Heese, K.H. Maier, R. Schubart, R. Broda, J. Grębosz, W. Królas, A. Maj, J. Blomqvist, Z. Phys. A344, 121 (1992)

[Sch93] M. Schramm, PhD. thesis, Freie Universität Berlin, 1993; Hahn-Meitner-Institut Report B-508, 1993

[Sch93(a)] M. Schramm, H. Grawe, J. Heese, K.H. Maier, R. Schubart, R. Broda, J. Grębosz, W. Królas, A. Maj, J. Blomqvist, Z. Phys. A344, 363 (1993)

[Sch95] M. Schramm, M. Rejmund, K.H. Maier, H. Grawe, J. Blomqvist, Phys. Scr. T56, 307 (1995)

[Sch97] M. Schramm, K.H. Maier, M. Rejmund, L.D. Wood, N. Roy, A. Kuhnert, A. Aprahamian, J. Becker, M. Brinkman, D.J. Decman, E.A. Henry, R. Hoff, D. Manatt, L.G. Mann, R.A. Meyer, W. Stoeffl, G.L. Struble, T.F. Wang, Phys. Rev. C56, 1320 (1997)

[Sjo80] T.P. Sjoreen, U. Garg, D. B. Fossan, Phys. Rev. C21, 1838 (1980)

[Smi71] S.M. Smith, P.G. Roos, C. Moazed, A.M. Bernstein, Nucl. Phys A173, 32 (1971)

[Spe89] R.H. Spear, At. Data Nucl. Data Tables 42, 55, (1989)

[Str82] J. Streets, B.A. Brown, P.E. Hodgson, J. Phys G8, 839 (1982)

[Tul95] J.K. Tuli, NDS 74, 349 (1995)

[Ura78] I. Uray, I. Tõrõk, P. Bornemisza-Pauspertl, L. Vegh, Z.Phys A287, 51 (1978)

[Val97] B.D. Valnion, PhD. thesis, Ludwig-Maximillians-Universität Mũnchen, 1997, (unpublished)

[Wag75] W.T. Wagner, G.M. Crawley, G.R. Hammerstein, Phys. Rev. C11, 486 (1975)

[War91] E. K. Warburton, B. A. Brown, Phys. Rev. C43, 603 (1991)

[Wil80] W.W. Wilcke, J.R. Birkelund, H.J. Wollersheim, A.D. Hoover, J.R. Huizenga, W.U. Schrõder, L.E. Tubbs, At. Data Nucl. Data Tables 25, 389 (1980)

[Wrz] J. Wrzesiński, et al., to be published

[Yeh97] M. Yeh, PhD. thesis, University of Kentucky, 1997, (unpublished)

[Zwa85] D. Zwarts, Comp. Phys. Commun. 38, 365 (1985)

# Acknowledgments

The successful realization of this research work was possible thanks to the kind assistance of many colleagues, who supported and participated in this project. I would like to gratefully acknowledge all of them.

Especially, I am greatly indebted to Dr K.H Maier from HMI Berlin who triggered this scientific program and whose contribution to the experimental work and the interpretation of results was enormous and very essential. Many thanks for the long hours of enlightening discussions, encouragement, optimism and a great help at all phases of the work.

I am also very thankful to:

- The members of the Nuclear Structure group at IFJ Kraków led by Prof R. Broda, including Dr M. Lach, Dr J. Wrzesiński and Dr B. Fornal for help in realizing experiments and partnership in data analysis. Particularly, I am grateful to Prof R. Broda for fruitful discussions and comments to the subject of this work.

- Dr H. Grawe from GSI Darmstadt for many discussions also concerning the nuclear physics in general.

- The members of EUROBALL Nuclear Spectroscopy group at GSI Darmstadt led by Dr J. Gerl, including, Dr H.J. Wollersheim, Dr Ch. Schlegel, Dr I. Kozhoukharow, MSc M. Kaspar, MSc I. Peter and MSc H. Schaffner for help in running experiments, enjoyable atmosphere and kind support of my studies. Especially, I am grateful to Dr J. Gerl for making it possible for me to continue research studies in GSI Darmstadt and for enthusiastic support of my activities.

- Prof J. Blomqvist from RIT Stockholm for enlightening remarks and comments to the subject of my study.

- Prof B.A. Brown from MSU for providing me with the shell-model code OXBASH, for deriving the H7B two-body matrix elements of residual nucleon-nucleon interaction for $^{208}$Pb region and for essential help related to the shell-model calculations.

- Dr hab. T. Rząca-Urban for the kind support of my studies and activities and for many valuable comments to this thesis.

- M. Górska for the assistance in my research work and partnership in a private life.